1-1-1975

Design and Fabrication of a Double Ion Implanted Hyperabrupt Diode for Use as a Voltage Variable Capacitor.

Albert Francis Walcheski

Design and Fabrication of a Double Ion Implanted Hyperabrupt Diode for Use as a Voltage Variable Capacitor

by

ALBERT FRANCIS WALCHESKI

A Thesis

Presented to the Graduate Committee

of Lehigh University

in Candidacy for the Degree of

Master of Science

in

Electrical Engineering

Lehigh University

1975

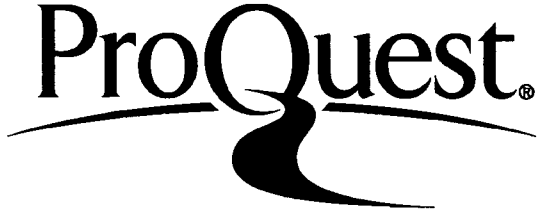

This thesis is accepted and approved in partial fulfillment of the requirements for the degree of Master of Science in Electrical Engineering.

May 7, 1925
(Date)

Professor in Charge

Chairman of Department

TABLE OF CONTENTS

LIST OF FIGURES

I. Abstract

This paper discusses the design and fabrication of a hyperabrupt varacter diode for the 39A Precision Oscillator used in the L5 telephone coaxial transmission system. Device requirements are that the capacitance is greater than 120 pF at 1 volt reverse bias and less than 10 pF at 10 volts reverse bias. Fabrication techniques of double diffused, alloy, epitaxial, ion-implantation and hybrid structures are discussed as possible ways of meeting the device requirements with the final design selected being a double implanted structure. The first implant and drive-in modifies the N doping profile and the second implant, done through an SiO_2 layer, forms the shallow PN junction. A model is developed which describes the enhancement profile as a Gaussian function and the second implanted profile as an exponential function and takes into account the reoxidation step prior to the second implant. A computational method is described for calculating the resultant C-V characteristics from the computed concentration profile. Good agreement is obtained between measured and calculated values and the model is used to show the variation in the C-V characteristics when the first implant dose, second implant dose, and oxide thickness are varied.

II. Introduction

Reversed biased PN junctions are widely used for their voltage-variable capacitance characteristics, but the capacitance range of the more familiar linear graded and abrupt step junctions is limited to the maximum value of its slope "m" $(-d\log C/d\log V)$[1] of 0.5 or less and the maximum reverse voltage that may be applied before the device goes into avalanche breakdown. For these reasons, there is considerable interest in hyperabrupt junction diodes which offer changes of capacitance of a factor of ten or better over a small voltage swing and have maximum slopes of approximately 2 to 5. Especially important uses for these devices would be in oscillator applications; either in FM circuits where the voltage swing across the diode translates directly into an FM signal or in precision oscillator applications where the varactor diode is used to tune or program the desired frequency and maintain that set frequency. It was the latter of these two applications that prompted the development of the varactor diode presented in this paper.

The application is the 5.12 MHz 39A Precision Oscillator[2] used as a reference frequency generator in the L5 Jumbo Group Frequency Supply. The L5 system can multiplex 108,000 two-way telephone conversations over a 22 line coaxial cable system with two cables used as spares. The basic oscillator is a modified Pierce oscillator with

varactor diodes in a crystal network to control the operating frequency. For this application, the varactor diode should have a capacitance value of less than 10 pF at a reverse voltage of 10 volts and greater than 120 pF at a reverse voltage of 1.0 volt. Since the varactor diodes will be located in the crystal oven which is maintained at ~85°C, and since the varactors are biased from a high impedance source, the reverse leakage should be low and equal to or less than 1.0 nanoampere at 2.0 volts reverse bias when measured at an ambient temperature of 25°C. This would translate to a worst case condition of approximately 150 nanoamperes at 85°C.

Some additional system constraints are that the device be encapsulated in a TO-18 package, that the diode element be electrically insulated from the can, and that a third lead be provided which is connected to the can for grounding.

III. Discussion of Available Fabrication Techniques

It is obvious from the previous discussion that in order to have a device with the required C-V characteristics, one must have a retrograded doping profile on the lighter doped side of the junction. This can be accomplished in various ways.

1. Double diffused[3] - Assuming a P^+N junction, one can first alter the N layer profile by performing an N diffusion (i.e., antimony) and then a subsequent P

diffusion (i.e., boron) to form the P^+ layer. One major problem, however, is that the C-V characteristics of the resultant devices vary widely resulting in a low yield to a fairly tight C-V requirement.

2. Alloy[4,5] - One can form the retrograded profile by using the well known alloy diffusion technique. The impurity (Sb) dissolved into some carrier metal (Sn or AgPb) acts as the source for the impurity enhancement. After alloying, the excess metal is removed from the surface and the contact metal (Al) is evaporated and alloyed to form the P^+ region. This technique is really double diffusion with alloy diffusions substituted for the gassious types. The resultant devices have tighter distributions than that of the double diffused in 1.

3. Epitaxial growth[6] - One can also alter the doping profile by use of low temperature epitaxial growth. In growing a high resistivity epi layer as the background concentration, one can then introduce more dopant at the end of the epi cycle to form the modified profile required. A subsequent diffusion forms the diode junction and completes the process. Device variability then depends on the control of the epi process.

4. Ion implantation[1] - With the advent of the practical use of ion-implantation as a diffusion source, a high degree of control is obtainable in tailoring the

doping profile. The epi structure is implanted and driven-in to form the retrograded profile. This technique coupled with a Schottky barrier junction provides a highly controlled process. Also, with the use of a guarded Schottky structure, one can achieve reverse leakages in the several nanoampere range.

5. MIS structure[7] - In this technique instead of forming a Schottky diode on an ion-implanted modified profile as in 4, one forms a metal-insulator-semiconductor structure. This alleviates the reverse leakage problem but this hybrid design is subject to the loss and stability problems associated with MIS structures.

After reviewing the techniques described above, the following design was decided upon. It will be of the basic double diffused structure of 1 but will incorporate ion-implantation as a diffusion source for the retrograded junctions as in 4. It will also have a guard ring as in 4 but the P^+ junction will be formed by another ion-implantation but, unlike the first implant, the dopant will be implanted through an SiO_2 layer. This second implant will only be annealed, not diffused, so as not to move the first implanted and diffused profile. Implanting through an SiO_2 layer allows one to shift the peak of the implanted profile to the surface. This double ion-implanted technique allows one to have a high degree of

control over the doping profile yet have low, stable reverse leakages similar to those of diffused silicon junction diodes.

IV. Theoretical Considerations

The main parameter of interest is, of course, the C-V relationship of the completed device. This C-V relationship can be expressed as:

$$C = k/V^m \qquad (1)$$

where

C = the capacitance
k = a constant
V = the reverse voltage
m = the power constant

For a step junction $m = \frac{1}{2}$ and for a linearly graded junction $m = \frac{1}{3}$. Hyperabrupt junctions can be defined as those devices having m values greater than $\frac{1}{2}$. In general, doping profiles of hyperabrupt junctions have steep transition regions where the doping profile changes from the enhanced higher concentration area to the lower background doping. Through this region, the net doping may change two orders of magnitude. Since the C-V characteristic is determined by the impurity doping profile, one must first obtain an accurate description of the PN doping profile. This requires the analysis of a double diffused structure since an enhancement diffusion

is first performed to produce the retrograde profile and a second diffusion to form the PN junction. If an alloy or Schottky structure is used for the P^+ layer, then only one side of the junction need be analyzed since the depletion region extends only into the lower doped side. If the junction is formed by ion-implantation or diffusion, then for small reverse voltages the depletion region in the heavier doped side must be taken into account. Figure 1 illustrates the type of structure to be discussed. First an enhancement diffusion is performed of the same conductivity type as the background doping N_B. This diffusion results in the profile N_D. Secondly, the PN junction is formed by an opposite type diffusion with the resultant profile N_A. Ideally, the second profile can be formed without disturbing the first profile.

For the diode presented in this paper, the enhancement diffusion is formed by an ion-implantation predeposition and subsequent drive-in. Assuming a fixed total impurity, the dopant will have a Gaussian concentration profile given as:

$$N_D(x) = \frac{Q_1}{(\pi Dt)^{1/2}} \exp\left(-x^2/(4Dt)\right) \qquad (2)$$

where

Q_1 = the implanted dose in ions/cm^2

D = the diffusion coefficient in cm^2/sec

t = the diffusion time in seconds.

Adding the background doping to Eq. (2) yields an expression for the donor impurity profile as:

$$N_D(x) = \frac{Q_1}{(\pi Dt)^{1/2}} \exp\left(\frac{-x^2}{4Dt}\right) + N_B \qquad (3)$$

The acceptor profile is accomplished by a second ion-implantation and anneal, not a drive-in, which keeps the first distribution intact. The general expression for an implanted profile is also Gaussian and is given by:

$$N_A(x) = \frac{Q_2}{\sqrt{2\pi}\ \Delta R_p} \exp\left(-\frac{(x-R_p)^2}{2\Delta R_p^2}\right) \qquad (4)$$

where

Q_2 = the implant dose in ions/cm^2

R_p = the projected ion range in cm

ΔR_p = the projected straggle distance in cm

This implant would result in a Gaussian profile totally within our structure, not like the N_A profile of Figure 1. However, if one implanted through an oxide layer whose thickness was just equal to R_p at the implant energy, one could end up with the N_A profile of Figure 1 whose distribution would be:

$$N_A(x) = \frac{Q_2}{\sqrt{2\pi}\ \Delta R_p} \exp\left(-\frac{x^2}{2\Delta R_p^2}\right) \qquad (5)$$

However, since the enhanced layer in this structure is relatively shallow (~1μm), an accurate description of

the acceptor profile is critical since variations in this profile will greatly affect the C-V characteristic. Others[8] have observed that the Gaussian profile is accurate in describing a boron implanted profile in silicon but this fit is mostly accurate from N_A max to ± 0.5 N_A max. Below this range, the Gaussian profile drops more rapidly than the measured profile. Since it is that very region which determines the junction in this structure, the exponential function best describes the N_A profile and is given by:

$$N_A(x) = \frac{Q_2}{\sqrt{2\pi}\ \Delta R_p} \exp \frac{-x}{\lambda} \qquad (6)$$

where λ is a constant for a given implant energy.

Figure 2 illustrates the difference in the net concentration profile when the N_A profile is assumed to be either Gaussian or exponential and all other parameters are kept constant.

One other area must be considered before the entire concentration profile can be determined and that is, the effect of the low temperature oxidation after the N_D profile is produced and before the second implant is performed. This oxidation, in effect, moves the start of the implanted N_A profile in from x=0 to x=0.44 X_{OX} where X_{OX} is the oxide thickness. This can be accounted for by modifying Eq. (3) as:

$$N_D(x) = \frac{Q_1}{(\pi Dt)^{1/2}} \exp\left(-\frac{(X+OX)^2}{4Dt}\right) + N_B \qquad (7)$$

where OX = 0.44 times the oxide thickness.

Eq. (6) and (7) now describe the total profile, and N(X) can now be written as:

$$N(x) = \frac{Q_2}{\sqrt{2\pi}\,\Delta R_p} \exp\frac{-x}{\lambda} - \frac{Q_1}{(\pi Dt)^{1/2}} \exp\left(-\frac{(X+OX)^2}{4Dt}\right) - N_B \qquad (8)$$

Also, to simplify the analysis, the following three assumptions are made.

1. The presence of mobile carriers in the depletion region is ignored.
2. Complete ionization of impurities in the depletion region is assumed.
3. The depletion layer is separated from the electrically neutral region by a sharp boundary.

Shockley[9] developed the theory for PN junctions and stated that the electric field distribution, E(x), across a reversed biased junction can be determined from the solution of Poisson's equation as:

$$E(x) = (q/K\varepsilon_o) \int_{x_1}^{x} N(x)\,dx \qquad (9)$$

where

q = the magnitude of electronic charge

K = the dielectric constant

ε_o = the permittivity of free space

$N(x)$ = the doping concentration from Eq. (8)

x_1 = the edge of one side of the depletion region

The voltage distribution, $V(x)$, is given as:

$$V(x) = \int_{x_1}^{x} E(x)\,dx \tag{10}$$

where $E(x)$ is given by Eq. (9).

Finally, the capacitance, C, per unit area is:

$$C(V) = K\varepsilon_o/(x-x_1) \tag{11}$$

The computation of the C-V relationship for this device proceeded in this manner.

1. For a given set of parameters, Eq. (8) is solved for x when $N_A = N_D+N_B$. This value of x is the junction depth x_j.
2. An x_1 is chosen such that $\Delta x = x_j-x_1$.
3. A value of x on the other side of x_j is calculated such that the total charge per unit area on either side of the PN junction is equal and opposite.
4. The field distribution, $E(x)$, is numerically calculated using Eq. (9).
5. The field distribution is numerically integrated, Eq. (10), producing a value $V(x)$.

6. The built-in voltage, V_B, is calculated using:[10]

$$V_B = \frac{KT}{q} \ln \frac{N_A N_D}{n_i^2} \qquad (12)$$

where

K = Boltzman's constant

T = Temperature in °K

q = Magnitude of electronic charge

N_A = Acceptor concentration just outside the space charge region

N_D = Donor concentration just outside the space charge region

n_i = Intrinsic carrier concentration

7. The applied voltage, V_R, is calculated such that $V_R = V(x) - V_B$.

8. Finally, the capacitance is calculated using Eq. (11) and multiplying the result by A, the area of the device.

Therefore, choosing values for x_1 in the N_A layer produces values of V_R and C, so incrementing through the N_A layer from $x_1 = x_j$ to $x_1 \to 0$ produces the desired C-V relationship.

A computer program was written in Fortran to perform the series of computations described. This program was run on a Honeywell 6078 computer which produced the results that are discussed in Section VI.

V. Device Fabrication

Starting material is a silicon epitaxial wafer approximately .012 inches (305μm) thick and 1.5 inches in diameter. The substrate is .01 Ω-cm antimony doped and the epitaxial layer is 10-15μm thick and 19-24 Ω-cm arsenic doped. Crystal orientation is <111> with a <110> flat on the slice. First oxidation is for 3 hours at 1050°C steam to produce approximately 8000Å of SiO_2 on the slice. As a heavy metal gettering step, the oxide from the back of the slice is removed and the slice is given a 30 minute 1100°C phosphorus diffusion using a $POCl_3$ source. The phosphorus glass is then removed by etching. Another oxidation follows at a temperature of 1050°C for 2 hours in steam. The next operation is a photolithographic step to open up a ring in the oxide .032 inches in diameter and .0006 inches wide. Care is taken in this step to keep the oxide intact on the back of the slice. The slice then undergoes a boron diffusion using a BN source for 10 minutes at 1140°C and boron drive-in at 1200°C for 10 minutes. This diffused ring acts as a guard ring around the shallow P^+ region to prevent low breakdown due to the small radius of curvature (~.4μm) of the active junction. The junction depth of the guard ring diffusion is ~2.5μm. The next operation is another photolithographic step which opens up the area within the guard ring and

slightly overlaps the guard ring (see Figure 3). This area, .0326 inch diameter circle, is the window in which will be implanted the phosphorus for the epi enhancement. The implant dose, Q_1, is 3.5×10^{12} phosphorus ions/cm^2 at 50 Kev. A short 900°C 30 minute anneal in oxygen is followed by the phosphorus drive-in at 1100°C for 75 minutes in oxygen. The original .0326 inch diameter circle is reopened by a non-selective etch and ~1000Å of SiO_2 is regrown at 900°C in steam. It is through this oxide that the boron will be implanted. The boron implantation is at a dose, Q_2, of 5.0×10^{14} boron atoms/cm^2 at 35 Kev. A 900°C anneal in oxygen for 30 minutes completes the high temperature treatments. The slice is passivated with a layer of approximately 2000Å of Si_3N_4 and the contact is platinum silicide-titanium-titanium nitride-platinum-gold. To accomplish the electrical isolation required for this application, a .050x.070x.025 inch ceramic, metallized on both sides, is first brazed onto the TO-18 header and the diode chip is eutectic bonded on top of the ceramic platform. Gold wires are thermocompression bonded to the chip and to the platform making the electrical connection to the leads of the package.

VI. Device Tests and Computed Results

Figure 4 is a C-V plot of completed devices along with the computed values of C and V for the given parameter

values. The spread in the measured data shows the slice to slice variation. Agreement with theory is quite good indicating that the model is adequate for predicting results for a variation of parameters and that the profile of Figure 2 with the assumed exponential function accurately describes the concentration profile. In Figure 5, the results of varying the phosphorus implant dose is calculated showing the resultant C-V curves at three different phosphorus doses. Likewise, Figures 6 and 7 show the calculated C-V curves for three different implant doses into a given phosphorus profile and the effect of a variation of the oxide thickness on the resultant C-V profile. As can be seen, a great variety of devices can be made using this design by varying the area, implants, drive time, and oxide thickness.

Care should be taken, however, that the boron implant dose be made sufficiently large and the P^+ region sufficiently heavily doped so as not to sweep out the entire P^+ region when the device is reversed biased. If this occurs, there is an increase in reverse current as the edge of the depletion region reaches the surface. This was observed at 4.0 volts reverse bias with a boron implant of 8×10^{13} ions/cm^2 and at 6 volts reverse bias when the boron implant was 1×10^{14} ions/cm^2. At 5×10^{14} ions/cm^2 this increase in reverse current was not observed.

Figure 8 is a plot of the reverse leakage at 2.0 volts reverse bias versus temperature. The devices are less than 1 nanoampere at 25°C and meet the requirements of the system. Device breakdown is ~150 volts at 25°C and at breakdown the depletion region has swept entirely through the epitaxial layer into the substrate. A plot of forward voltage versus forward current is given in Figure 9 along with references to the empirical forward current-voltage characteristics where m=1 for pure diffusion and m=2 for pure recombination current.

VII. Aging Conditions and Results

Since the device will normally be used in the reverse direction as a variable capacitor, the aging condition is in the reversed biased state also. The failure mechanism would be caused by any mobile ions which migrate towards the junction, modifying the doping concentration at the edge of the planar junction, and causing an increase in reverse leakage due to the creation of a channel or the reduction of the breakdown voltage. This migration is accelerated by increasing the reverse voltage and increasing the temperature. The aging condition is, therefore, a 150°C reverse bias (V_R=10 Vdc) test for 100 hours. All devices shipped must meet this in-process test and upon completion must pass the less than 1 nanoampere requirement at 2 volts reverse bias. All devices are

previously screened to the 1 nanoampere limit prior to the in-process aging and results to date have indicated that 95% of the devices fabricated thus far have passed the in-process age criteria.

VIII. Summary

This paper has presented a design and fabrication technique for manufacturing a stable, highly controlled, voltage variable capacitance diode utilizing a double ion-implanted structure. It offers a fabrication technique compatible with existing silicon integrated circuit technology along with highly reproducible results and high yields. A model has also been developed which accurately describes the device and it can be used as a design guide for adopting this design to the manufacture of other similar hyperabrupt devices.

IX. References

1. G. F. Foxhall and R. A. Moline, "Ion-Implanted Hyperabrupt Junction Voltage Variable Capacitors," IEEE Trans. Electron Devices, Ed. 19 (1972), pp. 267-273.

2. A. F. Flint and H. S. Pustarfi, "39A Precision Oscillator," Bell System Technical Journal, Vol. 53, No. 10 (1974), pp. 2097-2107.

3. A. B. Bhattacharyya and T. N. Basavaraj, "Transitions-Capacitance Calculations for Double-Diffused p-n Junctions," Solid State Electronics, Vol. 16 (1973), pp. 467-476.

4. P. J. W. Jochems, O. W. Memelink, and L. J. Tummers, Proc. Inst. Radio Engrs. 46, (1958) p. 1161.

5. T. Sukegawa, A. Shimizu, and J. Nishizana, National Convention Record of the Joint Conference of the IEE, IECE, IEI and ITE, Japan, Pt. 13, (1962) p. 1050.

6. S. Nakanuma, "Silicon Variable Capacitance Diodes With High Voltage Sensitivity by Low Temperature Epitaxial Growth," NEC Research and Development, (1967), pp. 53-66, Indexed in Engineering Index 1966 p. 2684 from IEEE Trans. on Electron Devices, July 1966.

7. B. A. Maciver, "Characteristics of Ion-Implanted Hybrid Voltage-Variable Capacitors," Electronic Letters, Vol. 9 (1973), pp. 210-212.

8. L. O. Bauer, M. R. Macpherson, A. T. Robinson, and H. G. Dill, "Properties of Silicon Implanted With Boron Ions Through Thermal Silicon Dioxide," Solid-State Electronics, Vol. 16 (1973), pp. 289-300.

9. W. Shockley, "The Theory of p-n Junctions in Semiconductors," Bell System Technical Journal, Vol. 28 (1949), pp. 435-450.

10. A. S. Grove, Physics and Technology of Semiconductor Devices. New York: John Wiley and Sons, Inc., 1967.

HYPERABRUPT DOPING PROFILE

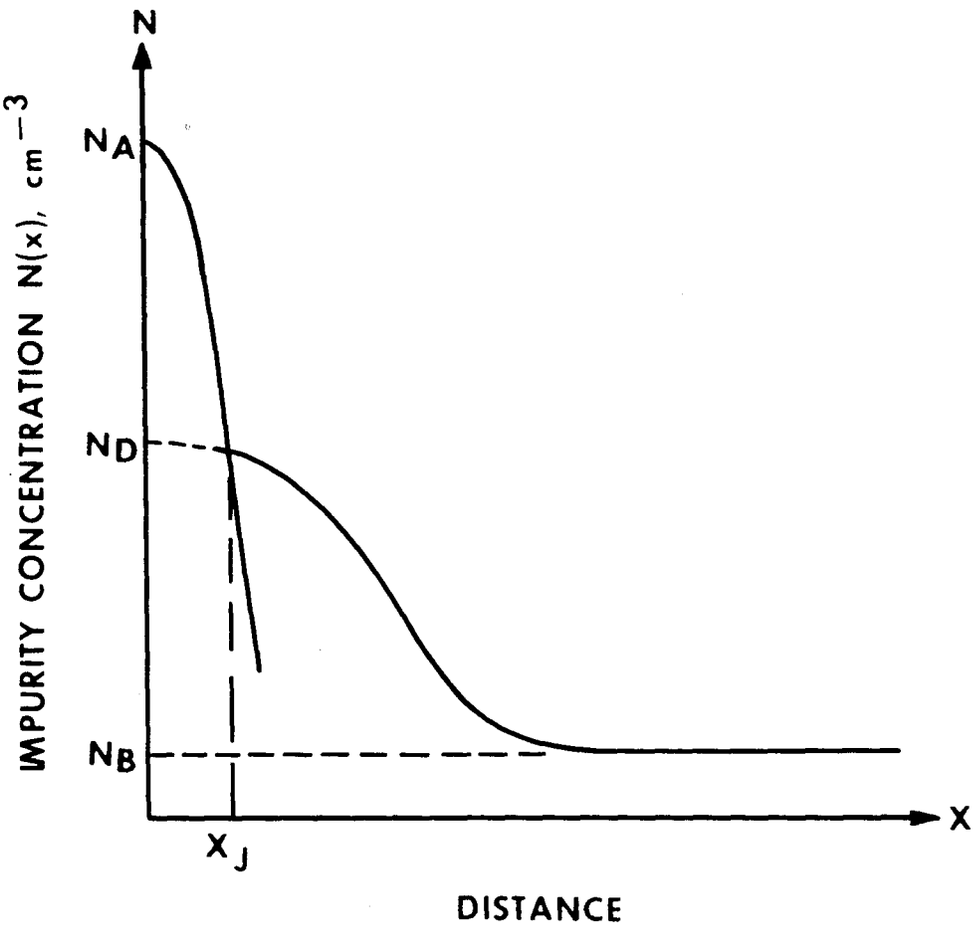

FIGURE 1

CALCULATED DOPING PROFILES

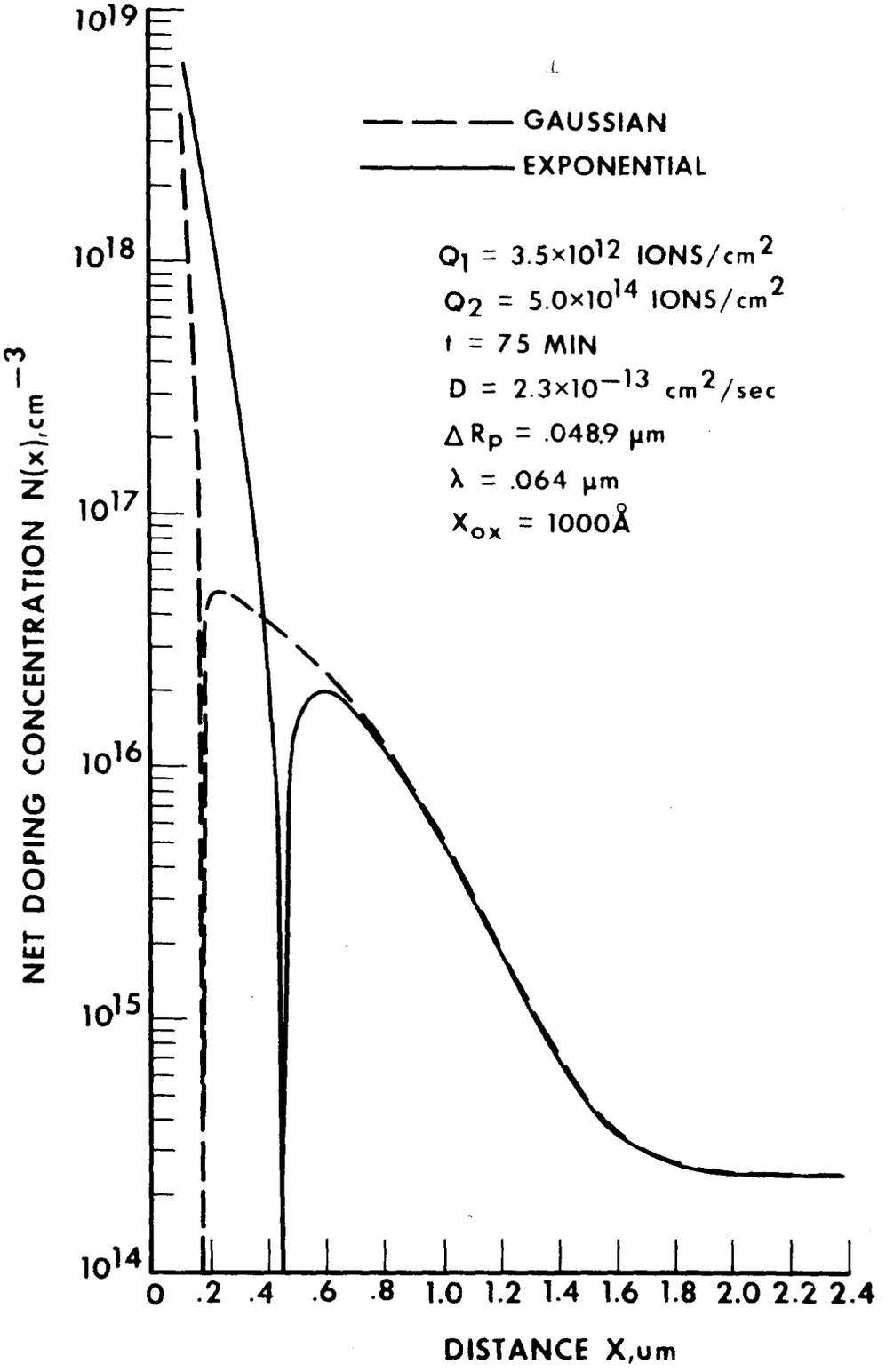

FIGURE 2

DIODE CHIP STRUCTURE

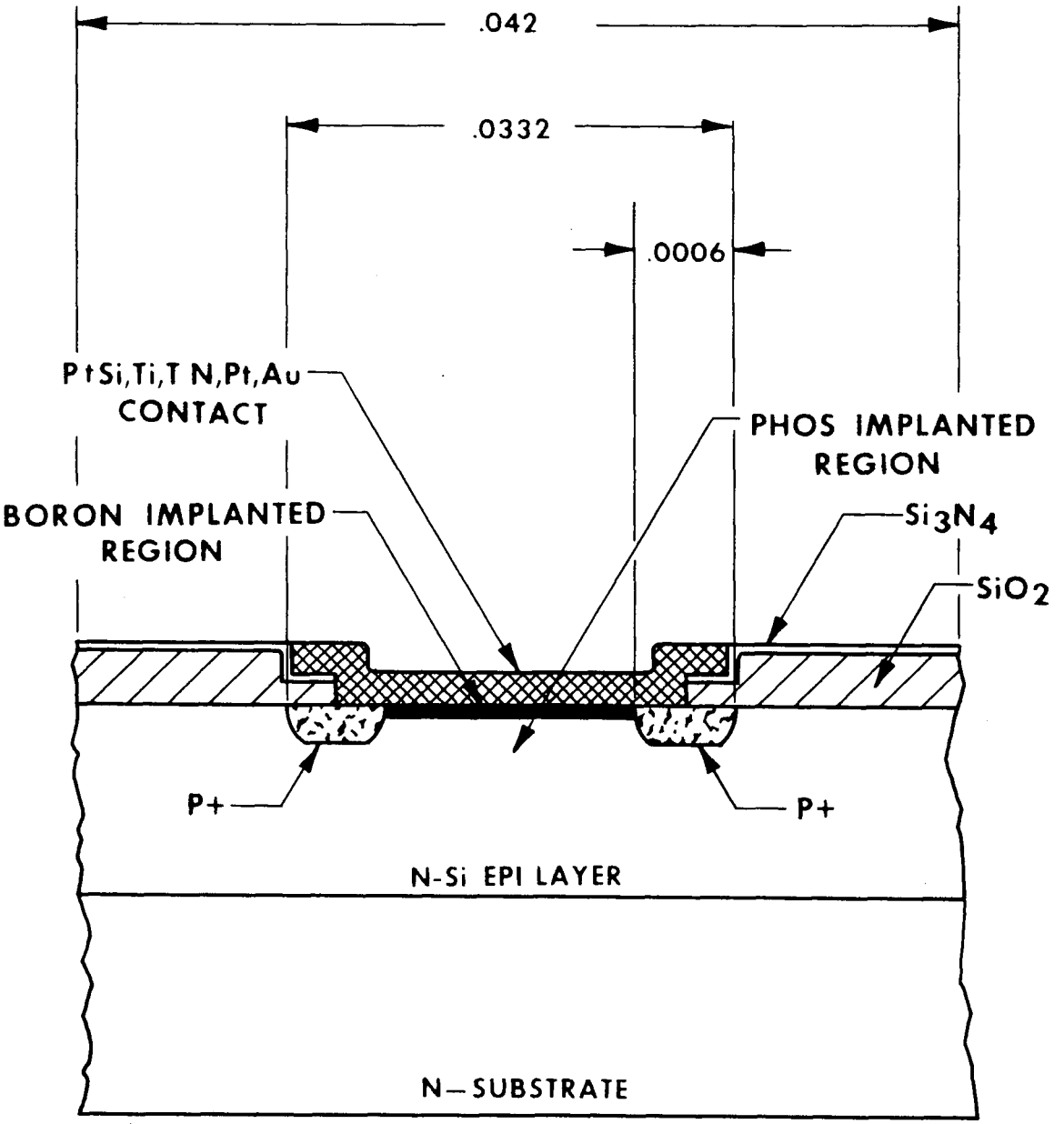

FIGURE 3

COMPUTED VS MEASURED C-V RESULTS

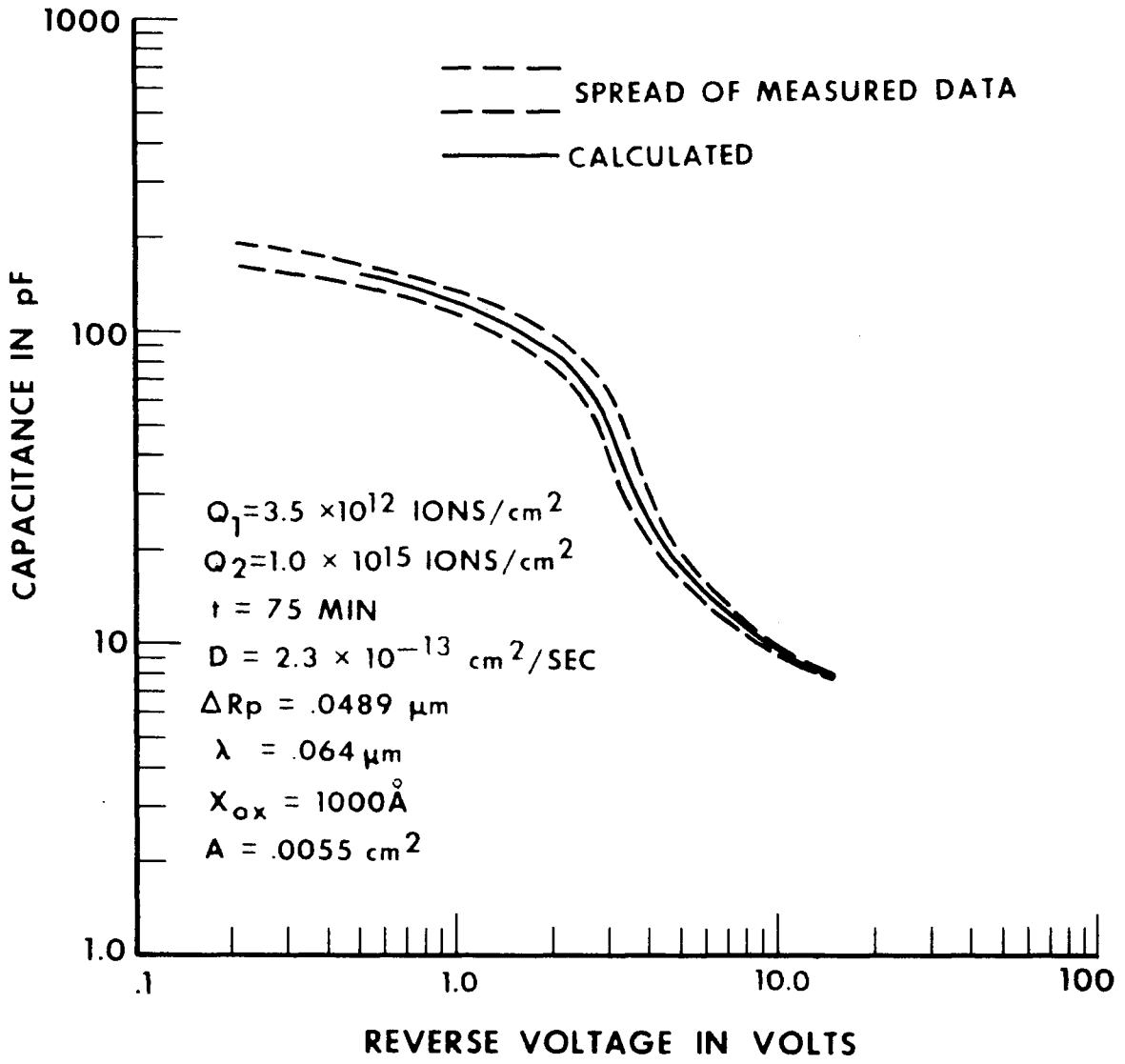

FIGURE 4

CALCULATED EFFECT OF VARIATION OF PHOSPHOROUS IMPLANT, Q_1

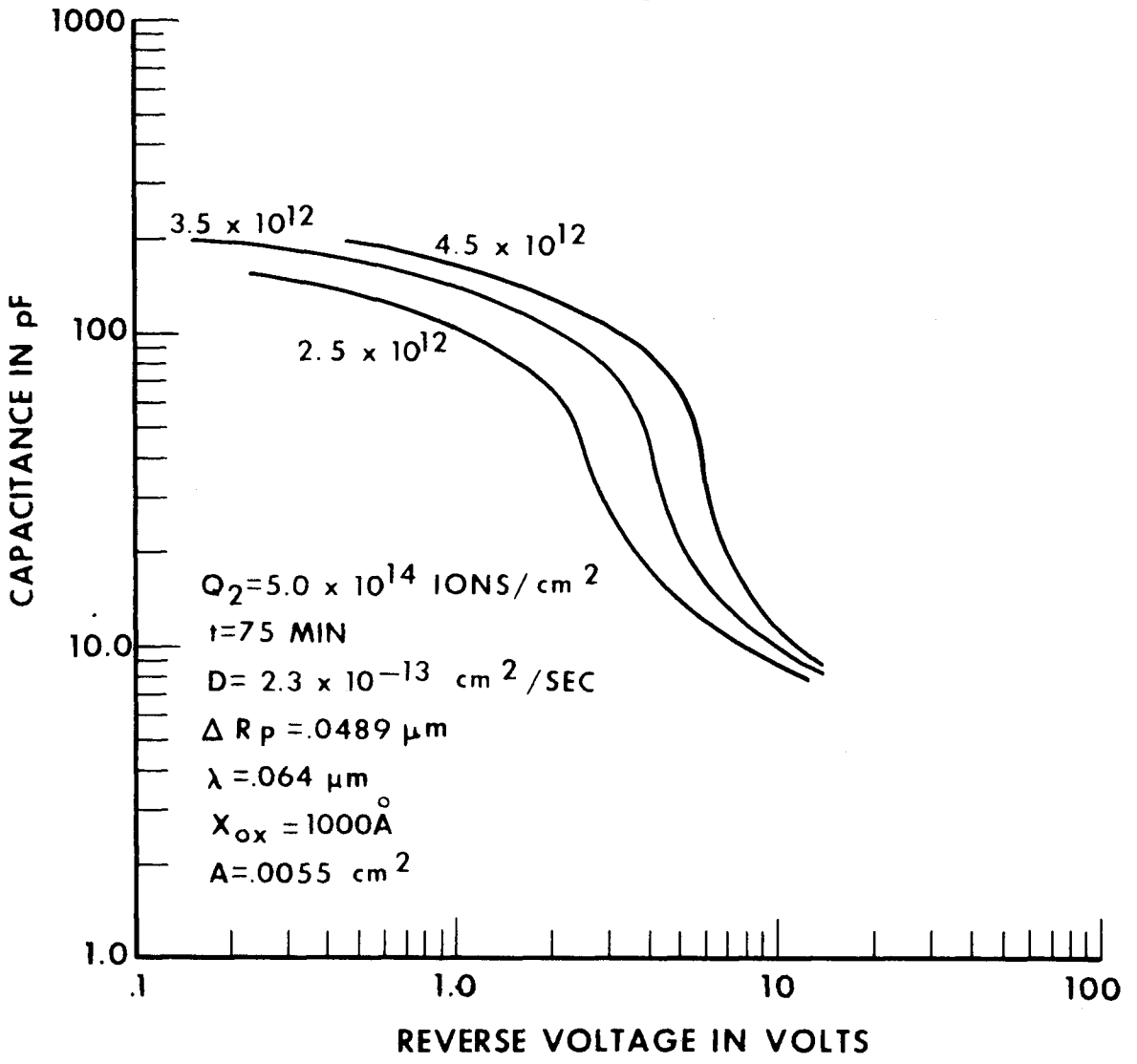

FIGURE 5

CALCULATED EFFECT OF VARIATION OF BORON IMPLANT, Q_2

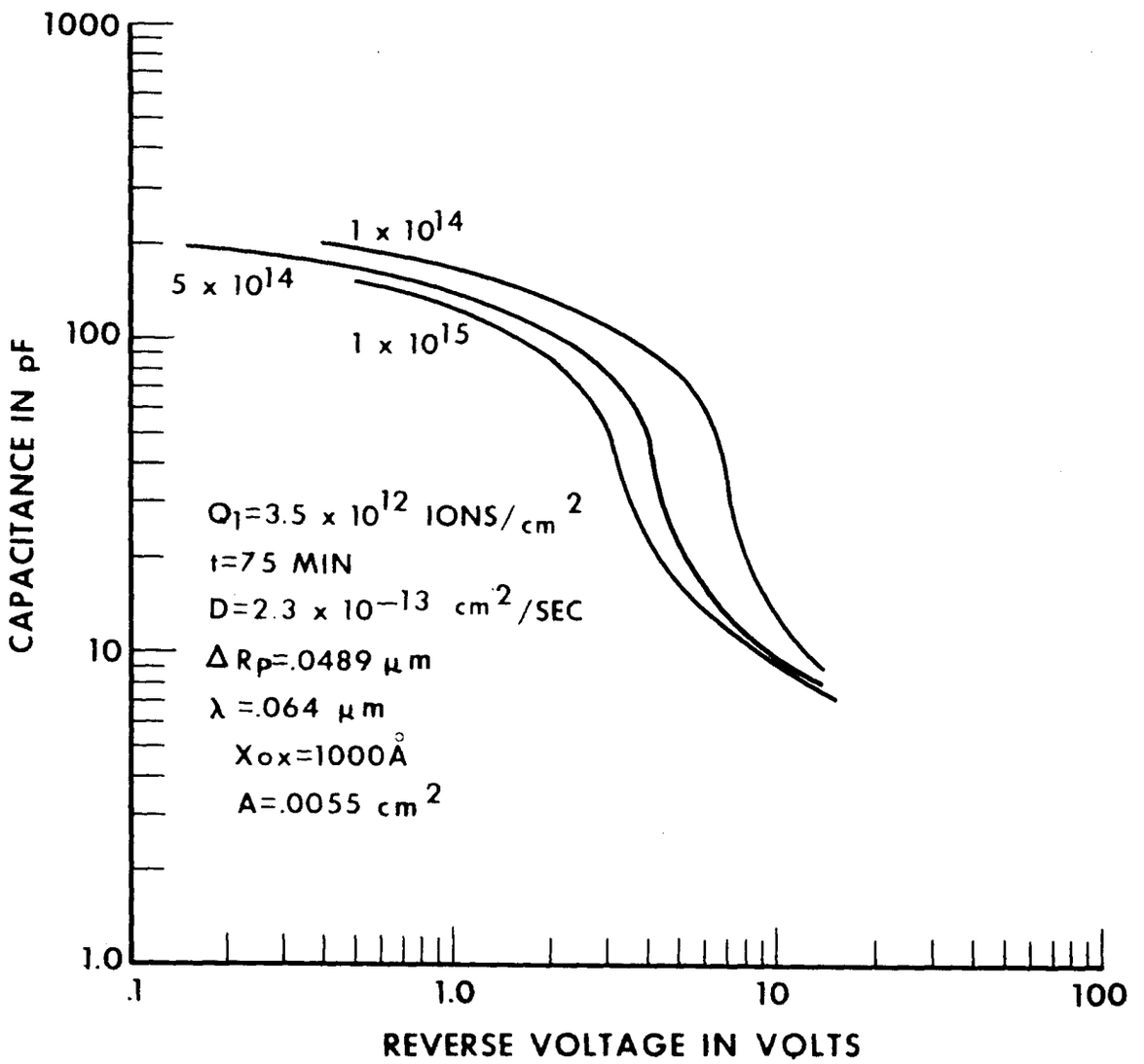

FIGURE 6

CALCULATED EFFECT OF VARIATION OF OXIDE THICKNESS, X_{ox}

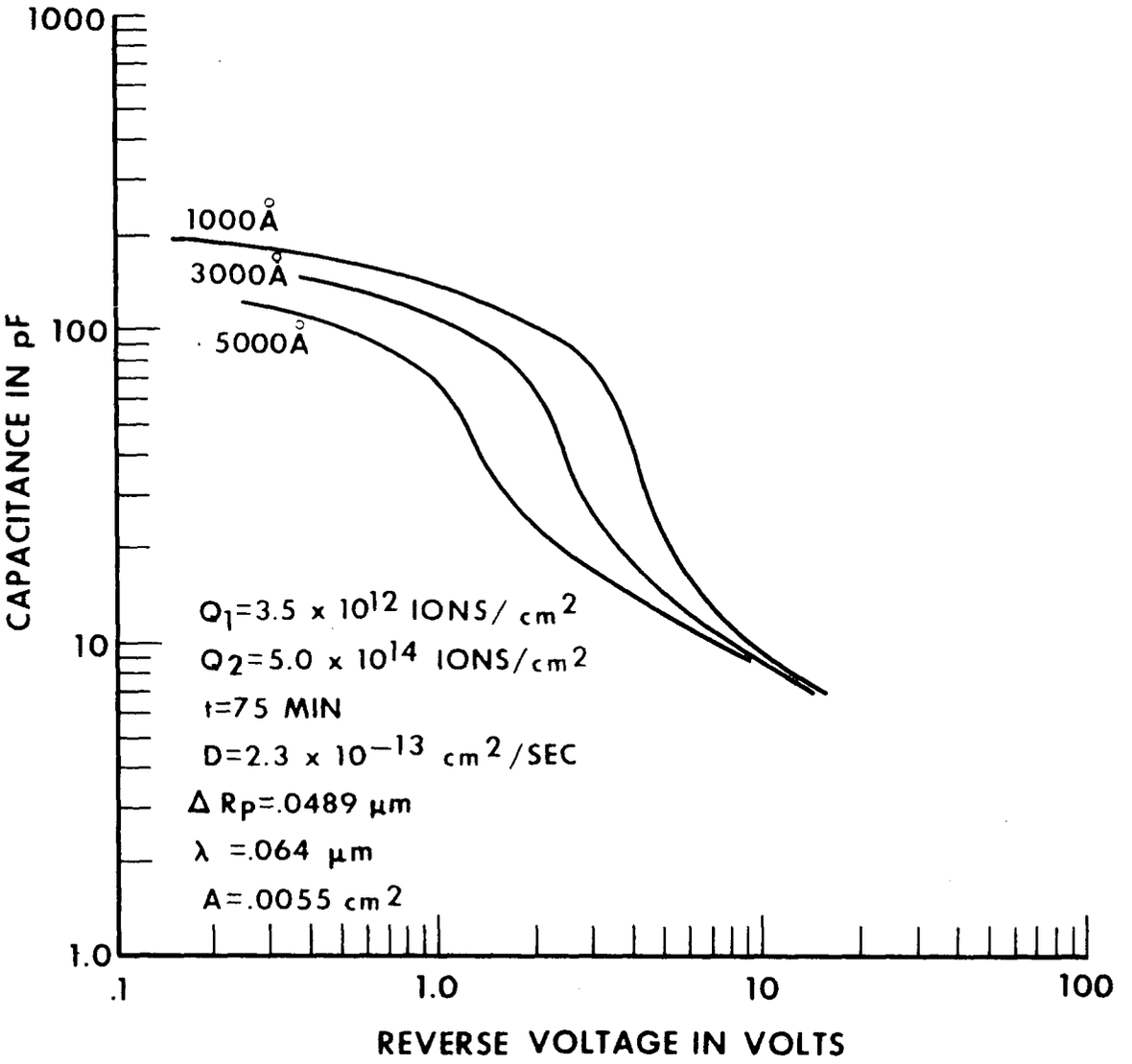

FIGURE 7

DIODE REVERSE LEAKAGE VS TEMPERATURE

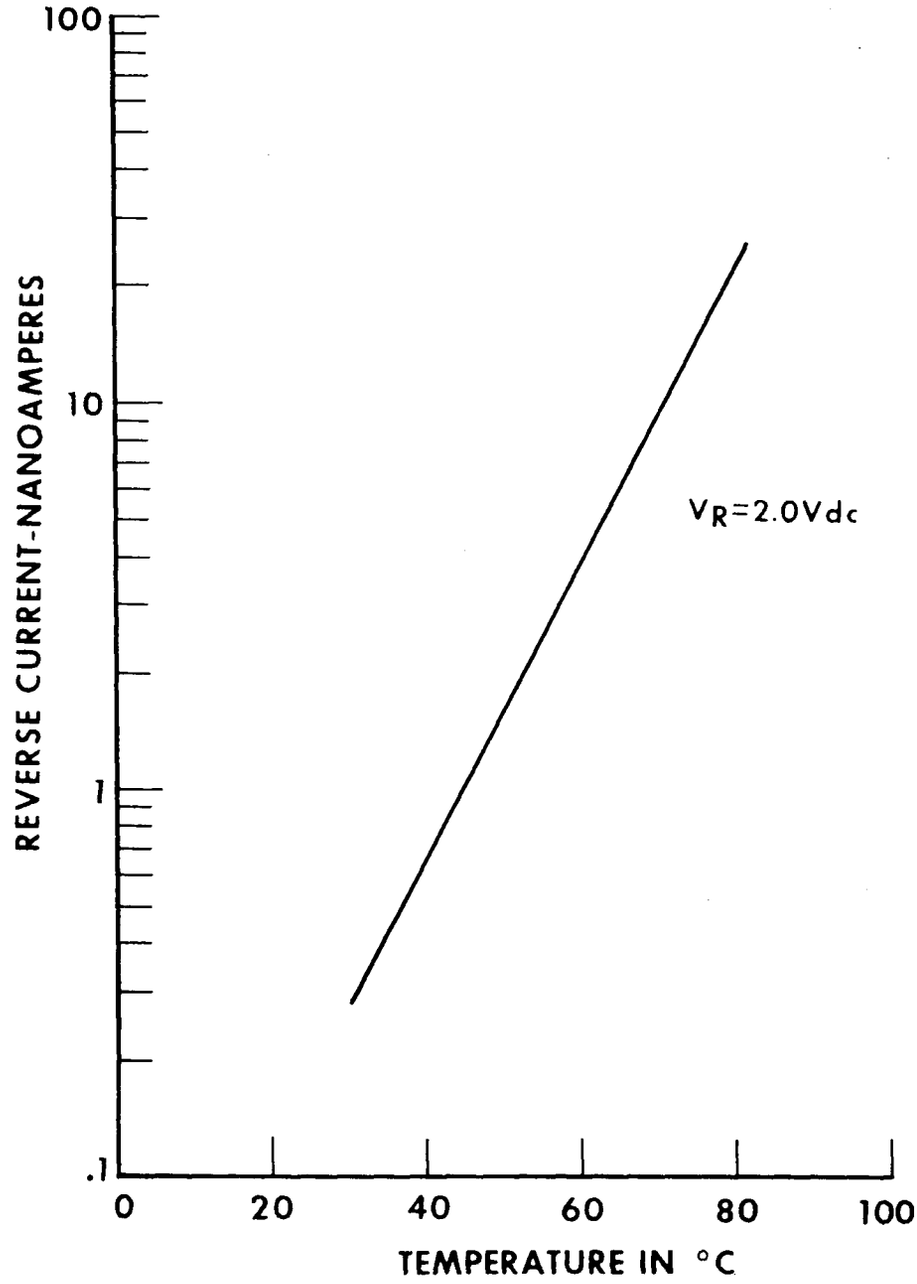

FIGURE 8

FORWARD VOLTAGE CHARACTERISTICS

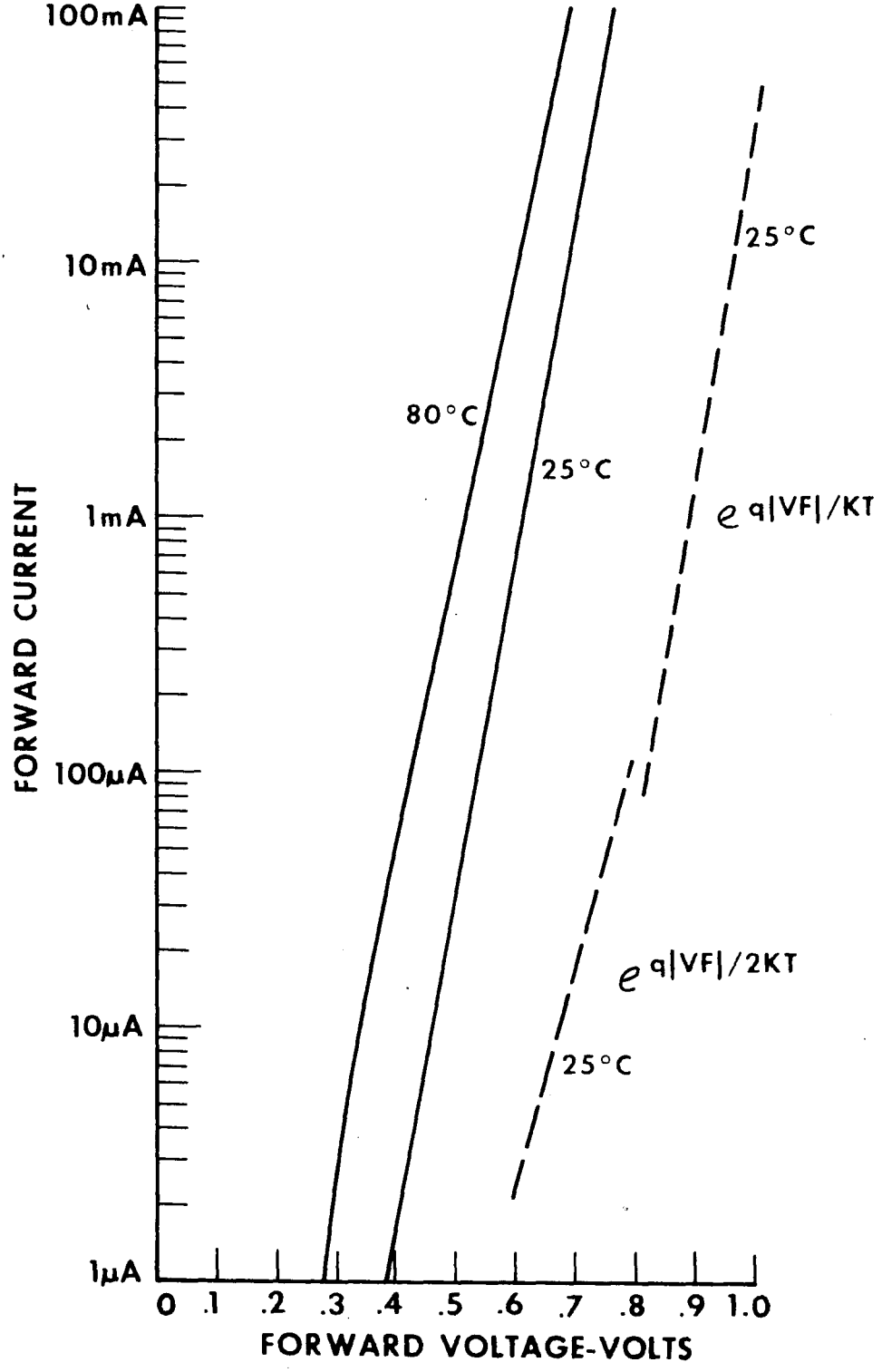

FIGURE 9

X. Vita

Mr. Albert F. Walcheski was born in Sugar Notch, Pennsylvania on August 10, 1937, the son of Joseph J. and Helen S. Walcheski. He graduated from Sugar Notch High School, Sugar Notch, Pennsylvania in June 1955. He received an Associate Degree of Electrical Technology from Pennsylvania State University-General Extension, Wilkes Barre center in June 1959, and a Bachelor of Science Degree in Physics from Albright College in June 1971. He has been employed with the Bell Telephone System since June 1959, first being employed by Western Electric Co., Laureldale, Pennsylvania and, since 1962, with Bell Telephone Laboratories, Reading, Pennsylvania. He currently has the position of Associate Member of Technical Staff in the Semiconductor Device Technology Group and device responsibility for hyperabrupt diodes and discrete junction field effect transistors. He and his wife, the former Geraldine M. Ford, reside in Reading, Pennsylvania.

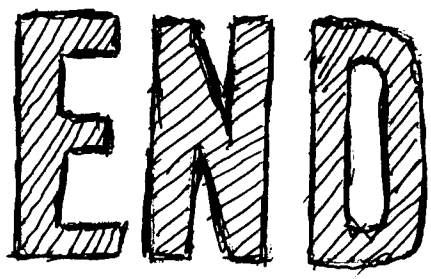
END

Flash

NO.

11


START

ANALYSIS OF LOAD DISTRIBUTION IN PRESTRESSED CONCRETE I-BEAM BRIDGES

by

Martin A. Zellin

A Thesis
Presented to the Graduate Committee
of Lehigh University
in Candidacy for the Degree of
Master of Science
in Civil Engineering

Lehigh University
Bethlehem, Pennsylvania

May, 1975

CERTIFICATE OF APPROVAL

This thesis is accepted and approved in partial fulfillment of the requirements of the degree of Master of Science.

Accepted May 8, 1975
(Date)

Professors in Charge

Dr. Celal N. Kostem

Dr. David A. VanHorn

Chairman of Department
Dr. David A. VanHorn

TABLE OF CONTENTS

LIST OF TABLES

LIST OF FIGURES

ABSTRACT

This thesis presents a refined method for the evaluation of live-load distribution factors for right, ie no skew, multi-beam bridges with prestressed concrete I-beams. The analytic technique used in the study is the finite element stiffness formulation for linearly elastic eccentrically stiffened plate structures. A brief description of the analysis technique and selected bridge models employed in a study correlating analytic results with those obtained from field test are presented. This study enabled an accurate investigation of live-load distribution by modeling the important design parameters.

The design and results of an analytic experiment to investigate live-load distribution is also presented. The results of the analytic experiment are used in arriving at a new method for evaluating live-load distribution.

1. INTRODUCTION

1.1 General

For many years, a large number of states, including the State of Pennsylvania, have been utilizing precast, prestressed concrete beams in the construction of multi-beam highway bridges. In these multi-beam bridges the beams are spread apart and equally spaced. Beams with either box-shaped or I-shaped cross-sections have been used and they are covered with a cast-in-place reinforced concrete deck. Since 1964, several research investigations on the structural behavior of these bridges have been conducted at Lehigh University. Each investigation covered one or more aspects of superstructure response to design vehicle loadings. This report will will present the results of a project initiated in 1972 which was centered on the development of proposed design provisions for live-load distribution in prestressed concrete I-beam bridges.

The Pennsylvania Department of Transportation (PennDOT) initially adopted some of the provisions of the American Association of State Highway and Transportation Officials (AASHTO) specifications[1] concerning the lateral distribution of live-load in multi-beam bridges. It should be noted here that in this report a multi-beam bridge is defined as constructed with the beams spread apart and equally spaced while AASHTO defines a multi-beam bridge as constructed with the beams placed side by side on the supports. The provisions of the AASHTO specifications that applied to spread

I-beam bridges were also applied to spread box-beam bridges. Using the provisions adopted by PennDOT, the interior beams were designed with a live-load distribution factor of $\frac{S}{5.5}$, where S is the center-to-center beam spacing, measured in feet. For the exterior beams the live-load distribution factor was based on the reaction of the wheel load obtained by assuming the slab to act as a simple span between beams. For this calculation the wheel load of the Standard AASHTO test vehicle is positioned to produce the maximum reaction at the exterior beam.

An investigation to study the problem of live-load distribution in spread box-beam bridges was initiated by Lehigh University in 1964. The first phase of the investigation was a field study of five spread box-beam type bridges. The conclusion of this study was that the provisions for lateral live-load distribution used by PennDOT did not give an accurate prediction when compared with test results. Therefore, a theoretical investigation was begun in 1967 to refine the method for predicting live-load distribution in the spread box-beam bridges. The result of this investigation was a new procedure which was adopted by AASHTO in 1973 (Art. 1.6.24).

In 1967 another field study was initiated to extend the results of the original work on spread box-beam bridges to include prestressed concrete I-beam bridges. The conclusion of this study of I-beam bridges was much the same as that of the box-beam bridges. The present AASHTO specification used by PennDOT for lateral live-

load distribution in I-beam bridges was not a realistic method. Thus, a theoretical investigation was initiated to develop a new method for the evaluation of live-load distribution factors for I-beam bridges. From this study a method of analysis to describe the behavior of I-beam bridges subjected to live loads was developed, as described herein.

1.2 Object and Scope of Study

The purpose of this investigation is to develop a refined method for the evaluation of live-load distribution factors for right, i.e., no skew, multi-beam bridges with prestressed concrete I-beams. The investigation is based upon a theoretical analysis technique developed at Lehigh University. The analysis technique is a finite element stiffness formulation for eccentrically stiffened plate structures in the linear elastic range. A short description of this finite element formulation is presented in Chapter 2.

Using the finite element technique different analytic models of I-beam bridges were compared with the results of the previous experimental study on I-beam bridges. Thus, the important design parameters of the bridge could be accounted for mathematically. The resulting analytic bridge model enabled an accurate and efficient study of live-load distribution. The analytic modeling study is presented in Chapter 3.

In Chapters 4 and 5 the design and results of an analytic

experiment to investigate live-load distribution are presented. It is from this analytic experiment that the design recommendation was obtained, as presented in Chapter 6.

1.3 Previous Studies

Load distribution in highway bridges has been studied for many years in this country and abroad. Though the work done has resulted in a greater understanding of the behavior of bridges, a number of simplifying assumptions were made in each case in order to overcome the mathematical difficulties involved in each of the solution procedures. Methods used to study the behavior of bridges have been grillage analysis, folded and orthotropic plate theories, finite difference method, finite strip method, and finite element method. Of all of the methods, the finite element method requires the fewest simplifying assumptions in accounting for the greatest number of variables which govern the structural response of the bridge. The technique chosen was an analysis scheme for stiffened plate structures developed at Lehigh University. This scheme utilized the finite element displacement approach.

It is not the purpose of this report to provide a discussion of previous work. An up-to-date annoted bibliography containing references which are directly or indirectly applicable to the structural behavior, analysis, and design of multi-beam type highway bridges was presented in a previous report[13] from this project.

2. ANALYSIS BY THE FINITE ELEMENT METHOD

2.1 Assumptions

The following assumptions were made in the finite element analysis of the bridge superstructures investigated as part of this research.

1. A small strain - small deflection theory was used.
2. Linearly elastic behavior of materials was assumed.
3. All superstructures were analyzed with simple supports. The effects of continuity were not included.
4. The longitudinal beams were prestressed concrete I-beams, either from Pennsylvania Standard[7] or from AASHTO-PCI Standard[1] cross-sections.
5. All loading conditions were static. No dynamic effects were considered.
6. The response of the slab was divided into out-of-plane and in-plane behavior. The out-of-plane behavior accounted for actions such as the normal stress associated with composite action of the beams and slab.
7. The in-plane and out-of-plane responses were superimposed.
8. The mid-plane of the deck slab was taken as the reference plane for the analysis technique.
9. The deck slab was assumed to have a constant thickness. Haunching for grade or camber was not included, nor was

the presence of permanent metal deck forms or the concrete below the top surface of the deck form. These are conservative assumptions.

10. Beams and slabs were assumed to act in a completely composite manner. Thus, the strain compatibility between the deck slab and the beam was maintained.
11. The beams were modeled as eccentric stiffeners to the slab.
12. The action of each beam was satisfactorily represented by a normal force, a bending moment about one axis, and a torsional moment. Weak-axis bending was ignored because of the relative stiffnesses of I-beam sections, and because only vehicular loading was considered.
13. The St. Venant torsional stiffness of the beams was considered. Warping torsion was assumed to be small because of the shape of the I-beams (Ref. 11). Appropriate values of the St. Venant torsional stiffness coefficient were computed and reported in Ref. 6.
14. The cross-sections of the structures analyzed in this research were reasonably proportioned. That is, for a particular structure, the beam size and spacing were appropriate for the span length, and the slab thickness was appropriate for the beam spacing.
15. The effect of the curb-parapet section was considered, as discussed in Sec. 3.3.4.

16. Intra-span diaphragms were not included in this analysis, since past research[9,11] has shown that while these diaphragms are effective in distributing the live load from a single vehicle, the effect becomes minimal when several lanes are loaded.

17. The number of loaded lanes conformed to section 1.2.6 of Ref. 1, as discussed in Sec. 4.2.

18. AASHTO type HS20-44 loading was used throughout the entire study. For spans up to 150 ft., a single HS20-44 vehicle was used. For spans in excess of 150 ft. a truck train used was the predecessor of the current lane loading, and is described in the Appendix B of Ref. 1. In deciding on the truck train, comparisons were made of the effects of a single HS20-44 vehicle, a truck train, and the lane loading. It was found that the lateral load distribution was not materially affected by the type of loading. Generally, there was less than 2% difference between the maximum and minimum distribution percentages produced by the three types of loadings. Therefore, the truck train was used for spans in excess of 150 ft., because the corresponding input could be handled automatically within the computer program.

2.2 Finite Element Analysis

The finite element method has three basic phases,

1) Structural Idealization

2) Evaluation of element properties

3) Assembly and analysis of the structural system.

In the current analysis, the beams and slab were treated separately, and then combined in the third phase. This presentation will follow the same pattern by discussing first the analysis of deck slabs, then the analysis of beams, and finally the assembly of beam and slab elements. This analysis is based on the formulation by Wegmuller and Kostem.[11,12]

2.2.1 The Deck Slab

As mentioned in Sec. 2.1, the response on the deck slab was further divided into out-of-plane (bending) and in-plane (membrane) actions.

2.2.1.1 The Out-of-Plane Behavior of the Deck Slab

The deck slab was analyzed using thin plate theory. Hence, the following assumptions were made:

1. Sections which were plane and normal to the middle surface before deformation remained plane and normal after deformation.
2. Transverse displacements were small compared to the plate thickness.

3. Since stresses normal to the plane of the plate were negligible, shearing stresses in the transverse direction were neglected, and the transverse displacement of any point on the plate was essentially the displacement of the corresponding point on the middle surface of the plate.

The deck slab was discretized into rectangular plate bending elements. The element developed by Adini, Clough, and Melosh was used. The plate elements were connected at node points. A node point was common to all of the elements which surrounded it. The displacements at the node points were the basic unknowns of the finite element stiffness analysis. There were three out-of-plane displacements assigned to each plate element node point. These displacements were the transverse displacement, W, and the bending rotations θ_x and θ_y. These displacements occured at the mid-plane of the plate. Thus, there were a total of twelve out-of-plane degrees of freedom (i.e., unknown displacements) associated with each plate bending element.

A polynomial displacement function was used to describe the displacements within the plate bending element.

$$W = \alpha_1 + \alpha_2 X + \alpha_3 Y + \alpha_4 XY + \alpha_5 X^2 + \alpha_6 Y^2 + \alpha_7 XY^2 \qquad (2.1)$$
$$+ \alpha_8 X^2Y + \alpha_9 X^3 + \alpha_{10} Y^3 + \alpha_{11} X^3Y + \alpha_{12} XY^3$$

The nodal rotations are given as derivatives of the transverse displacement, W.

$$\theta_x = \partial w/\partial y \tag{2.2}$$

$$\theta_y = - \partial w/\partial x \tag{2.3}$$

There are twelve unknown constants in Eq. 2.1 and twelve boundary conditions for each element: three displacements at each of four nodes. Substituting Eq. 2.1 into Eqs. 2.2 and 2.3, and then substituting the coordinates of the corners of the elements with respect to the element axes (shown in Fig. 1), the following equation is obtained:

$$\{\delta^e\}_o = [C]_o \{\alpha\} \tag{2.4}$$

the subscript "o" indicates out-of-plane displacements. The constants (α) are evaluated by matrix inversion.

$$\{\alpha\} = [C]_o^{-1} \{\delta^e\}_o \tag{2.5}$$

The strains within the element are related to the displacement field by the strain displacement equations. Within the context of the finite element method, strains and stresses are usually referred to as <u>generalized strains</u> and <u>generalized stresses</u>.

The generalized strains for out-of-plane behavior are the bending curvatures. Thus, it is possible to define the strains as:

$$\{\varepsilon\} = \begin{Bmatrix} \phi_x \\ \phi_y \\ \phi_{xy} \end{Bmatrix} = \begin{Bmatrix} -\partial^2 w/\partial x^2 \\ -\partial^2 w/\partial y^2 \\ 2\,\partial^2 w/\partial_x\,\partial_y \end{Bmatrix} \tag{2.6}$$

Substitution of Eq. 2.1 into Eq. 2.6 results in the matrix equation:

$$\{\varepsilon\} = [Q]\ \{\alpha\} \tag{2.7}$$

Substitution of Eq. 2.5 into Eq. 2.7 relates the generalized strains to the unknown nodal equations:

$$\{\varepsilon\} = [Q]\ [C]_o^{-1}\ \{\delta^e\}_o \tag{2.8}$$

Stresses are related to strains by an elasticity matrix:

$$\{\sigma\} = [D]\ \{\varepsilon\} \tag{2.9}$$

The stresses corresponding to the strains given by Eq. 2.6 are the bending moments per unit distance; M_x, M_y, and M_{xy}. Using the well-known equations of plate analysis (Ref. 8), the elasticity matrix is defined as:

$$\begin{Bmatrix} M_x \\ M_y \\ M_{xy} \end{Bmatrix} = \frac{Eh^3}{12(1-\nu^2)} \begin{bmatrix} 1 & \nu & 0 \\ \nu & 1 & 0 \\ 0 & 0 & \frac{1-\nu}{2} \end{bmatrix} \begin{Bmatrix} \phi_x \\ \phi_y \\ \phi_{xy} \end{Bmatrix} \tag{2.10}$$

where E is the modulus of elasticity of the plate, h is the plate thickness, and ν is Poisson's Ratio. Once these matrices have been defined, the well-established procedures of the finite element

method lead to the following stiffness matrix (Ref. 14):

$$[K]_o = [C]_o^{-1^T} \int_A [Q]^T [D] [Q] \, dx \, dy \, [C]_o^{-1} \tag{2.11}$$

The out-of-plane stiffness matrix, $[K]_o$ is given explicitly in Refs. 5, 11, and 14.

2.2.1.2 The In-Plane Behavior of the Deck Slab

The in-plane behavior of the plate is analyzed as a plane-stress elasticity problem. The discretization remains the same as discussed of out-of-plane behavior. There are two in-plane displacements at each node. The displacement in the x-direction (Fig. 1) is called U, the displacement in the y-direction is V. There are a total of eight in-plane degrees of freedom. The polynomial displacement functions are given by Eqs. 2.12 and 2.13.

$$U = \alpha_{13} + \alpha_{14} X + \alpha_{15} Y + \alpha_{16} XY \tag{2.12}$$

$$V = \alpha_{17} + \alpha_{18} X + \alpha_{19} Y + \alpha_{20} XY \tag{2.13}$$

As in the out-of-plane case, the eight unknown constants in Eqs. 2.12 and 2.13 are evaluated using the eight nodal displacements:

$$\{\delta^e\}_I = [C]_I \{\alpha\} \tag{2.14}$$

$$\{\alpha\} = [C]_I \{\delta^e\}_I \tag{2.15}$$

The generalized strains are taken as:

$$\{\varepsilon\} = \begin{Bmatrix} \partial u/\partial x \\ \partial v/\partial y \\ \partial u/\partial x + \partial v/\partial y \end{Bmatrix} = \begin{Bmatrix} \varepsilon_x \\ \varepsilon_y \\ \gamma_{xy} \end{Bmatrix} \tag{2.16}$$

Substitution of Eqs. 2.12 and 2.13 into 2.16 results in:

$$\{\varepsilon\} = [Q]\ \{\alpha\} \tag{2.17}$$

Substituting Eq. 2.15 into Eq. 2.19 results in the strain-displacement relations:

$$\{\varepsilon\} = [Q]\ [C]_I^{-1}\ \{\delta^e\}_I \tag{2.18}$$

The stresses are chosen as the membrane stresses σ_x, σ_y and τ_{xy}. The resulting elasticity matrix, based on the assumption of plane stress, is given by:

$$\begin{Bmatrix} \sigma_x \\ \sigma_y \\ \tau_{xy} \end{Bmatrix} = \frac{E}{1-\nu^2} \begin{bmatrix} 1 & \nu & 0 \\ \nu & 1 & 0 \\ 0 & 0 & \frac{1-\nu}{2} \end{bmatrix} \begin{Bmatrix} \varepsilon_x \\ \varepsilon_y \\ \gamma_{xy} \end{Bmatrix} \tag{2.19}$$

The basic matrices necessary to evaluate Eq. 2.13 are now known for the in-plane case, and the in-plane stiffness matrix, $[K]_I$, can now be evaluated. The in-plane stiffness matrix is also given explicitly in Ref. 11.

2.2.1.3 Superposition of In-Plane and Out-of-Plane Behaviors

Since analysis is based on a small deflection theory with linear material properties, as mentioned in Sec. 2.1, the in-plane and out-of-plane stiffness matrices may be superimposed as follows:

$$\begin{Bmatrix} F_I \\ F_o \end{Bmatrix} = \begin{bmatrix} K_I & 0 \\ 0 & K_o \end{bmatrix} \begin{Bmatrix} \delta_{e_I} \\ \delta_{e_o} \end{Bmatrix} \tag{2.20}$$

$[F]_I$ and $[F]_o$ are the in-plane and out-of-plane nodal force vectors, respectively.

2.2.2 The Beams

Figure 2 shows a beam element, nodal points, coordinate axes and degrees of freedom. The degrees of freedom consist of an in-plane axial displacement, U, out-of-plane bending displacements, W and θ_y, and a torsional rotation, θ_x at each node. Beam elements are positioned between plate nodes in the x-coordinate direction.

The in-plane and out-of-plane response of beam elements are considered simultaneously. The torsional response is treated separately.

2.2.2.1 The In-Plane and Out-of-Plane Behavior of Beams

The polynomial displacement functions for the response of beam element not including the effects of torsion are given by:

$$U = \alpha_{21} + \alpha_{22} X \tag{2.21}$$

$$W = \alpha_{23} + \alpha_{24} X + \alpha_{25} X^2 + \alpha_{26} X^3 \tag{2.22}$$

These displacements occur in the same reference plane that is used for calculation of the plate displacements (Fig. 2). In this formulation the reference plane was the mid-plane of the deck slab. It should be noted that Eqs. 2.21 and 2.22 have the same form as Eqs. 2.12 and 2.1 when the coordinate y is equal to a constant. This fact, combined with a choice of beam eccentricity referenced to the mid-plane of the deck slab, provides strain compatibility between the deck slab and the beam. This is necessary to correctly model composite beam-slab bridges. The bending rotation, θ_y, is defined by Eq. 2.3.

The six unknown constants in Eqs. 2.21 and 2.22 are evaluated using the six nodal displacements, three at each end of the beam:

$$\{\delta^e\}_B = [C]_B \{\alpha\} \tag{2.23}$$

$$\{\alpha\} = [C]_B^{-1} \{\delta^e\}_B \tag{2.24}$$

The generalized strains are taken as the bending curvature and axial strain.

$$\{\varepsilon\} = \begin{Bmatrix} dy/dx \\ - d^2w/dx^2 \end{Bmatrix} \tag{2.25}$$

the generalized stresses corresponding to these strains are the axial force and bending moment.

$$\{\sigma\} = \begin{Bmatrix} N \\ \\ M \end{Bmatrix} \tag{2.26}$$

The strain in the beam can be related to Eq. 2.25 as shown in Fig. 3.

$$\bar{\varepsilon} = \frac{du}{dx} - Z \frac{d^2w}{dx^2} \tag{2.27}$$

The bar indicates that the strain is referred to the reference plane. The stress is equal to Young's modulus times the strain.

$$\bar{\sigma} = E \bar{\varepsilon} = E\left[\frac{du}{dx} - Z \frac{d^2w}{dx^2}\right] \tag{2.28}$$

The generalized stresses are related to $\bar{\sigma}$ by the integrals:

$$N = \int_A E \bar{\sigma} \, dA = E \frac{du}{dx} \int_A dA - E \frac{d^2w}{dx^2} \int_A Z \, dA = E \bar{A} \frac{du}{dx} - E \bar{S} \frac{d^2w}{dx^2} \tag{2.29}$$

$$M = \int_A E Z \bar{\sigma} \, dA = E \frac{du}{dx} \int_A Z \, da - E \frac{d^2w}{dx^2} \int_A Z^2 \, dA = E \bar{S} \frac{du}{dx} - E\bar{I} \frac{d^2w}{dx^2} \tag{2.30}$$

The elasticity matrix is defined by using Eqs. 2.29 and 2.30:

$$\begin{Bmatrix} N \\ M \end{Bmatrix} = \begin{bmatrix} \bar{A} & \bar{S} \\ \bar{S} & \bar{I} \end{bmatrix} \begin{Bmatrix} dy/dx \\ - d^2w/dx^2 \end{Bmatrix} \tag{2.31}$$

The bars in Eq. 2.31 indicate that the appropriate quantities are referred to the reference plane, not necessarily to the centroidal

axis of the beam.

Substituting Eqs. 2.21 and 2.22 into Eq. 2.25 leads to the definition of [Q]. Once this is done, all of the matrices are defined to evaluate the nontorsional stiffness matrix of the eccentric beam element:

$$[K] = [c]_B^{-1^T} \int_\ell [Q]^T [D] [Q] \, dx \, [c]_B^{-1} \tag{2.32}$$

The beam stiffness matrix above is given explicitly in Ref. 11.

2.2.2.2 The Torsional Behavior of the Beams

The St. Venant torsional stiffness of the prestressed concrete I-beams is included in the analysis. The warping torsion effects are neglected. The St. Venant torsional moment can be related to the unit angle of twist by:

$$T_{sv} = GK_T \, \phi' \tag{2.33}$$

The unit angle of twist can be related to the axial rotation of the beam by:

$$\{\varepsilon\} = \phi' = \frac{\partial}{\partial x} \theta_x = \frac{\partial}{\partial x} \frac{\partial w}{\partial y} \tag{2.34}$$

Substitution of the displacement function for the plate (Eq. 2.1) into Eq. 2.34 results in the assumed displacement function for θ_x along a line defined by a constant y coordinate.

$$\theta_x = \frac{\partial w}{\partial y} = \alpha_{27} + \alpha_{28} X \tag{2.35}$$

The elemental displacement vector consists of values of θ_x at each end of the beam. Thus, a connection matrix analogous to Eqs. 2.4, 2.14, 2.15, and 2.23 can be defined.

$$\{\delta_e\}_T = [C]_T \{\alpha\} \tag{2.36}$$

$$\{\alpha\} = [C]_T^{-1} \{\delta_e\}_T \tag{2.37}$$

The generalized stress and strain are the torsional bending moment and the unit angle of twist, respectively. Thus, an elasticity matrix is defined as shown above.

$$\{T\} = [GK_T] \{\phi'\} \tag{2.38}$$

The matrix [Q] is again defined by substituting the displacement functions given by Eq. 2.35 into the definition of strain given by Eq. 2.34. When this is done, all of the matrices needed to define the stiffness matrix are known, and evaluation may proceed. An explicit torsional stiffness matrix is given in Ref. 11.

2.3 Assembly of Elements

The assembly of elements in the finite element method is analogous to the assembly of member-stiffness matrices in conventional matrix structural analysis. The slab element stiffness matrix relates a force at one node to the displacements of the remaining nodes in that element. Each node may be surrounded by as many as four slab elements which join that node. Thus, a force at one node may be related to the displacements of all the nodes in four elements. This means that, including the fact that some nodes will be common to the adjoining elements, a total of 9 nodes having forty-five degrees of freedom could be related to the single force component. The process of relating the force to all of the adjoining ele-

ments and their degrees of freedom is called assembly of the global stiffness matrix. The problem of finding the appropriate node points related to a given node point is a matter of specifying structural topology to the computer program which actually performs the arithmetic operations, and will not be discussed in this report.

The superposition of beam stiffness components is accomplished by straight-forward addition of corresponding beam and slab element stiffness components. This includes isolating the nodes to which beam elements are attached. The force at a node having a beam element is related to the beam displacements at the adjacent nodes in the x-direction. This is also a matter of topology which is specified as input to the computer program, and will not be discussed in this report.

2.4 Solution and Back Substitution

The assembly of the element stiffness matrices results in a set of simultaneous equations relating nodal forces to nodal displacements. These equations are solved for the nodal displacements after the boundary conditions are enforced. Once the displacements are known, it is possible to back-substitute them into appropriate equations to compute the generalized stresses. Thus, substitution of nodal displacements into the beam stiffness matrix results in the normal force, bending moment, and torsional moment at the beam node points. These forces act at the plane of reference, i.e., the midplane of the plate. This fact is important in evaluating the lateral load distribution in bridges.

Substitution of the appropriate nodal displacements into Eq. 28 followed by substitution of the results into Eq. 2.9, enables the evaluation of the unit bending moments M_x, M_y, and M_{xy} at the node points. The inplane stresses (or forces) can be evaluated in a similar manner.

2.5 Computation of Moment Percentages

A moment percentage is defined as the bending moment carried by one beam where the beam can be considered as the total composite cross-section, divided by the total of the moments carried by all the beams, and multiplied by 100. The moment carried by one composite cross-section is given by:

$$M_c = \int_{beam} \sigma_x Z \, dA + \int_{slab} \sigma_x Z \, dA \qquad (2.39)$$

where Z is a coordinate from any reference plane. If the reference plane is chosen as the mid-plane of the plate, Eq. 2.39 may be rewritten as:

$$M_c = M_{x_{beam}} + \int_o^{b_{eff}} (M_{x_{slab}}) \, d\ell \qquad (2.40)$$

in which b_{eff} is the effective width of the slab. It was noted in Sec. 2.2 that provisions were made to reference the beam moment to any arbitrary reference plane, including the mid-plane of the plate. It is this moment which is found by back-substitution, as discussed in Sec. 2.2.4.

The problem of finding the effective flange width is simplified by the relative sizes of the unit slab bending moment, $M_{x_{slab}}$, and the beam bending moment about the mid-plane of the plate. The total slab moment across the bridge width is only a small percentage of the total of the composite beam moments. Sample calculations indicate that for multi-beam bridges, the total slab moment is generally $\leq$ 5% of the total. Therefore, the effect of a small error in the effective flange width is an insignificant difference in the moment percentages as calculated in this research. Therefore, the following approximate effective flange widths were used in lieu of more exact calculations:

1. For interior beams, the actual beam spacing was used.
2. For exterior beams, one half of the spacing, plus the over-hang was used.

Having the effective flange width and choosing the slab moment at the node over the beam as representative width of the superstructure, Eq. 2.40 reduces to:

$$M_c = M_{beam} + (M_{x_{slab}}) (b_{eff}) \tag{2.41}$$

The moment percentage of one beam is then calculated as:

$$M_{pi} = \frac{M_{c_i}}{\sum_{i=1}^{n} M_{c_i}} \tag{2.42}$$

in which i denotes the beam in question and n is the total number of beams. These moment percentages were used to produce influence lines for a given bridge. These influence lines were then loaded to determine the maximum distribution factor for a given bridge.

3. ANALYTIC MODELING STUDY

3.1 Purpose of Analytic Modeling Study

The finite element technique described in Chapter 2 of this report was used in the study of lateral load distribution in I-beam bridges. A preliminary study was undertaken to investigate different methods of analytically modeling the I-beam bridges so as to use the finite element method effectively and efficiently. In this study the analytic models were compared to the field test results[3,4,9,10] of two in-service I-beam bridges located near Lehighton and Bartonsville, Pennsylvania.

The results of the analytic modeling study were threefold. First, important design parameters of a bridge were isolated, described, and analyzed using analytic approximations. Thus, the influence of these design parameters such as the curb-parapet section and permanent metal deck forms were taken into account. Second, the analysis was verified by comparison with the results from the field tests. Third, the analytic bridge model was refined, to enable an accurate and efficient study of lateral load distribution.

3.2 Description of Field Test Bridges

The field testing of the Lehighton and Bartonsville bridges analyzed in this investigation is described in detail by Chen and VanHorn,[3,4,9] and Wegmuller and VanHorn.[10] Initially, only the field

test results of the Lehighton bridge were used in comparison with different analytic models. The reason for the emphasis on the Lehighton bridge was two-fold. First, the Lehighton bridge was tested both with and without midspan diaphragms between beams. Second, there was only one curb-parapet section on the Lehighton bridge, which allowed the effect of the curb-parapet section on load distribution to be seen more readily. The Bartonsville bridge test results were then compared to an analytic model which included all of the features of modeling discussed in this chapter which are appropriate to the Bartonsville bridge.

The cross-section of the Lehighton Bridge is shown in Fig. 4. The main supporting members were six identical PennDOT 24/45 prestressed concrete I-beams spaced 6 feet 9 inches center-to-center. The slab was cast-in-place over a permanent metal deck form, with a nominal thickness of 7-1/2 inches. With a curb and parapet section on only one side of the superstructure, the roadway width was 33 feet 9 inches. The span length was 71 feet 6 inches, center-to-center of bearings.

The cross-section of the Bartonsville Bridge is shown in Fig. 5. The main supporting members were five identical AASHTO Type III prestressed concrete I-beams spaced 8 feet center-to-center. The slab was cast-in-place with a nominal thickness of 7-1/2 inches. The roadway width was 32 feet. The span length was 68 feet 6 inches, center-to-center of bearings.

3.3 Analytic Modeling

3.3.1 Discretization of the Superstructure

Using the finite element technique, the actual bridge was modeled by a discretized bridge containing a suitable number of finite elements. Figure 6 shows the cross-section of the test bridge. Also shown is the plan view of the bridge, with the discretization indicated. The lines indicate boundaries between elements, and the intersections of those lines are nodal points. The beams were also discretized into beam elements, connected at the appropriate nodal points. In the discretization shown in Fig. 6, there are two plate elements between the beams. In the analytic modeling study, the discretization was varied according to the requirements of a particular analytic model.

In comparing the analytic and field test results, the moments at a cross-section called the maximum moment section of the bridge were used. The maximum moment section, shown as section M in Fig. 6, is the section at which the absolute maximum moment would occur in a simple beam of the same span as the bridge, when loaded with the test vehicle. The test vehicle, which closely approximated the AASHTO HS20-44 design vehicle, is shown in Fig. 7.

Comparisons of different analytic models were made using moment percentage diagrams. The definition of moment percentage for a particular beam is defined in section 2.3 of this report.

3.3.2 Refinement of Slab Discretization

Figure 8 shows a typical segment of the cross-section of the test bridge. The figure shows that portions of the slab are supported by the relatively stiff flange of the I-beams. Because of the support provided by the flanges, the first investigation undertaken was the analytic modeling of the effective bending span of the slab between the beams.

Two different models were used to model the effective bending span of the slab. The first model was a mathematical approximation that was an accurate and efficient modeling technique. The second model was a theoretically better approximation, but was a far less efficient model. Though this second model would not be used in an extensive study, it was used here to verify the first modeling technique.

The first model, shown in Fig. 8, consisted of nodes positioned above the center of the beams and midway between the beams. This discretization, which consisted of two slab elements between beams, was designated the 2PL mesh. Using this discretization, the effective bending span was approximated by introducing an orthotropy factor (Dy) in the analysis. This factor was defined as the ratio of the transverse-to-longitudinal stiffness of a unit area of slab. The orthotropy factor was calculated as the square of the ratio of the center-to-center beam spacing to the flange-to-flange spacing.

As shown in Fig. 8, the orthotropy factor calculated for the Lehighton Bridge was 1.69.

The moment percentage diagram shown in Fig. 9 is a comparison of two analytic models with the field test results. One model included the orthotropy factor in the analysis, while the other did not. As shown in Fig. 9, the test vehicle is located between the third and fourth beams, as indicated by the wheels and axle. Comparison of the analytic models with the field test results showed that a closer correlation to the field test results was obtained when the orthotropy factor was included in the analysis.

To verify that this method was an effective way of modeling the bending span of the slab, a comparison was made with another theoretical model. The discretization for the latter model is shown in Fig. 10. There are four slab elements between the beams, with two elements over the flange of each beam, and two elements between the flanges of the beams. This discretization was designated the 4PL mesh. The slab elements over the flanges of the beams were assigned an orthotropy factor of 100.0. This orthotropy factor defined the stiffness of the slab elements, above the beam flanges, in the transverse direction to be 100 times greater then stiffness in the longitudinal direction. In effect, the slab elements above the flanges were allowed to deform in the longitudinal direction, while essentially remaining rigid in the transverse direction. This prevented relative deformation of the slab with respect to the beam flange in

the transverse direction. The elements between the beams were assigned an orthotropy factor of 1.00, therefore those elements would deform in an isotropic manner.

In Fig. 11, the results from use of the 4 PL mesh are compared with those from the 2 PL mesh. The position of the test vehicle is indicated. It is seen in this comparison that both models yielded virtually the same results. Thus, the methods of modeling the appropriate bending span were verified. Based on the comparison, the 2 PL mesh was selected for the remainder of the study because it was as equally effective as and more efficient than, the 4 PL model in representing the bending span of the slab.

A further investigation was then performed to determine the effect of a different slab discretization on the analysis. The discretization in Fig. 12(a) is the 2 PL mesh, described earlier in this section, while the discretization in Fig. 12(b) has one slab element between the beams, and will be designated the 1 PL mesh. Both of these models contain the appropriate orthotropy factors and results from their use are compared in Figs. 13 & 14. Two different truck positions are indicated. These figures both show that there was no perceptible difference between either of the modeling techniques.

3.3.3 Permanent Metal Deck Form

The concrete slab of the test bridge was placed over a permanent metal deck form which had ribs running in the transverse direction (Fig. 15). The effects of the deck form on lateral load distribution were modeled by introducing another orthotropy factor (Dy). As indicated in Fig. 16 the orthotropy factor was calculated as the ratio of moments of inertia I'/I, where I' was defined as the moment of inertia of the transformed concrete section and the metal deck form in the transverse direction, and I was the moment of inertia of the concrete slab of nominal thickness in the longitudinal direction. For the test bridge, the orthotropy factor was calculated as 1.48. The effect of including this factor in the analysis is shown in Fig. 17. When the permanent metal deck form was included in the analysis, the agreement between analytic and field test results was improved.

3.3.4 Curb-Parapet Section

In order to verify that the analytic model accurately represented the actual superstructure behavior, it was also necessary to make an investigation to assess the effect of the single curb-parapet section, shown on the right side of the cross-section in Fig. 4. The curb-parapet section was considered as a beam element in the analysis. Two different models of the section were studied ; (1) The section, shown in Fig. 18, was considered to be

fully effective. (2) The section was considered to be partially effective. That is, only the cross-sectional properties up to the dashed line were considered, as indicated in Fig. 18. In the actual bridge, the curb-parapet section was interrupted by deflection joints one inch in width at intervals of approximately 14 feet along the span length. The joints were filled with a pre-molded joint filler in the portion of the section between the top of the slab and the dotted line. Therefore, the two models represented the upper and lower bounds of effectiveness.

Both modeling techniques are compared to the field test results in Figs. 19, 20, and 21. Each figure corresponds to a different truck position. It is seen in Fig. 19 that there is very little difference between results from the models. This was expected for a truck position which was as far as possible from the curb-parapet section. In this case the bending moments in the beams in the vicinity of the curb-parapet are negligible, and therefore, the influence of the curb-parapet would be small. In Fig. 20 the test vehicle is placed between the third and fourth beams of the bridge. For this load case, there was a noticeable difference between the fully effective and partially effective models. Use of the partially effective section produced results which correlated better with the field test than those obtained with the fully effective section. In Fig. 21 the truck is positioned as close as possible to the curb-parapet section.

With this position of the truck, use of the fully effective curb-parapet section, resulted in an over-estimation of the moment carried by the exterior beam under the curb-parapet section, while use of the partially effective curb-parapet section, yielded very good correlation with the field test results. Thus, it was concluded that the effect of the curb-parapet section on lateral load distribution increases as the load approaches that section. These studies have also indicated that the partially effective section is a more realistic model of the curb-parapet than a fully effective section.

3.4 Summary

A study of different analytic modeling techniques has been presented. In this study, an accurate and efficient model was developed for use in the study of lateral load distribution. Figures 22 and 23 show the correlation between analytic and field test results for two additional load cases on the Lehighton Bridge. Figures 24 and 25 compare analytic and field test results for two load cases on the Bartonsville Bridge. The difference between the analytic and field test results is no greater than 6% for any load case.

Based on this study, the following conclusions are drawn:

1) The permanent metal deck form and the top flanges of the beams stiffen the slab in the transverse direction. This stiffening effect can be accounted for by using an orthotropy

factor. Suggested methods of computing these orthotropy factors are presented in Sec. 3.3.2 and Sec. 3.3.3.

2) The number of elements between beams can be reduced with a considerable increase in efficiency, but without a significant loss in accuracy.

3) The curb-parapet section affects the distribution of live load. The results from this preliminary study indicate that a partially effective curb-parapet model yields more realistic results than a fully effective model.

4. DESIGN OF ANALYTIC EXPERIMENT

4.1 General

To obtain a general method for the evaluation of distribution factors that will be reliable for all bridges over a range of different dimensions, many bridges were considered in the investigation. Although field tests were important in establishing the validity of analytical techniques, an investigation of the size required in this study eliminates the possibility of sufficient field testing to provide the basis for a general specification provision. Therefore, an analytic experiment was designed to yield information which would form the basis for development of new design provisions for live-load distribution factors. In this analytic experiment, approximately 300 bridges were designed and analyzed. The experiment was a computer based analytic simulation. The analytic simulation was accomplished by using the theoretical technique described in Chapter 2, which incorporated the analytic model developed in Chapter 3.

4.2 Type of Superstructure and Loading Configuration

The bridges that were considered in the analytic experiment were all simple-span, without skew. The bridges consist of a reinforced concrete deck slab supported longitudinally by equally spaced prestressed concrete I-beams. The effects of the curb-parapet section and the intra-span diaphragms were neglected. All

bridges were designed using the provisions of the 1973 AASHTO specification, and the PennDOT Standards for bridge design, BD-201 and AASHTO HS20-44 truck loadings were used.

4.3 Bridge Dimensions and Variation of Parameters

The following bridge design parameters were varied in the analytic experiment. A representative range of bridge widths were chosen, using Sec. 1.2.6 of the 1973 AASHTO specification as a guide. The bridge widths used were 20, 30, 42, 54, 66, and 78 ft. For each bridge width, the number of beams was varied, which provided a range in beam spacing. The beam spacings varied from 4'-0" to 10'-6". For each beam spacing, the length of the bridge was varied from approximately 30 ft. to approximately 150 ft. The slab thickness used for each case was the thickness appropriate for the beam spacing and length, as specified in PennDOT BD-201. The bridges were designed using the stiffest, straight-strand, economical (smallest cross-sectional area) beam shape. Both PennDOT and AASHTO prestressed I-beam shapes were used.

Tables 1, 2, and 3 give an overall scope of the range of the analytic experiment. Table 1 indicates the range for the 20 ft. and 30 ft. wide bridges, and Tables 2 and 3 show the range for the 42, 54, 66, and 78 ft. wide bridges respectively. For each bridge width, the tables indicate the range of the number of beams, the beam spacing in feet, the minimum and maximum lengths and the

number of bridges actually analyzed for a given bridge width.

Table 4 demonstrates the scheme used to vary the bridge parameters in the analytic experiment. The table provides a detailed outline of the experiment for all bridges that are 20 ft. in width. Each X represents a bridge that was designed and analyzed. Across the top of the table, the number of beams is varied from 3 to 6. On the left hand side of the table, the S/L ratio is indicated. The quantity S/L is the ratio of beam spacing to span length. Thus, for a 3-beam bridge with a beam spacing of 10 ft. and a span length of 30 ft. the S/L ratio is 1/3. For the same beam spacing, if the span length is increased to 150 ft., the S/L ratio is 1/15. The S/L ratios were varied from about 1/3 to 1/30 for each particular beam spacing. As shown in Tables 5-9, this technique was used for other bridge widths included in the analytic experiment. The results of the experiment are presented in Chapter 5.

5. RESULTS OF THE EXPERIMENT

5.1 General

The design of an extensive analytic experiment to study lateral load distribution was presented in Chapter 4. This chapter presents the method in which the results of the bridge analyses were utilized to arrive at a new equation for determination of lateral load distribution in prestressed concrete I-beams, simple span, no-skew highway bridges.

The following is a brief outline of the steps involved in the determination of the lateral load distribution developed in this research.

1) Analyze the bridges listed in Chapter 4.
2) Obtain influence lines for each beam of each bridge.
3) Calculate the maximum distribution factor for each bridge for a number of loaded lanes from one to the number as set forth in section 1.2.6 of Ref. 1.
4) Plot maximum distribution factors versus the S/L ratio.
5) Determine a new lateral load distribution equation by fitting the data plotted in step 4 with an appropriate equation.

5.2 Analysis of Bridges and Resulting Influence Lines

The finite element method described in Chapter 2 was the

method used to analyze the bridges in the experiment. A single HS20-44 vehicle was placed in a number of positions across the width of the bridge, and an analysis was performed for each position. The longitudinal position of the vehicle was always the one that would produce an absolute maximum moment in an analogous single beam of length equal to the span length of the bridge. The bridge was discretized in such a way that the maximum moment was obtained directly in the analysis.

For each position of the vehicle, a moment percentage diagram was obtained, similar to the diagrams used in Chapter 3. The moment percentage diagrams were then used to produce the influence lines for each beam. Each influence line was plotted using approximately ten vehicle positions across the width of the bridge. These influence lines were then used to produce the distribution factors for each beam.

The technique of obtaining the influence lines for beams can be illustrated by using one of the 219 bridges that were analyzed in the experiment. This bridge was 42 ft. in width and 105 ft. in length. There were 7 beams spaced at 7 ft.. Influence lines for the exterior beam and center beam are shown in Fig. 26 and 27, respectively. The lines were developed using eleven vehicle positions.

5.3 Determination and Plotting of Maximum Distribution Factors

This section explains how the maximum distribution factor for each bridge was determined, using the influence lines. As explained in Chapter 4, each bridge width that was included in the experiment, except the 20 foot wide bridge, was considered as two design lane configurations. For example, the 42 foot wide bridge was considered as a three and four lane structure, as set forth in Sec. 1.2.6 of Ref. 1. Shown in Figs. 26 and 27 are the positions of the design traffic lanes when the example bridge was considered as a three-lane and then four-lane structure. Thus, two maximum distribution factors were developed from the analysis of every bridge.

Considering the example bridge as a three-lane structure, the following method was used to calculate the maximum distribution factor for the center beam (Fig. 27). A vehicle was placed in each of the three lanes. The vehicles were positioned within their individual traffic lanes so as to produce the maximum moment percentage in each lane. These values were then summed to produce the maximum summation of moment percentages for the center beam. The summation was then multiplied by two to convert the vehicle axle load to wheel loads. This calculation produced the maximum distribution factor for the center beam of the bridge when the structure was considered as a three-lane bridge.

To obtain the maximum distribution factor for the interior beams of the bridge, this process was repeated for the remainder of the interior beams. The calculated distribution factors were then compared to determine the maximum distribution factor for the interior beams of the example bridge using a three-lane configuration. The example bridge was then considered as a four-lane bridge and the complete process was repeated. The calculations for the example bridge yielded a maximum distribution factor of 1.16 for the three-lane case and 1.38 for the four-lane case.

Fig. 26 shows the influence line for the exterior beam of the example bridge. The distribution factors for the exterior beam were calculated using the same technique as used for the interior beams. The maximum exterior beam distribution factors were obtained by again calculating distribution factors for the three and four-lane case.

Though the calculations for the interior and exterior beams were similar, the influence line for the exterior beam serves as a good example to demonstrate the care required in calculation of the maximum distribution factor. As shown in Fig. 26 for the three-lane case, one of the three lanes is positioned where negative moment is produced. If this negative moment percentage was included in the summation, the maximum distribution factor would not be obtained. Therefore, this negative value was excluded from the sum-

mation. The case in which two of the three lanes were loaded was more critical for this case, and was the loading used in calculating the maximum distribution factor for the beam.

This process for calculating the maximum distribution factor was repeated for all of the 42 foot wide, 7 beam bridges listed in table 6 resulting in the list in table 10. The bridge lengths ranged from 42 feet to 105 feet. The distribution factors ranged from 1.38 to 1.42 for the four-lane case. The results in table 10 are shown in graphical form in Fig. 28. The maximum distribution factor for each bridge is plotted against the beam spacing-to-span length ratio of the bridges. Figure 28 shows only the results of the 42 foot wide, 7 beam bridges. In Fig. 29, the maximum distribution factors for all of the 42 ft. wide bridges listed in table 7 are shown. Plots of maximum distribution factors were obtained for all 219 bridges studied. It was from these plots that the new method for calculating the distribution factor for interior and exterior beams was obtained.

5.4 Distribution Factors

Separate provisions currently exist for the calculation of distribution factors for interior and exterior beams in Ref. 1. The results for interior and exterior beams obtained in this research are also presented separately. Figures 30 to 40 are plots of the maximum distribution factors for interior beams. Figures

41 to 51 are plots of the maximum distribution factors for exterior beams. The plots, which include results for 219 bridges, are grouped by bridge widths and number of design lanes considered. They include the complete range of beam spacings considered for each width. The solid lines represent the computer analysis. The dashed lines represent the analytic expression that approximates the computer results.

5.5 Summary

In this chapter, the method of obtaining the maximum distribution factors for the bridges studied was presented. The final plots presented in section 5.4 were obtained after 219 bridge analyses were performed which included a total of approximately 1500 vehicle load cases. From these analyses, approximately 1200 influence lines were studied under many lane load configurations to determine new lateral load distribution equations for the interior and exterior beams. These equations are presented in chapter 6.

6. DISTRIBUTION FACTORS

6.1 Interior Beams

The analytic expression which was developed to calculate the live-load distribution factor for interior beams is presented in this section.

Figures 30 to 40 are plots of maximum distribution factors versus S/L (ratio of beam spacing-to-span length ratio) for the interior beams. The solid lines represent the computer analysis results, while the dashed lines represent the analytic expression that approximates the computer results. The figures show the results obtained for the complete range of bridge widths studied. The 42 ft. wide bridge distribution factors will serve as a representative sample of the trends that are apparent in the figures.

Figure 33 is the plot of maximum distribution factors for bridges that are 42 ft. wide and with 3 design lanes, while Fig. 34 is the plot of maximum distribution factors for the same bridges except that the bridges have 4 design lanes. As expected the following trends are apparent when the figures are compared.

1) As the length of the bridge increases the distribution factor decreases.
2) As the number of beams increase the distribution factor decreases.

3) The distribution factors for the 4 design lane case are higher than those for the bridges considered as 3 design lanes.

The analytic expression for evaluating distribution factors contains provisions accounting for the above referred trends. Of the many equations studied to approximate the experimental distribution factors for interior beams, the following equation produced consistent correlation with the experimental results:

$$DF = \left(W_c + \frac{W_c}{N_B} - \gamma\right) \frac{1}{\beta} - 0.45 \left(0.25 - \frac{S}{L}\right)$$

$$\gamma = 0.3 \left(W_c - W_{min}\right)$$

$$\beta = 4.7 \, N_B$$

where

W_c = roadway width between curbs, in ft.

N_B = number of beams

S = beam spacing, in ft. ($4.5 \leq S \leq 10.5$)

L = span length, in ft. ($30.0 \leq L \leq 150.0$)

W_{min} = minimum curb to curb width which qualifies as an N_L design lane bridge, in ft.

N_L = number of design lanes

The distribution factors that are calculated using this equation are shown in figs. 30 - 40 by the dashed lines. A comparison of the results of the computer analysis ($DF_{comp.}$) and the analytic expression ($DF_{anal.exp.}$) is made using the ratio

$DF._{anal.exp.}/DF._{comp.}$ Using this ratio a mean of 104% was calculated. That is, the analytic expression is, on the mean, 4% higher than the computer analysis. The standard deviation is 4%. Thus there is a 95% probability that the results using the equation will be between 96% and 112% of the experimental results.

6.2 Exterior Beams

The maximum distribution factors for the exterior beams are plotted in figs. 41 to 51. For the exterior beams, the maximum distribution factors are plotted versus span length. The solid lines represent the computer analysis results, while the dashed lines represent the analytical expression approximating the computer results. As expected, the following trends, similar to those for the interior beams became apparent when the figures are compared.

1) The distribution factor increases as the length of the bridge increases.
2) The distribution factor decreases as the number of beams increases.
3) As the number of lanes increases, for a given width, the distribution factor increases.

The following equation approximates the computer analysis results:

$$D.F. = \frac{S}{10} + \frac{L}{750} + 0.1$$

where

S = beam spacing, in ft. ($4.5 \leq S \leq 10.5$)

L = span length, in ft. ($30.0 \leq L \leq 150.0$)

The distribution factors that are calculated using this equation are shown in figs. 41 - 51 by the dashed lines.

7. SUMMARY AND CONCLUSION

7.1 Summary

A method of analysis based on the finite element method is presented in Chapter 2. A review of the assumptions and limitations of the previously developed analysis technique is discussed and the analysis technique is then described.

In Chapter 3 comparisons are made between results from the theoretical analysis technique, and values yielded from the field testing of two in-service bridges. Different methods of analytically modeling the bridges were used in comparison with the field test results. Through these comparisons, the validity of the theoretical analysis technique was verified. Also, by refining the analytic bridge model, the accuracy and efficiency of the study of live load distribution was increased.

An analytic experiment to study live load distribution is presented in Chapter 4. 219 different bridges were designed and analyzed under AASHTO HS20-44 design loading. Chapter 5 shows how the results of the bridge analyses which constituted the analytic experiment were utilized to arrive at a new equation to describe the lateral load distribution.

In Chapter 6 a design recommendation for the determination of lateral live-load distribution is presented. Separate procedures

are given for the interior and exterior beams.

7.2 Conclusions

Very good agreement was obtained between the theoretical analysis technique and the field test results. Through an analytic modeling study the analytic bridge model used was refined so that optimum accuracy and efficiency were obtained.

Based on the results of the analyses of 219 bridges the following conclusions can be made.

1. The lateral live-load distribution in prestressed concrete I-beam bridges can be accurately described by the equations presented in Chapter 6. The behavior of interior and exterior beams is described by separate equations.
2. The span length of the bridge, the beam spacing, and the number of design traffic lanes are very important factors in determining the live-load distribution factors.
3. The effect of the curbs and parapets were not considered in the development of the equations to describe lateral live-load distribution. However, based on the results of the analytic modeling study, it was found that the curbs and parapets do have an influence on the distribution of live-load. Therefore, it is felt the design procedures should be modified to permit the effect of curbs and parapets to be considered.

8. TABLES

Roadway Width: 20 feet				
No. Beams	Space	L_{MAX}	L_{MIN}	No. Bridges
3	10'-0"	80'	40'	5
4	6'-8"	116'-8"	40'	7
5	5'-0"	100'	40'	6
6	4'-0"	120'	48'	6
				Tot. = 24

a)

Roadway Width: 30 feet				
No. Beams	Space	L_{MAX}	L_{MIN}	No. Bridges
4	10'-0"	80'	40'	5
5	7'-6"	90'	37'-6"	6
6	6'-0"	120'	42'	7
7	5'-0"	125'	50'	6
8	4'-3"	127'-6"	51'	6
				Tot. = 30

b)

TABLE 1 RANGE OF BRIDGE DESIGN PARAMETERS

Roadway Width: 42 feet				
No. Beams	Space	L_{MAX}	L_{MIN}	No. Bridges
5	10'-6"	84'	42'	5
6	8'-5"	101'	42'-1"	6
7	7'-0"	105'	42'	6
8	6'-0"	120'	42'	7
9	5'-3"	105'	42'	6
10	4'-8"	116'-2"	46'-8"	6
				Tot. = 36

a)

Roadway Width: 54 feet				
No. Beams	Space	L_{MAX}	L_{MIN}	No. Bridges
6	10'-10"	108'-4"	32'-6"	6
7	9'-0"	108'	36'	6
8	7'-9"	116'-3"	38'-9"	6
9	6'-9"	135'	40'-6"	7
11	5'-5"	135'-5"	37'-10"	7
13	4'-6"	135'	36'	7
				Tot. = 39

b)

TABLE 2 RANGE OF BRIDGE DESIGN PARAMETERS

Roadway Width: 66 feet				
No. Beams	Space	L_{MAX}	L_{MIN}	No. Bridges
8	9'-5"	113'	37'-8"	6
9	8'-3"	123'-9"	33'	7
10	7'-4"	128'-4"	29'-4"	8
12	6'-0"	120'	36'	7
14	5'-1"	127'-1"	50'-10"	6
16	4'-5"	132'-6"	53'	6
				Tot. = 40

a)

Roadway Width: 78 feet				
No. Beams	Space	L_{MAX}	L_{MIN}	No. Bridges
9	9'-9"	117'-8"	39'	7
10	8'-8"	104'	34'-8"	7
11	7'-10"	117'-6"	39'-2"	7
12	7'-1"	124'	35'-5"	7
13	6'-6"	130'	32'-6"	8
15	5'-7"	111'-8"	39'-1"	7
17	4'-11"	123'	39'-4"	7
				Tot. = 50

b)

TABLE 3 RANGE OF BRIDGE DESIGN PARAMETERS

Roadway Width 20 feet

(2 design lanes)

No. Beams	6	5	4	3
S/L				
1/30	X			
1/25	X			
1/20	X	X		
1/17.5	X	X	X	
1/15	X	X	X	
1/12	X	X	X	
1/10		X	X	
1/8		X	X	X
1/7			X	X
1/6			X	X
1/5				X
1/4				X
1/3				

S = Beam Spacing

L = Span Length

TABLE 4 BRIDGES ANALYZED, ROADWAY WIDTH 20 FT.

Roadway Width 30 feet

(2-3 design lanes)

No. Beams	8	7	6	5	4
S/L					
1/30	X				
1/25	X	X			
1/20	X	X	X		
1/17.5	X	X	X		
1/15	X	X	X		
1/12	X	X	X	X	
1/10		X	X	X	
1/8			X	X	X
1/7			X	X	X
1/6				X	X
1/5				X	X
1/4					X
1/3					

S = Beam Spacing

L = Span Length

TABLE 5 BRIDGES ANALYZED, ROADWAY WIDTH 30 FT.

Roadway Width 42 feet

(3-4 design lanes)

No. Beams	10	9	8	7	6	5
S/L						
1/30						
1/25	X					
1/20	X	X	X			
1/17.5	X	X	X			
1/15	X	X	X	X		
1/12	X	X	X	X	X	
1/10	X	X	X	X	X	
1/8		X	X	X	X	X
1/7			X	X	X	X
1/6				X	X	X
1/5					X	X
1/4						X
1/3						

S = Beam Spacing

L = Span Length

TABLE 6 BRIDGES ANALYZED, ROADWAY WIDTH 42 FT.

Roadway Width 54 feet

(4-5 design lanes)

No. Beams	13	11	9	8	7	6
S/L						
1/30	X					
1/25	X	X				
1/20	X	X	X			
1/17.5	X	X	X			
1/15	X	X	X	X		
1/12	X	X	X	X	X	
1/10		X	X	X	X	X
1/8	X		X	X	X	X
1/7		X		X	X	X
1/6			X			X
1/5				X	X	
1/4					X	X
1/3						X

S = Beam Spacing

L = Span Length

TABLE 7 BRIDGES ANALYZED, ROADWAY WIDTH 54 FT.

Roadway Width 66 feet

(5-6 design lanes)

No. Beams	16	14	12	10	9	8
S/L						
1/30	X					
1/25	X	X				
1/20	X	X	X			
1/17.5	X	X	X	X		
1/15	X	X	X	X	X	
1/12	X	X	X	X	X	X
1/10		X	X	X	X	X
1/8			X	X	X	X
1/7				X	X	X
1/6			X			
1/5				X	X	X
1/4				X	X	X
1/3						

S = Beam Spacing

L = Span Length

TABLE 8 BRIDGES ANALYZED, ROADWAY WIDTH 66 FT.

Roadway Width 78 feet

(6-7 design lanes)

No. Beams	17	15	13	12	11	10	9
S/L							
1/30	X						
1/25	X						
1/20	X	X	X				
1/17.5	X	X	X	X			
1/15	X	X	X	X	X		
1/12	X	X	X	X	X	X	X
1/10		X	X	X	X	X	X
1/8			X	X	X	X	X
1/7		X			X	X	X
1/6			X	X			X
1/5			X	X	X	X	
1/4					X	X	X
1/3							X

S = Beam Spacing

L = Span Length

TABLE 9 BRIDGES ANALYZED, ROADWAY WIDTH 78 FT.

ROADWAY WIDTH = 42 FT. AASHTO - $\frac{S}{5.5}$ = 1.27

NO. OF BEAMS = 7

	3 LANE RESULTS		4 LANE RESULTS	
LENGTH	MAX D.F.	$\frac{S}{X}$	MAX D.F.	$\frac{S}{X}$
42	1.29	5.43	1.42	4.93
49	1.25	5.59	1.41	4.96
56	1.25	5.59	1.41	4.96
70	1.24	5.65	1.41	4.96
84	1.22	5.74	1.40	5.00
105	1.16	6.03	1.38	5.07

TABLE 10 DISTRIBUTION FACTORS 42 FT. WIDE, 7 BEAM BRIDGES

9. FIGURES

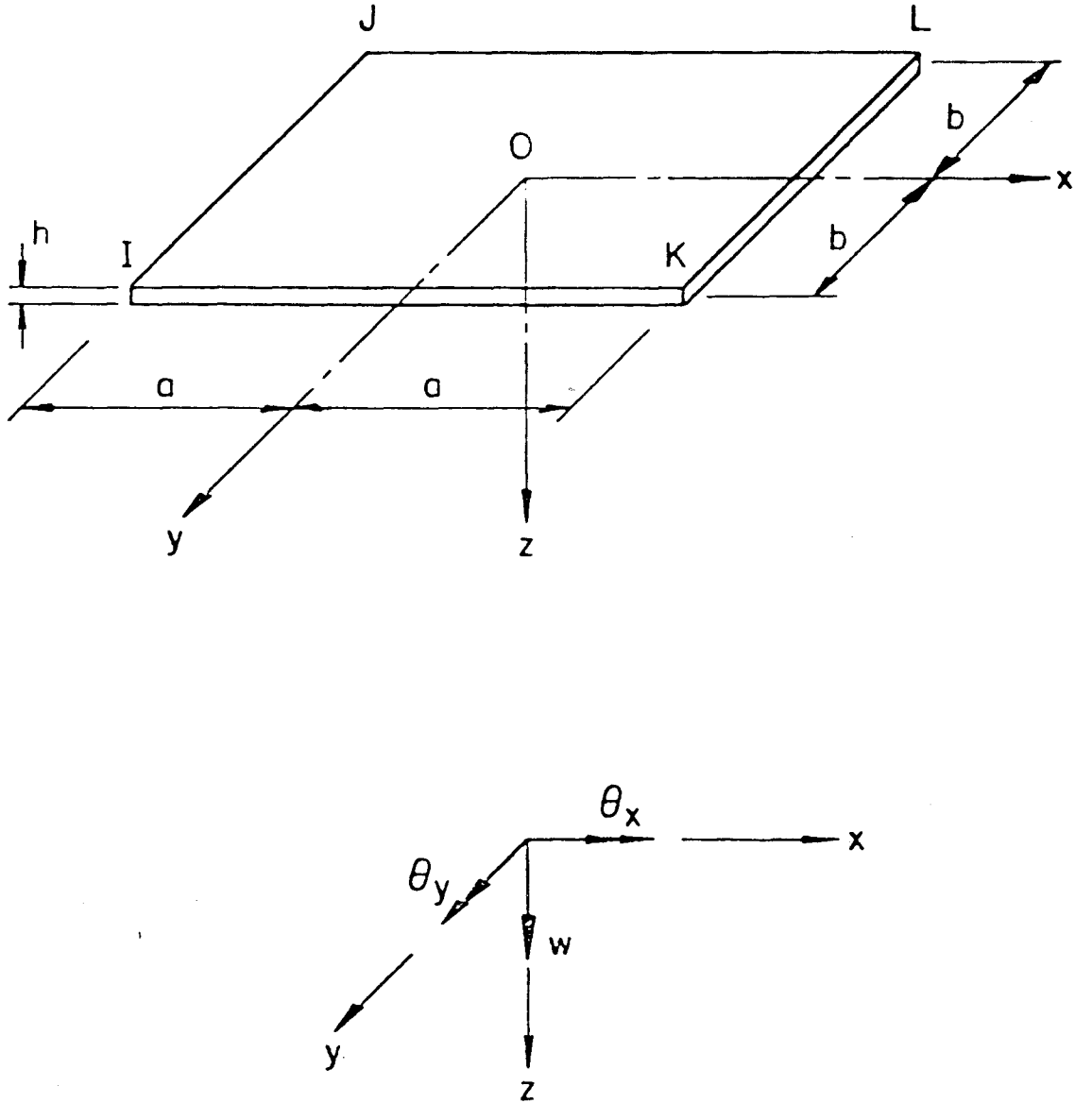

Fig. 1 Rectangular Plate Element and Basic Displacement Components

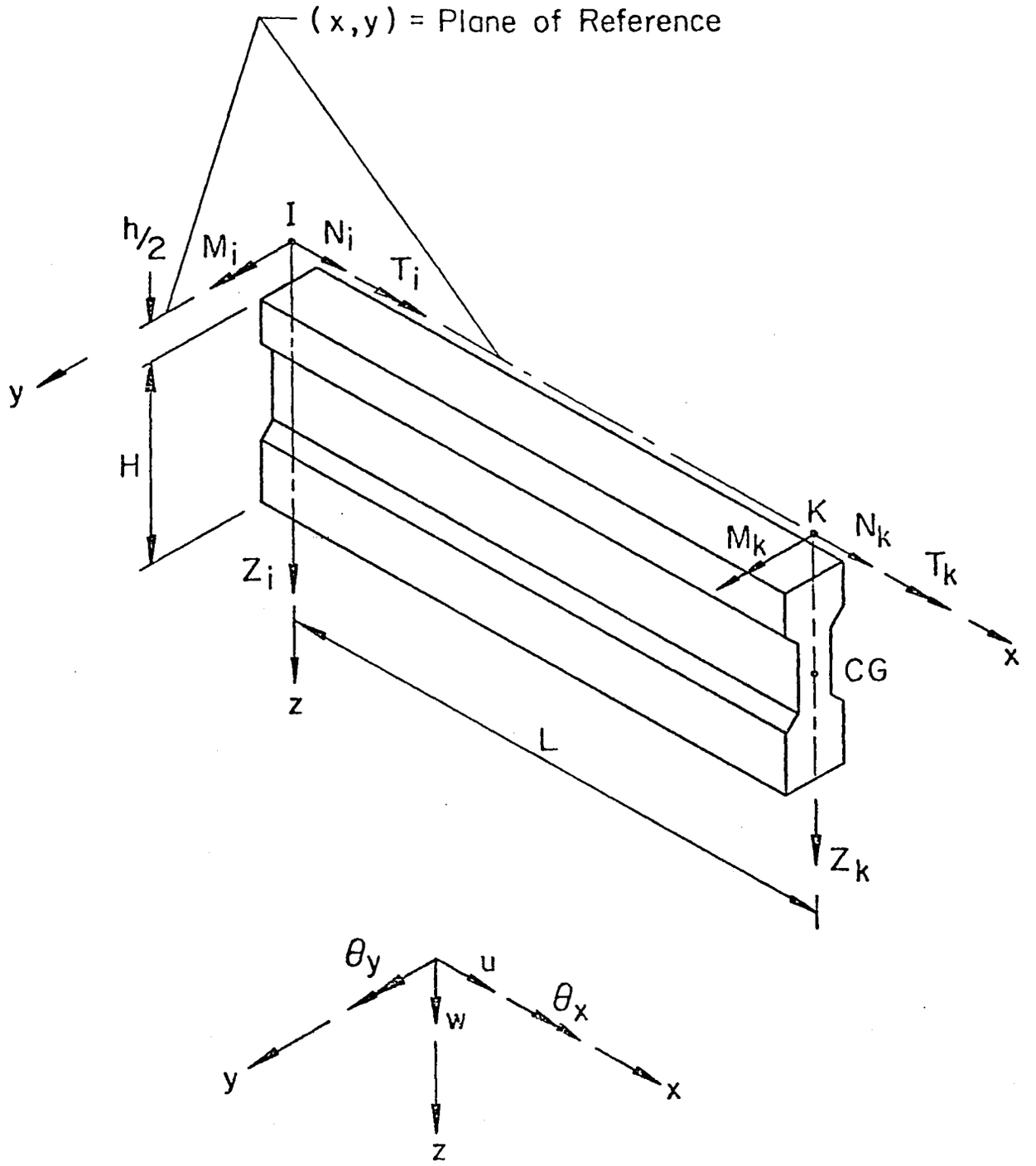

Fig. 2 Eccentrically Attached Beam Element

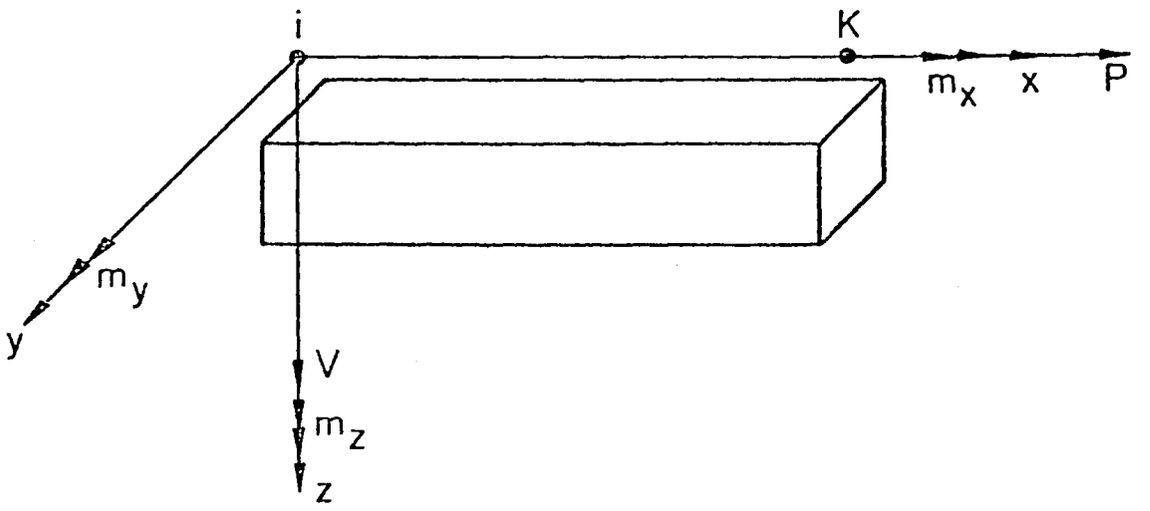

Fig. 3 Coordinate System and Positive Sign Convention

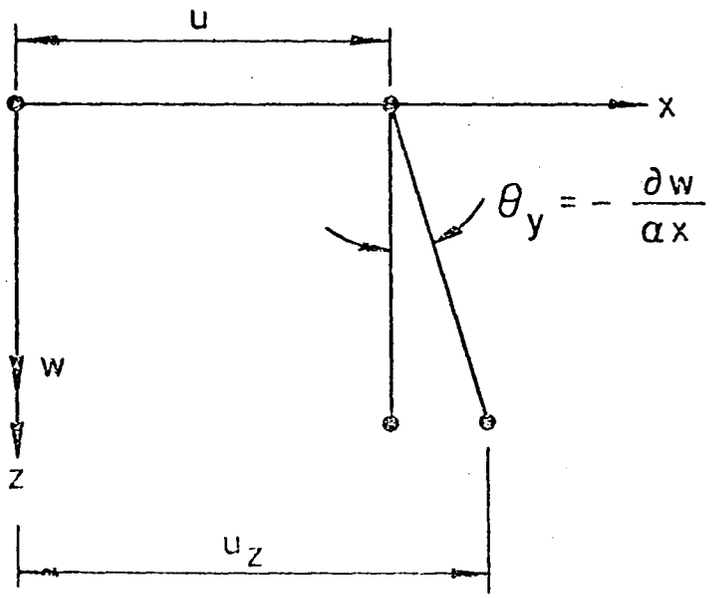

Fig. 3 Coordinate System and Generalized Displacements

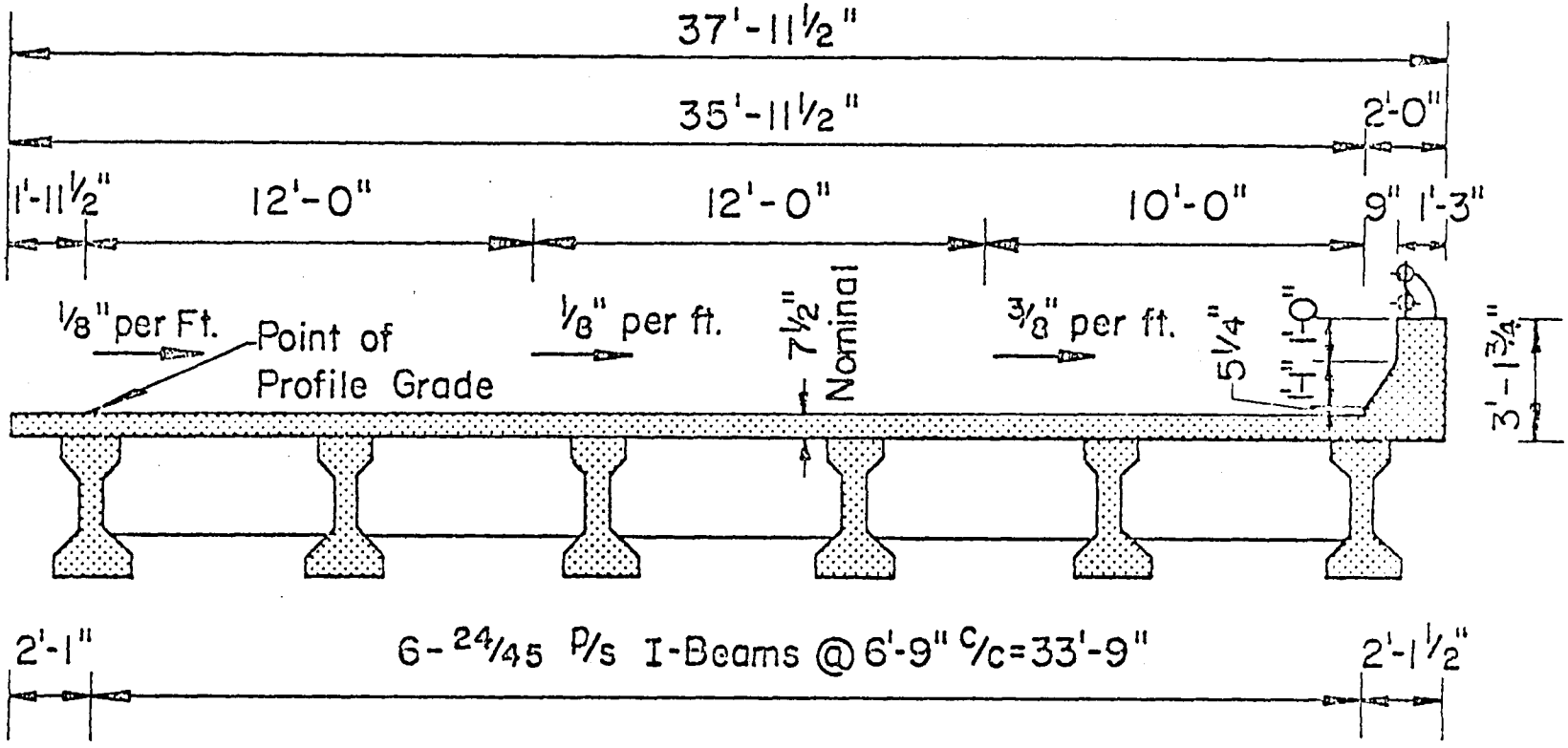

Fig. 4 Cross-Section of Lehighton Bridge

DESIGN DIMENSIONS

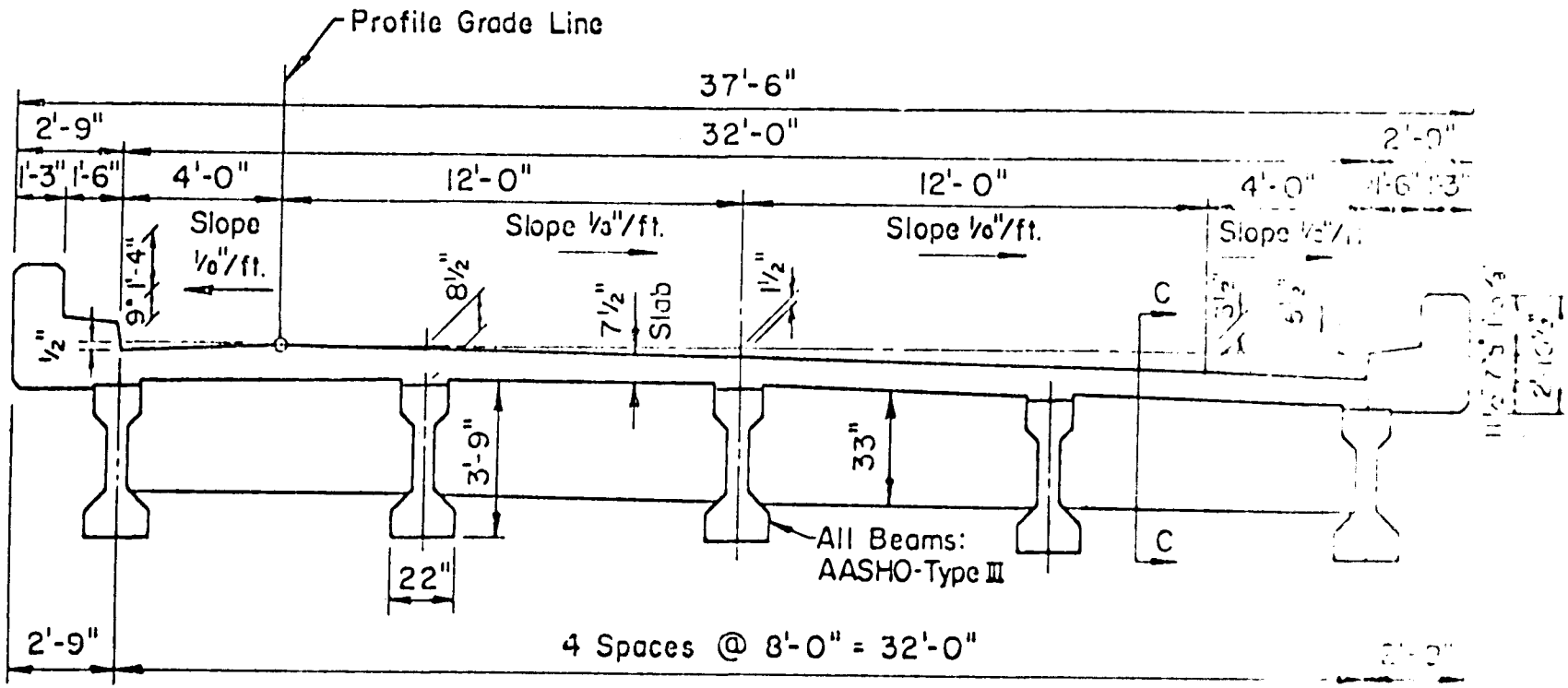

Fig. 5 Cross-Section of Bartonsville Bridge

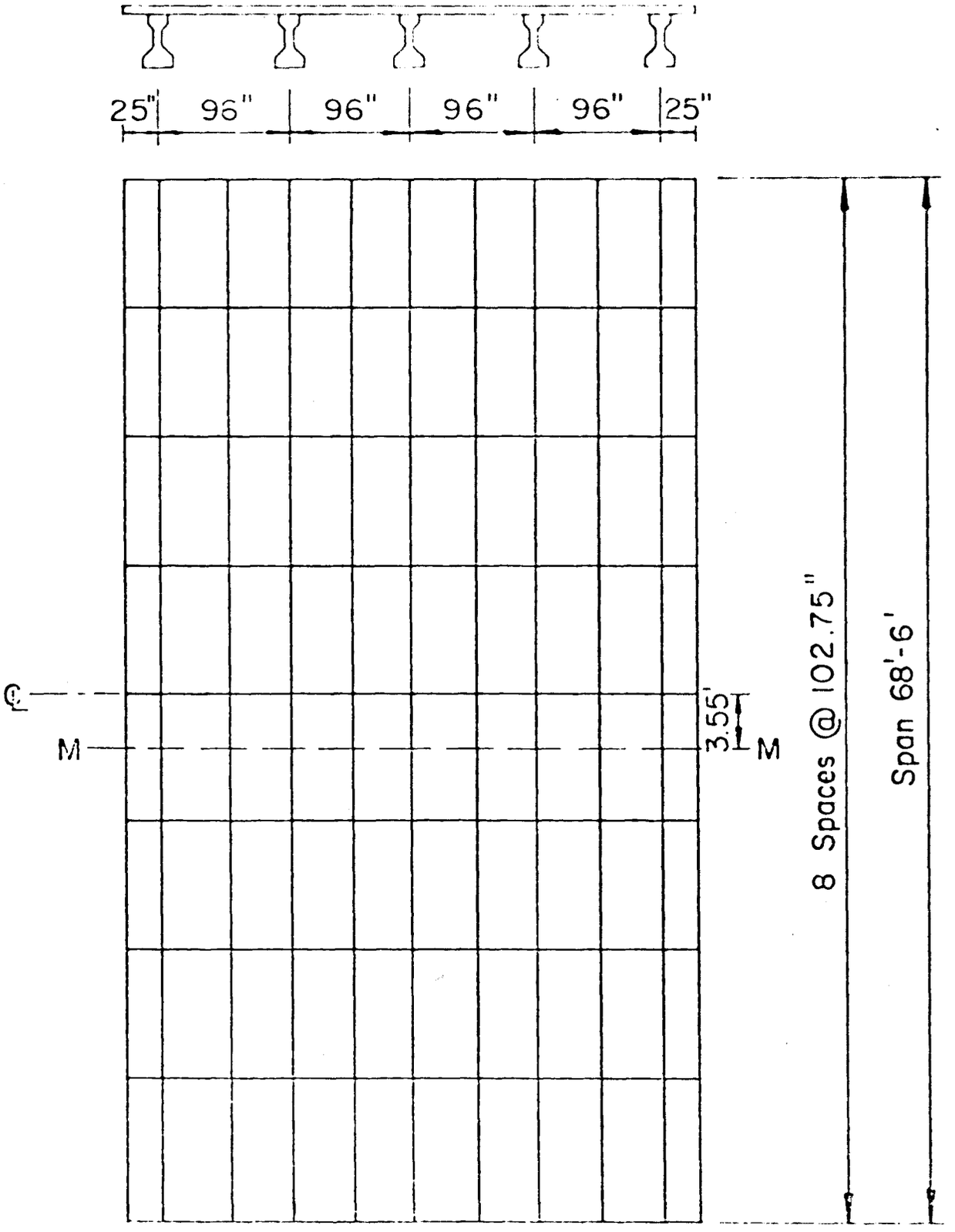

Fig. 6 Discretization of I-Beam Bridge

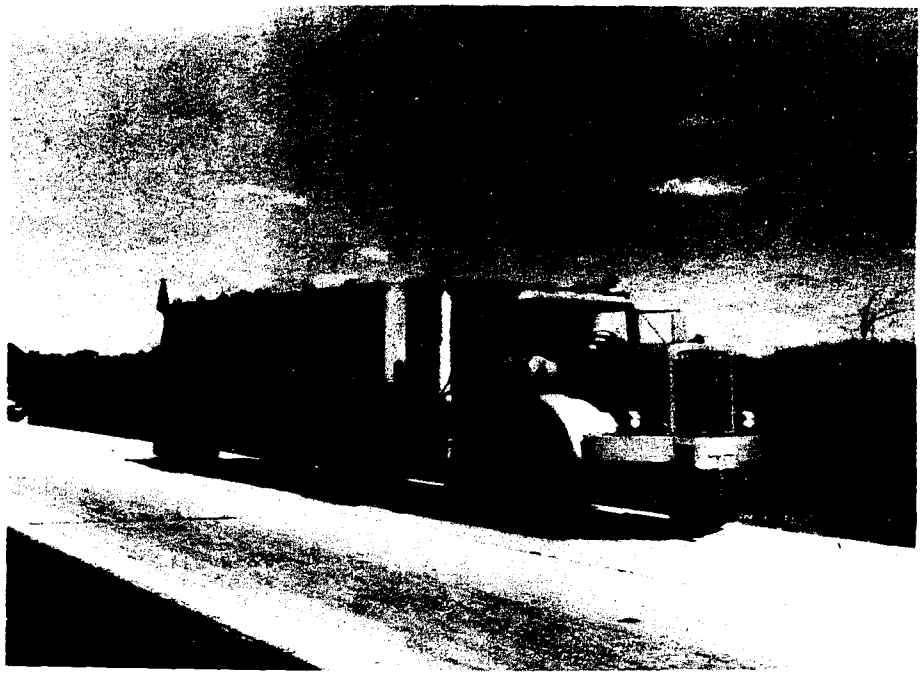

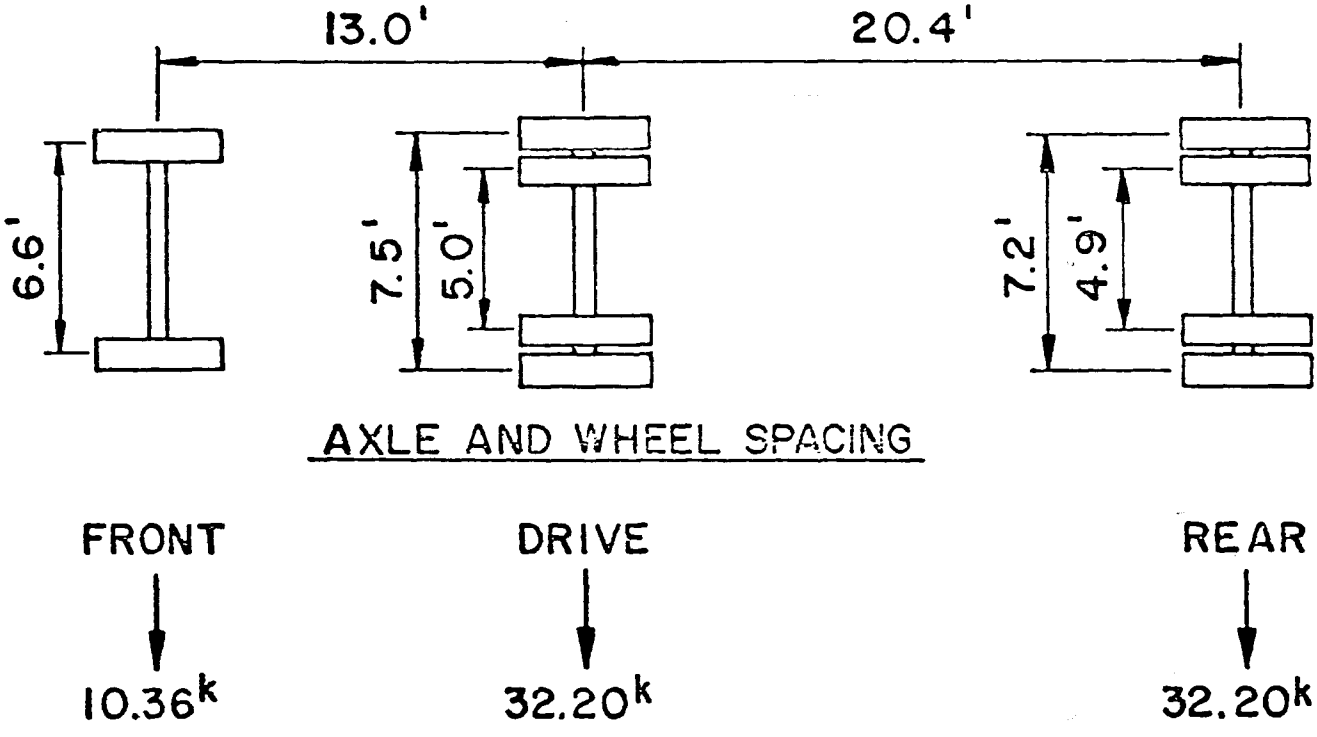

Fig. 7 Test Vehicle

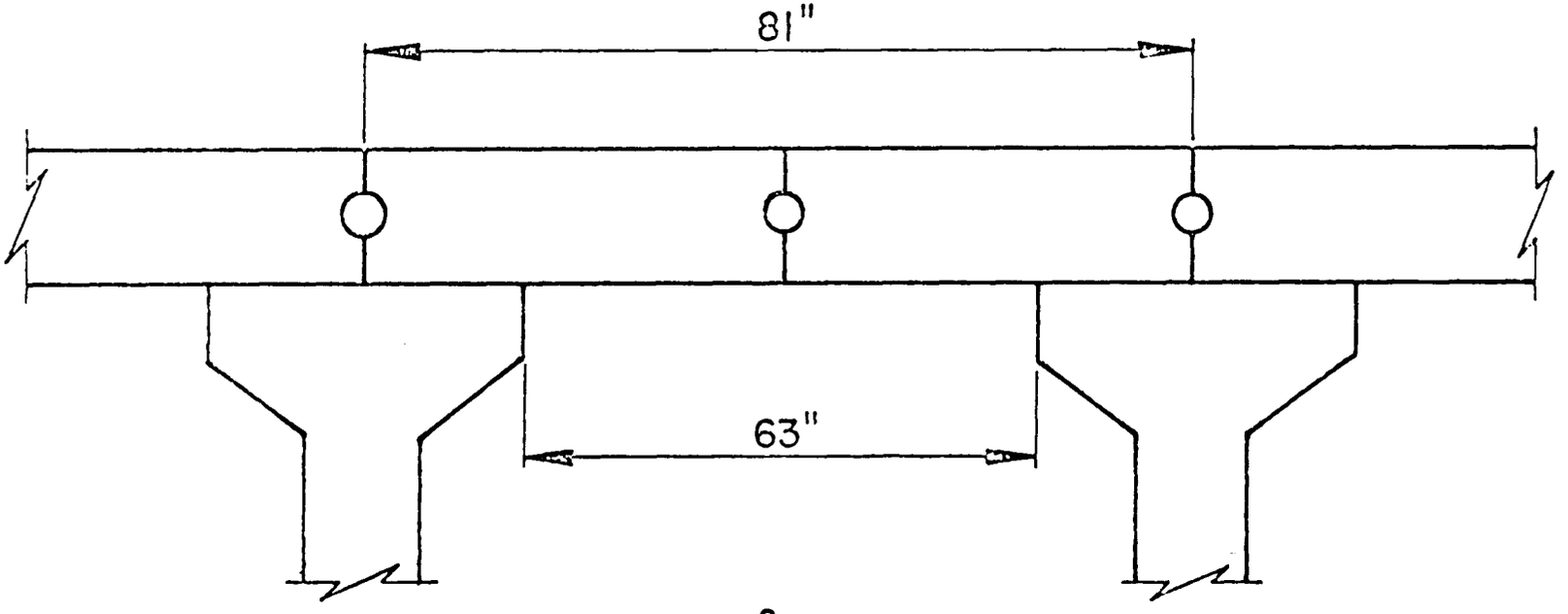

$$D_Y = \left(\frac{81}{63}\right)^2 = 1.69$$

Fig. 8 2PL Mesh Discretization and Orthotropy Factor

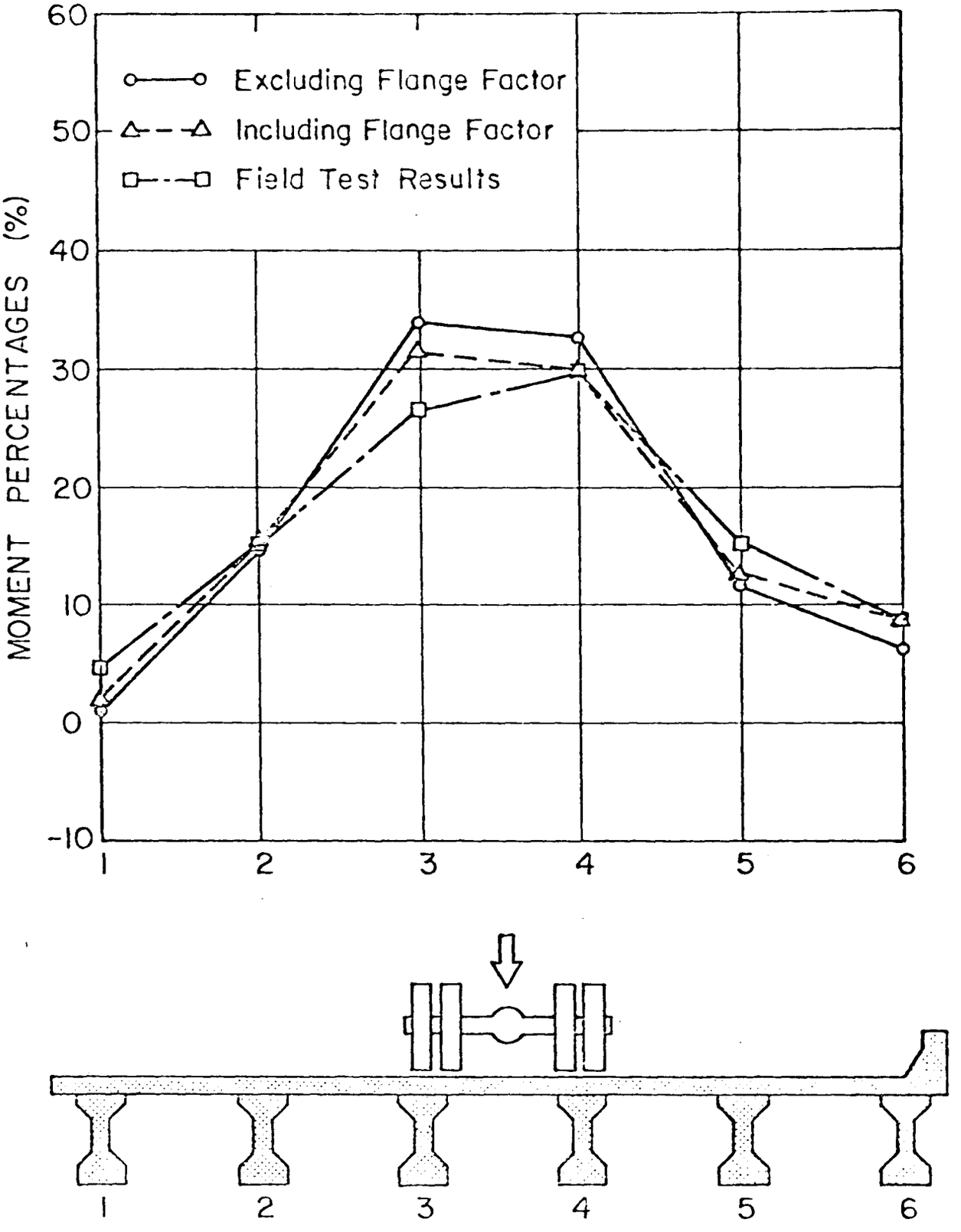

Fig. 9 Moment Percentages

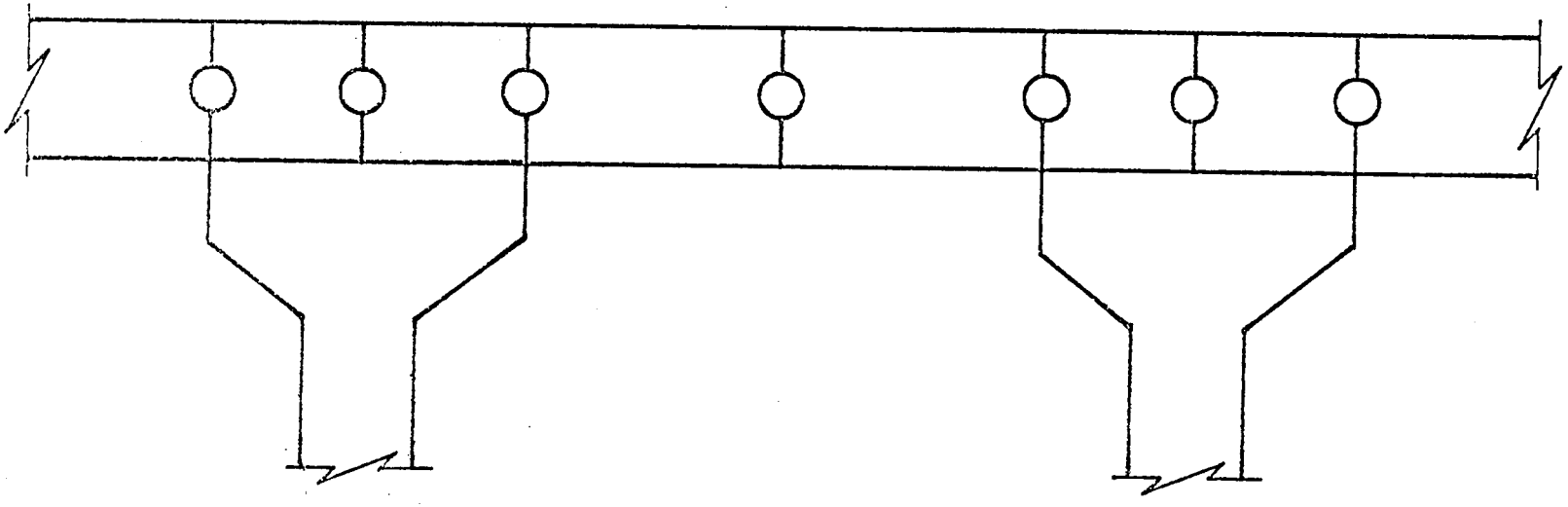

Slab Elements Over Flanges $D_Y = 100.0$

Slab Elements Between Beams $D_Y = 1.0$

Fig. 10 4PL Mesh Discretization and Orthotropy Factors

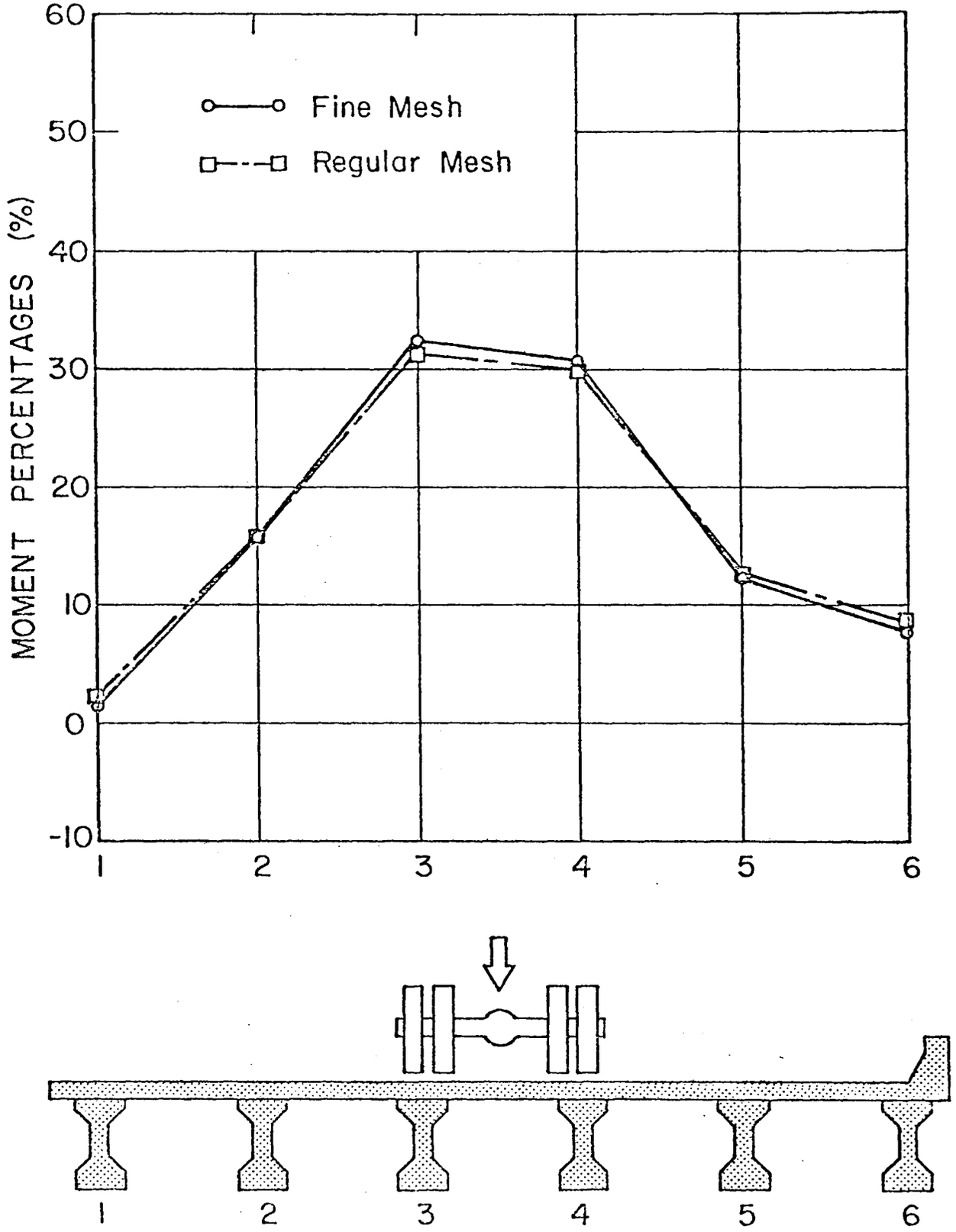

Fig. 11 Moment Percentages (2 PL Mesh - Regular Mesh, 4 PL Mesh - Fine Mesh)

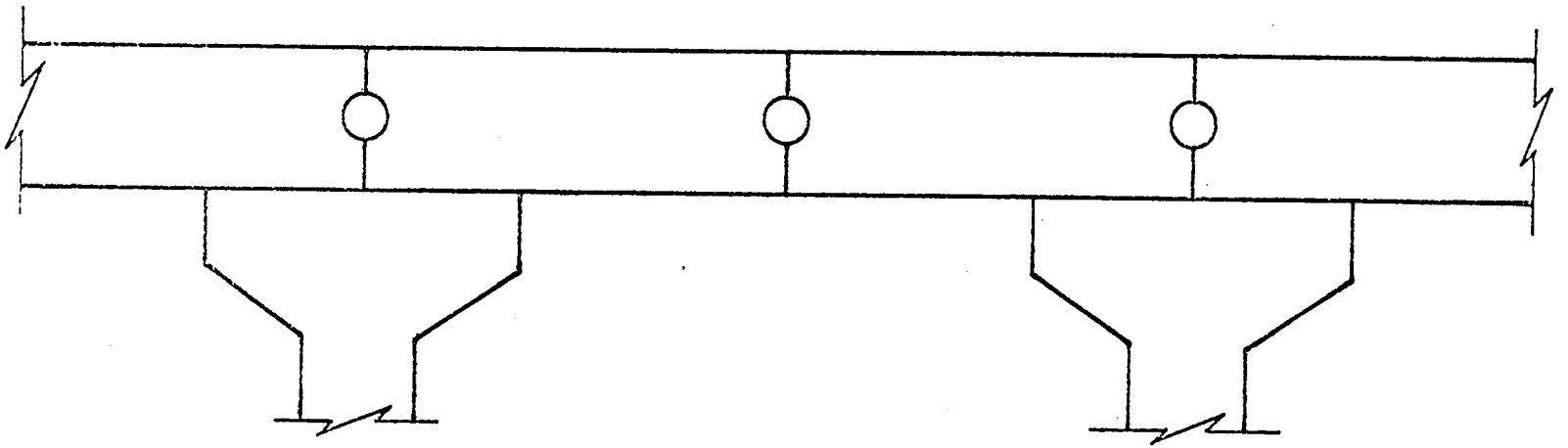

a) Two Slab Elements Between Beams

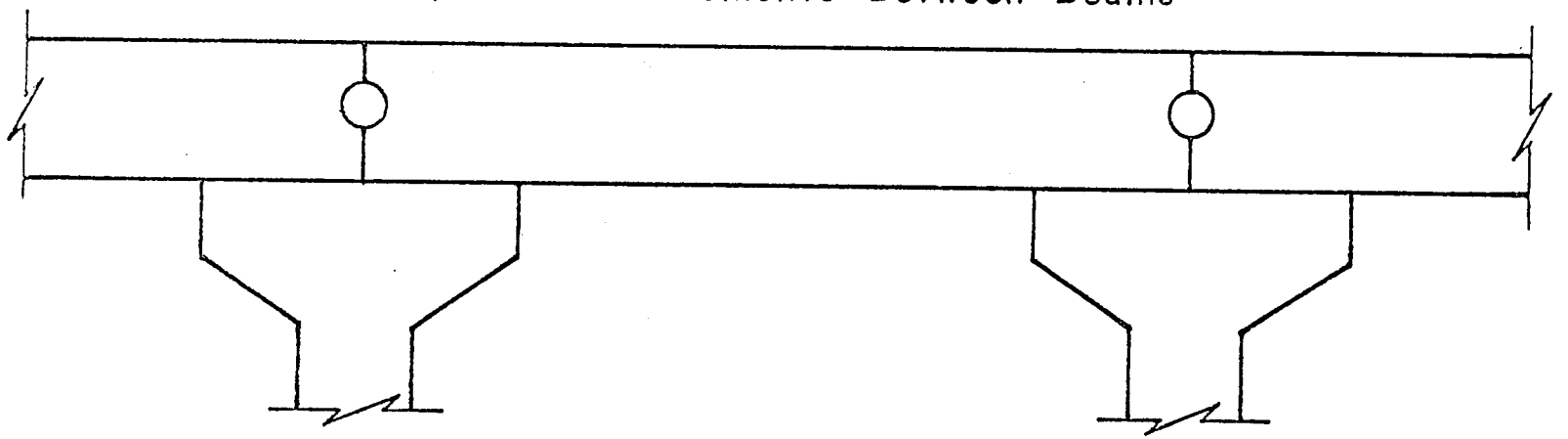

b) One Slab Elements Between Beams

Fig. 12 2 PL and 1 PL Mesh Discretization

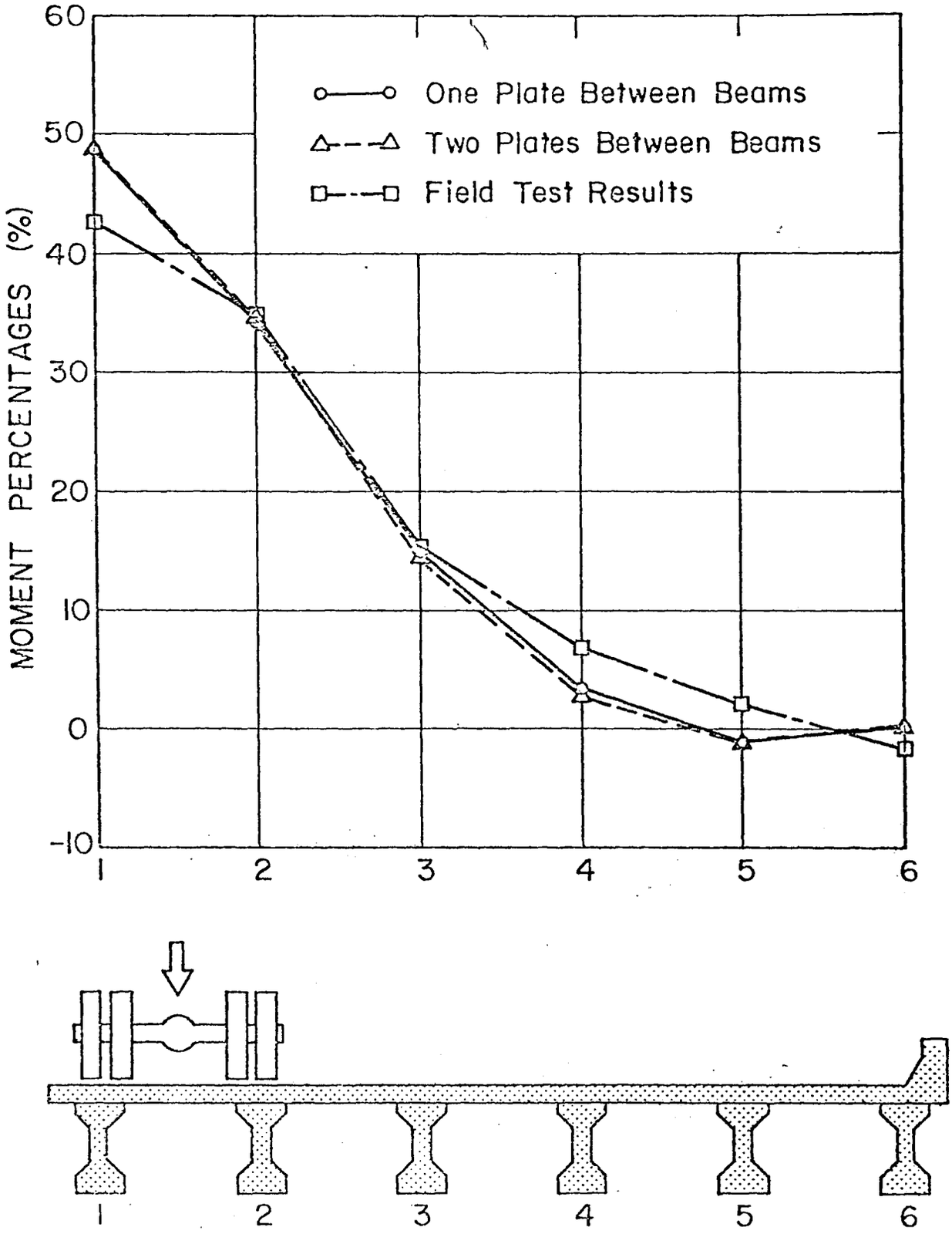

Fig. 13 Moment Percentages

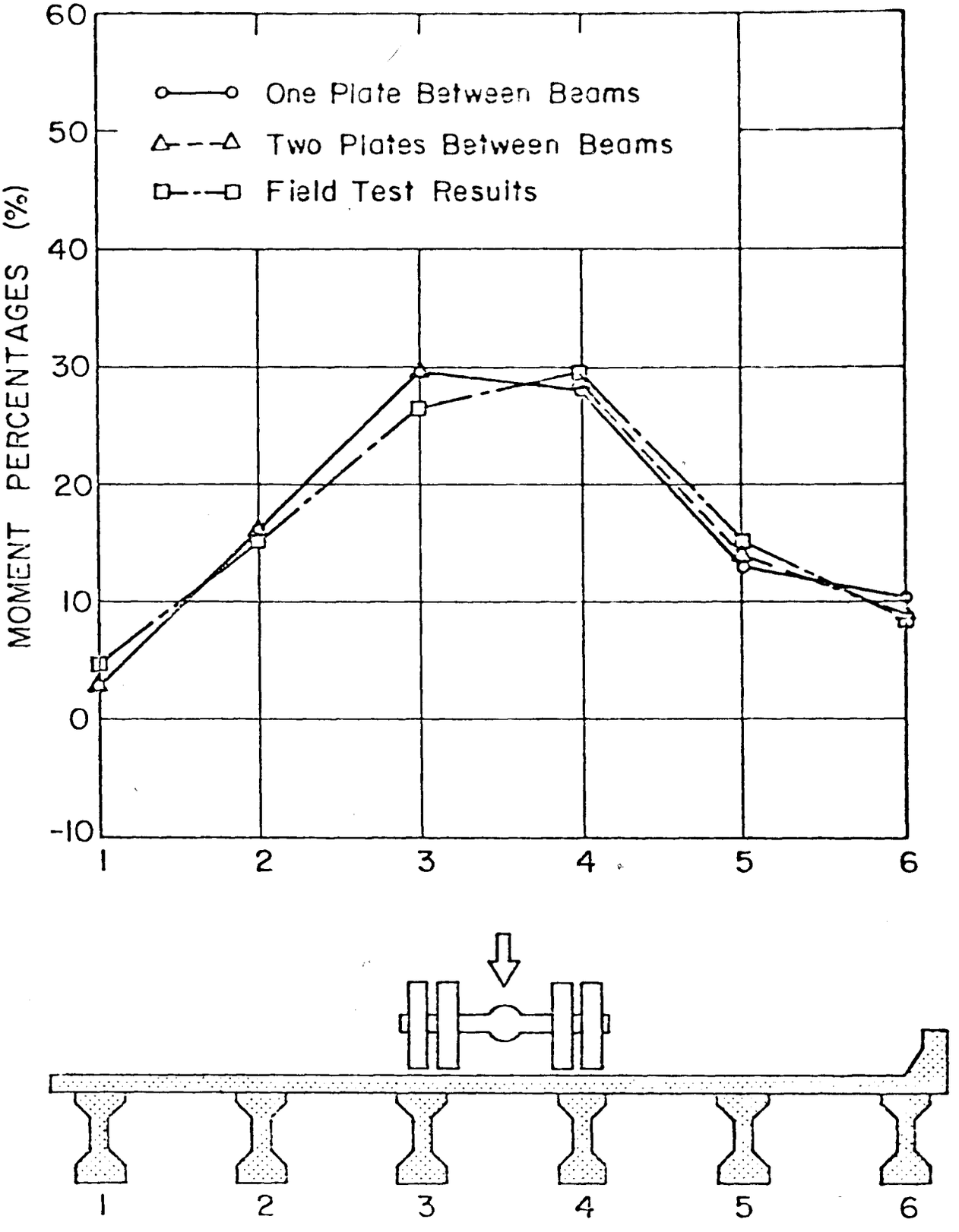

Fig. 14 Moment Percentages

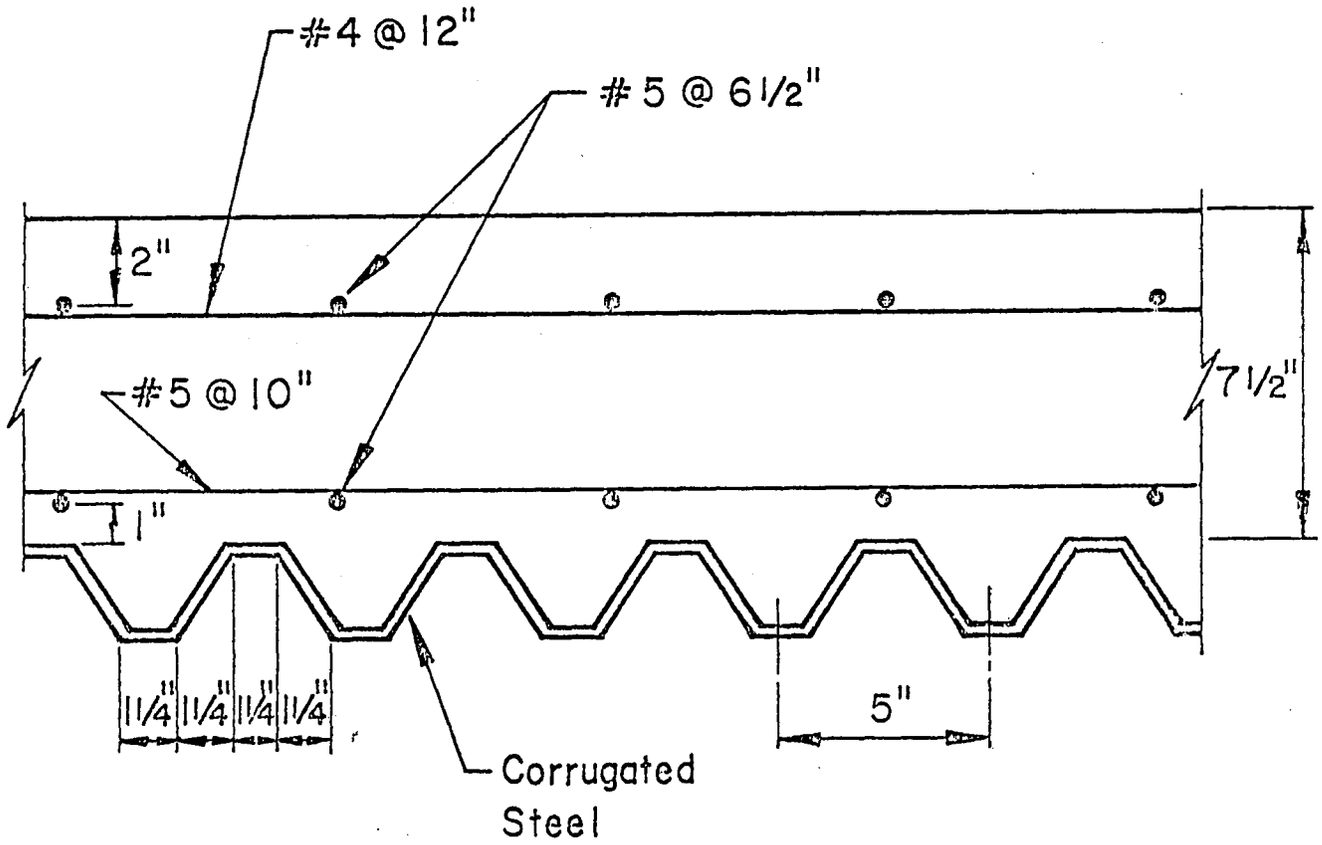

Transverse Cross-section Of Slab

Fig. 15 Cross-Section of Lehighton Bridge Slab

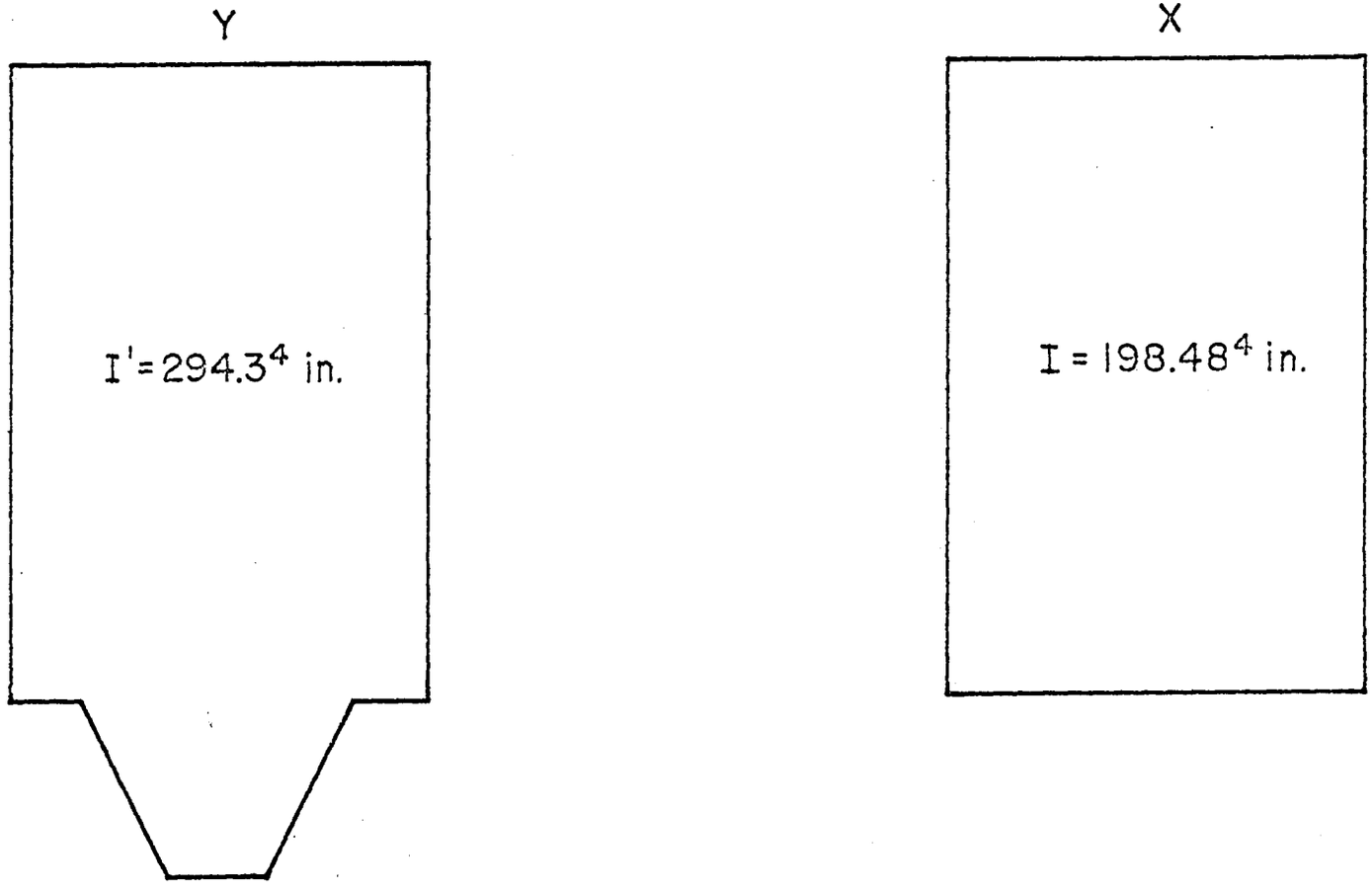

$$D_Y = \frac{I'}{I} = 1.48$$

Fig. 16 Slab Moments of Inertia and Orthotropy factor

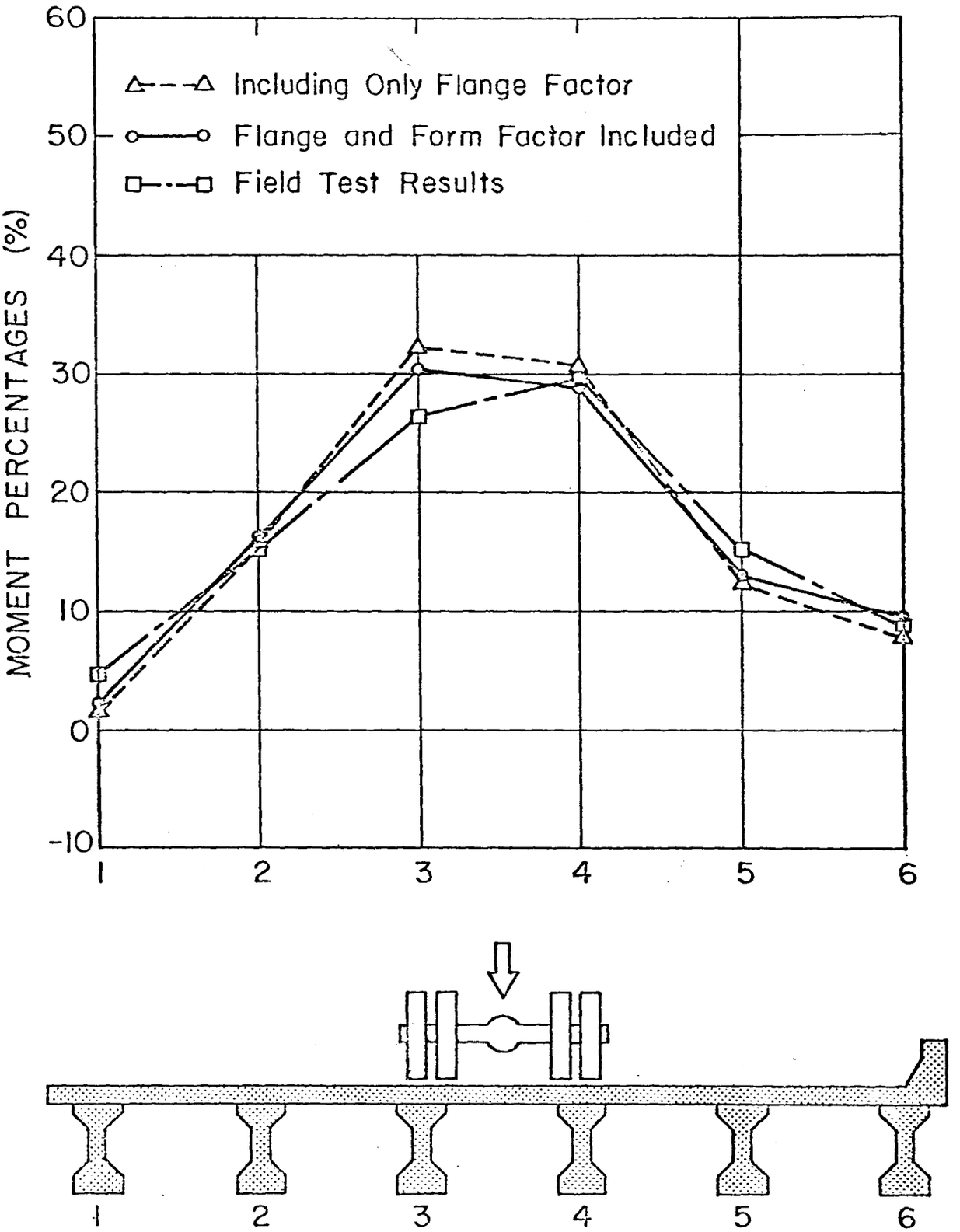

Fig. 17 Moment Percentages

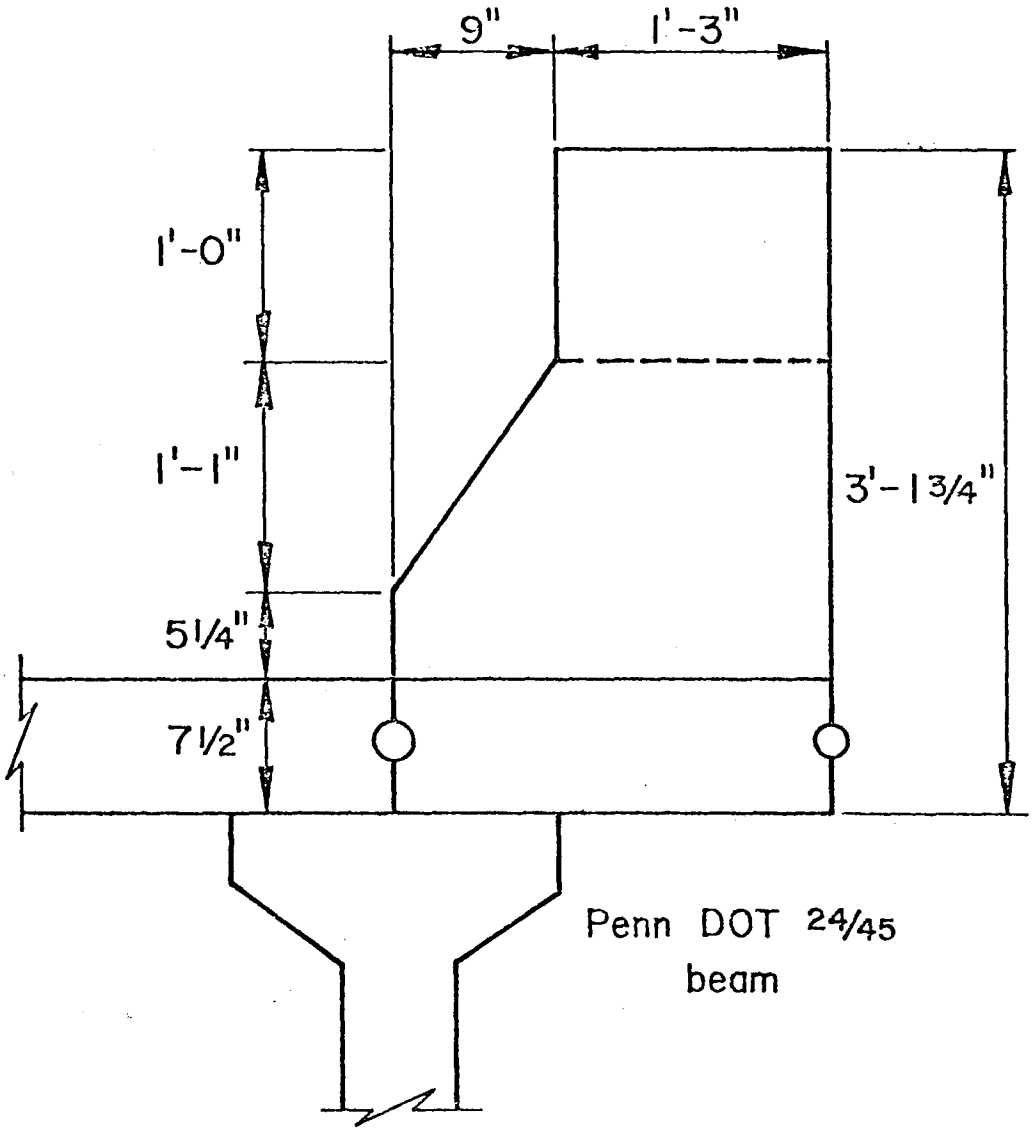

Fig. 18 Curb-Parapet Section

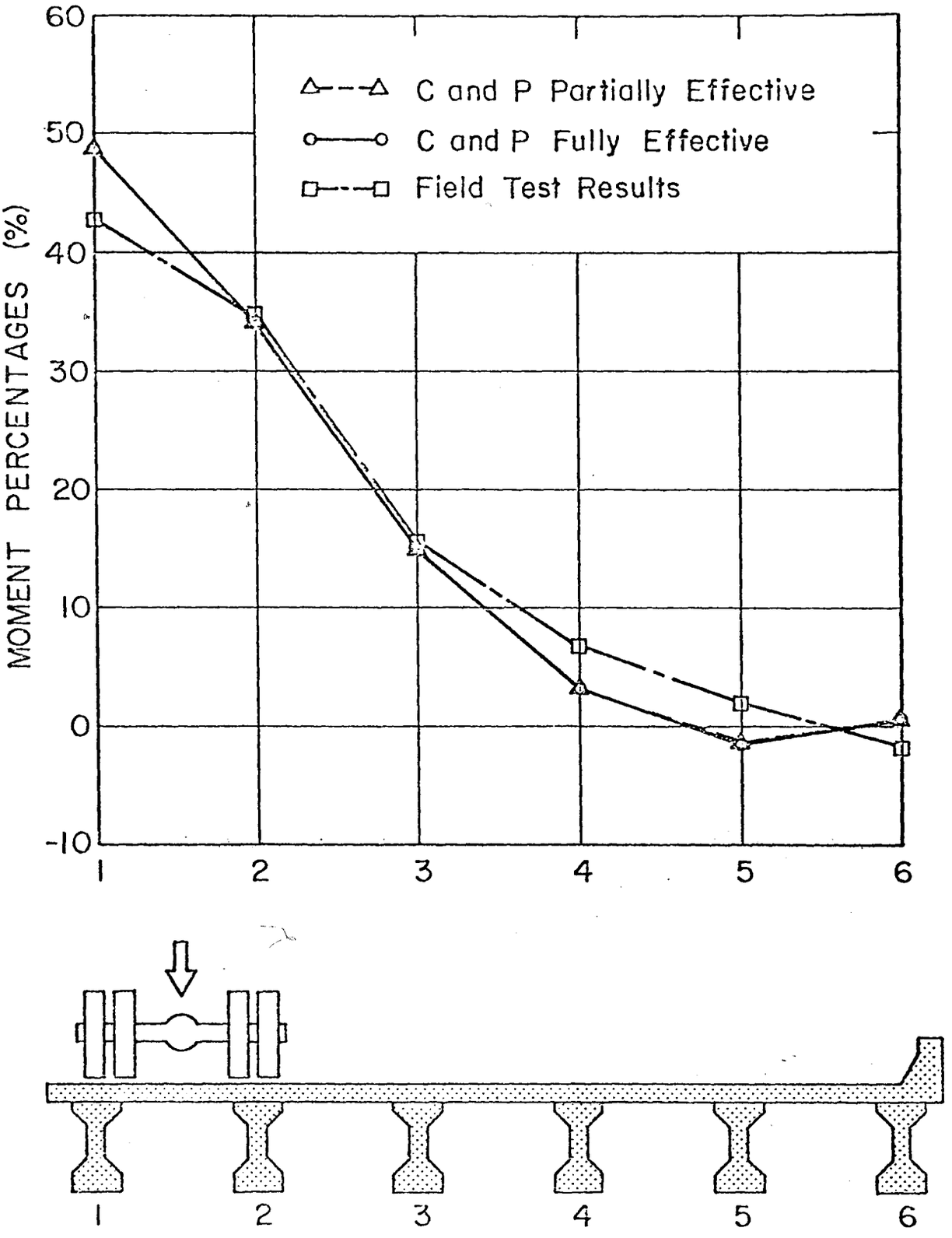

Fig. 19 Moment Percentages

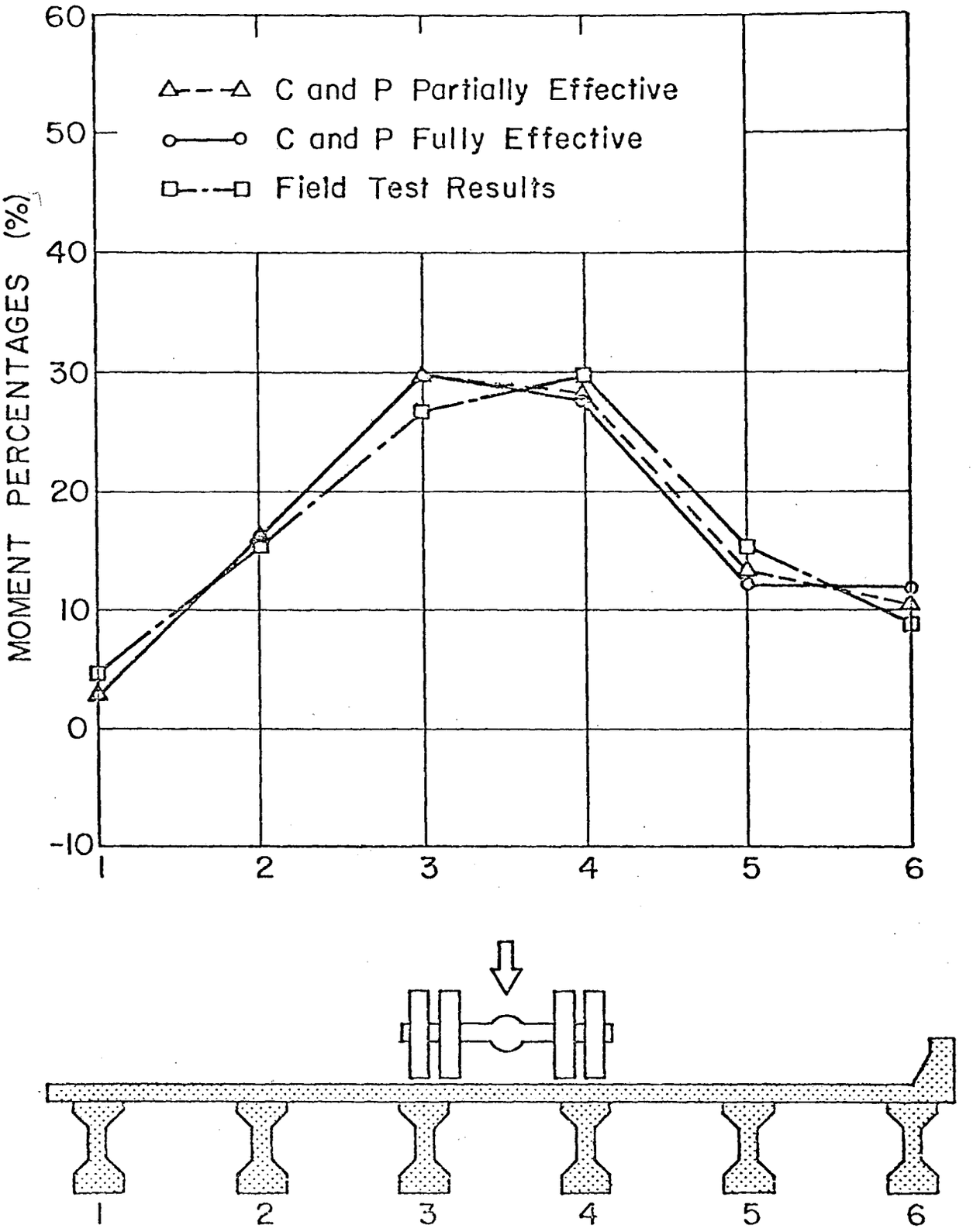

Fig. 20 Moment Percentages

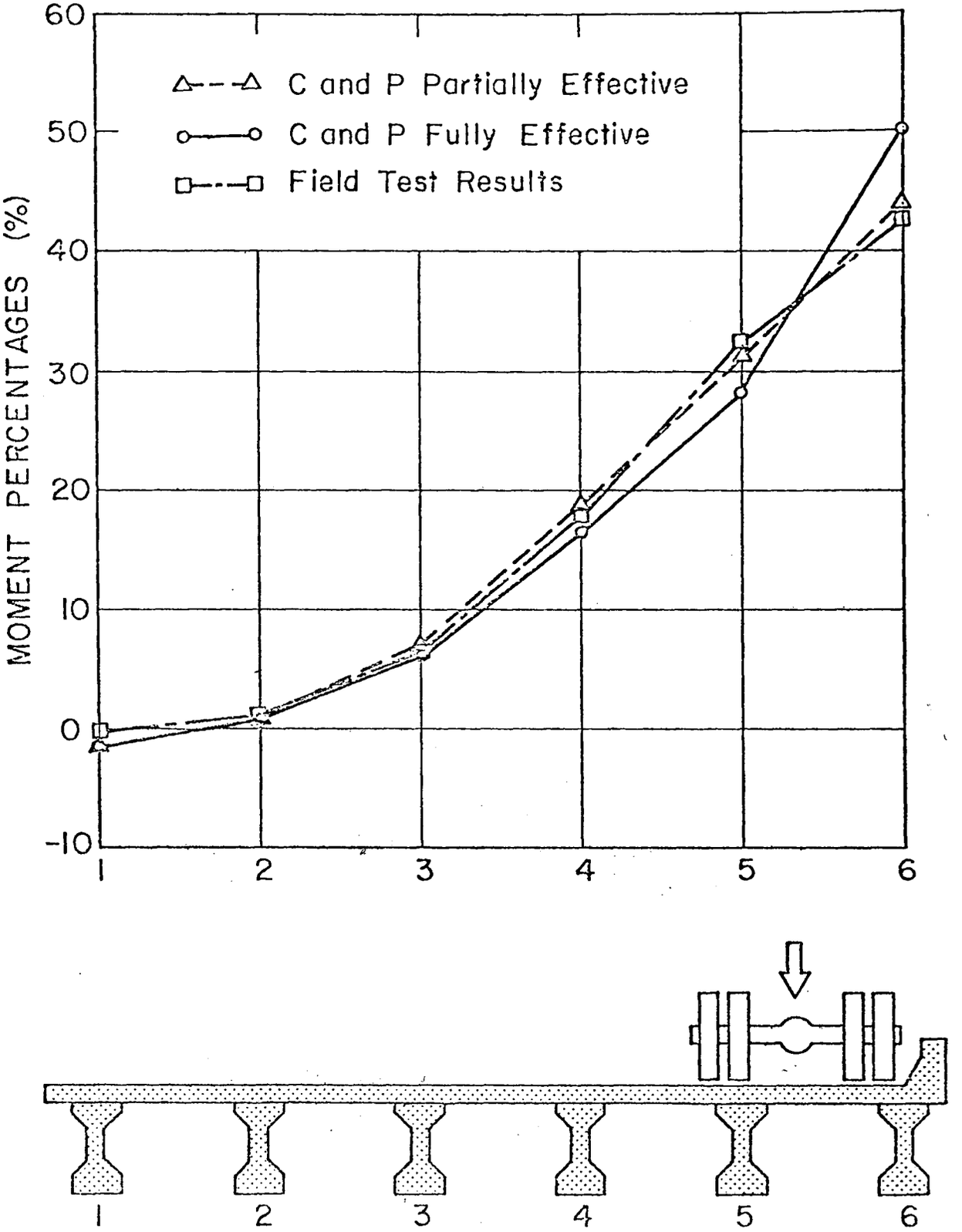

Fig. 21 Moment Percentages

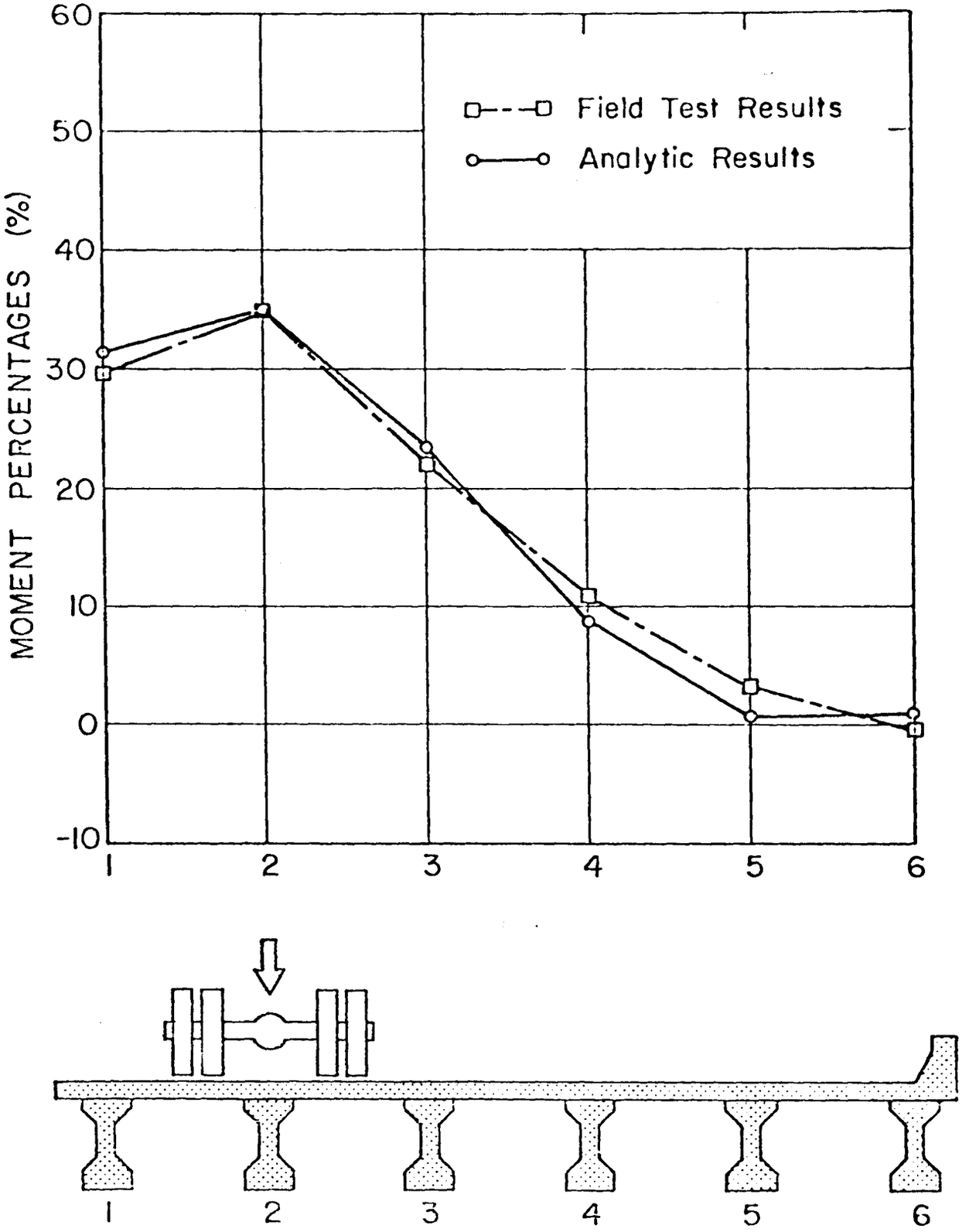

Fig. 22 Moment Percentages - Lehighton Bridge

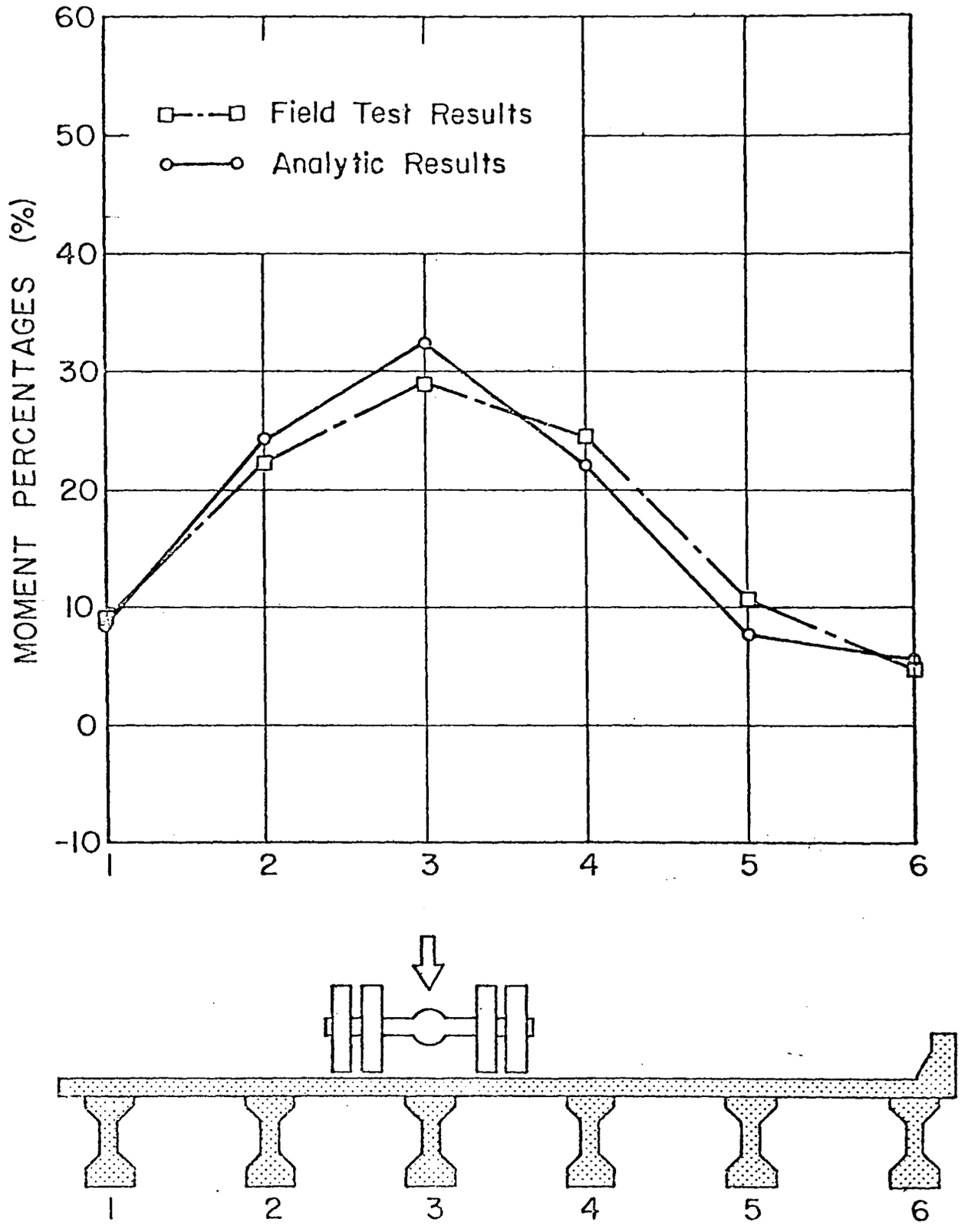

Fig. 23 Moment Percentages - Lehighton Bridge

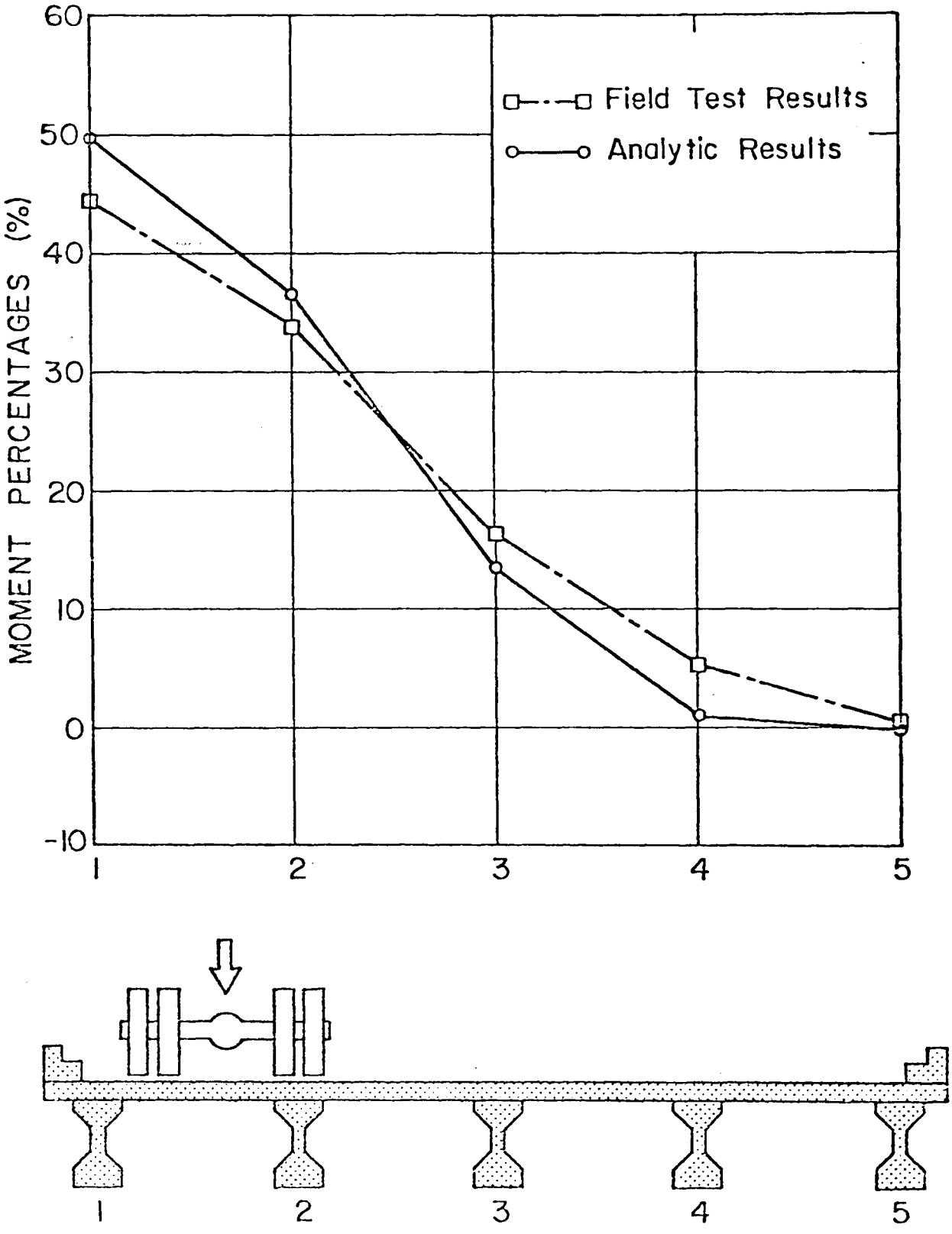

Fig. 24 Moment Percentages - Bartonsville Bridge

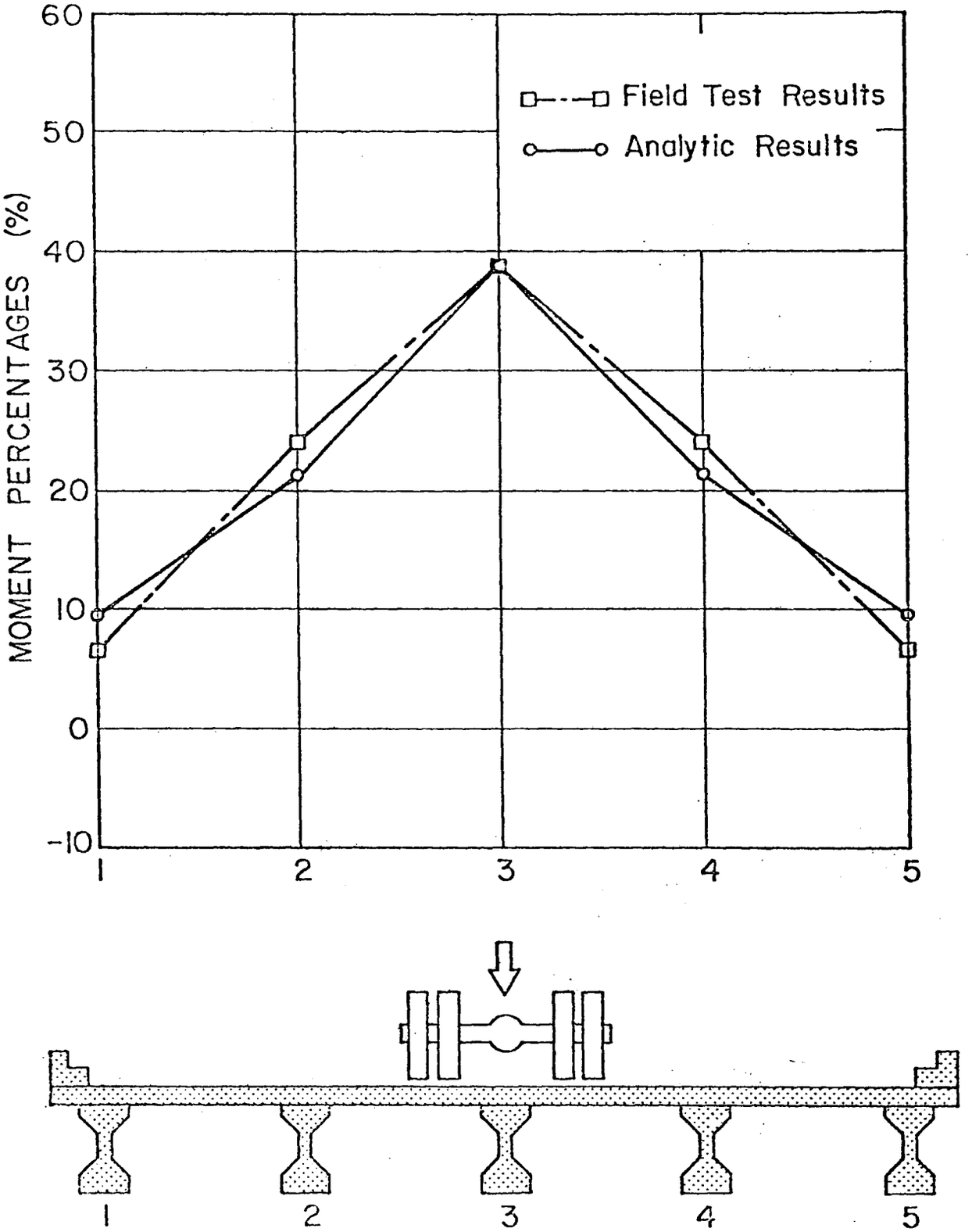

Fig. 25 Moment Percentages - Bartonsville Bridge

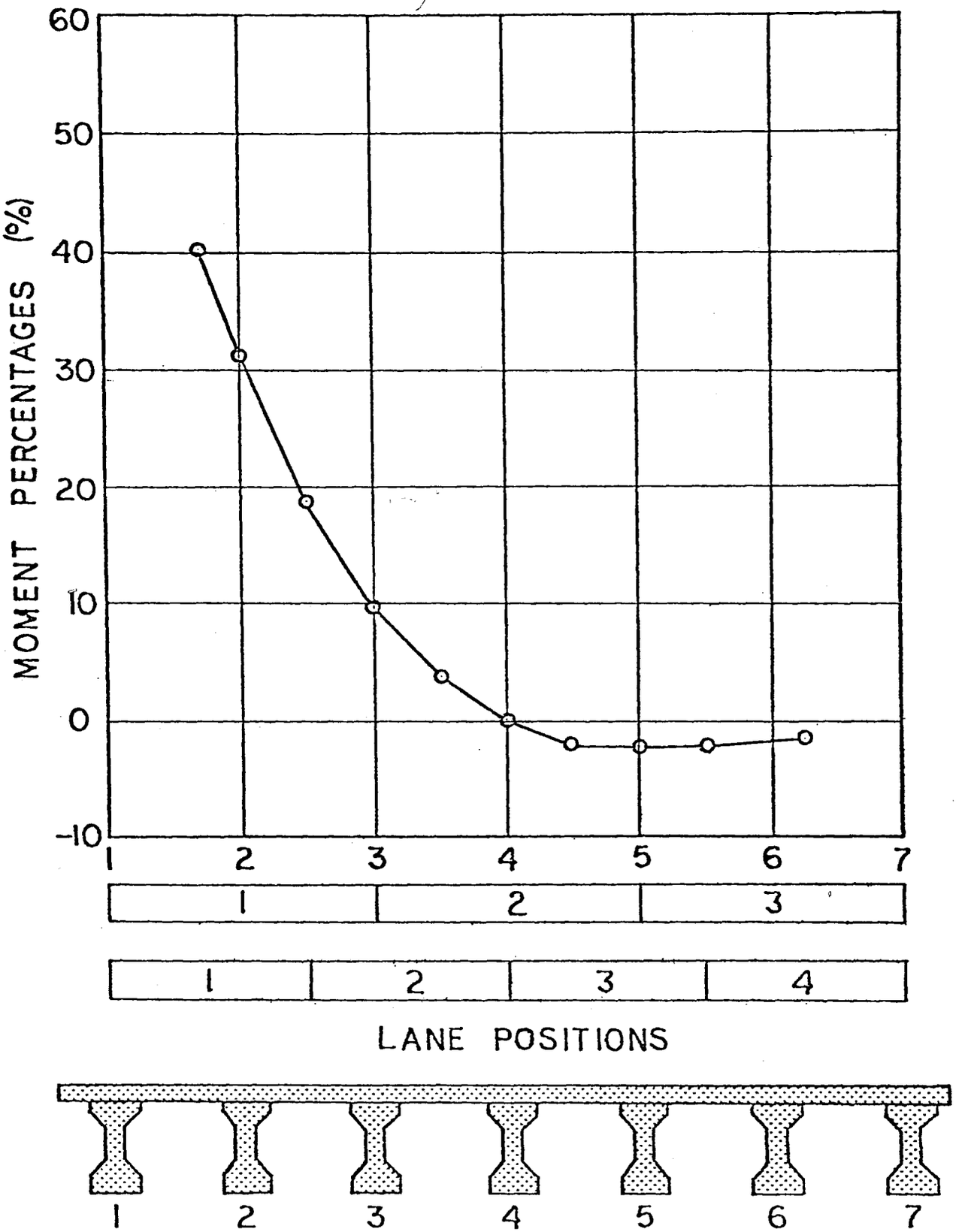

Fig. 26 Influence Line for Moment Percentages
42 Ft. Wide Bridge, 7 Beams, Length 105 Ft. - Beam 1

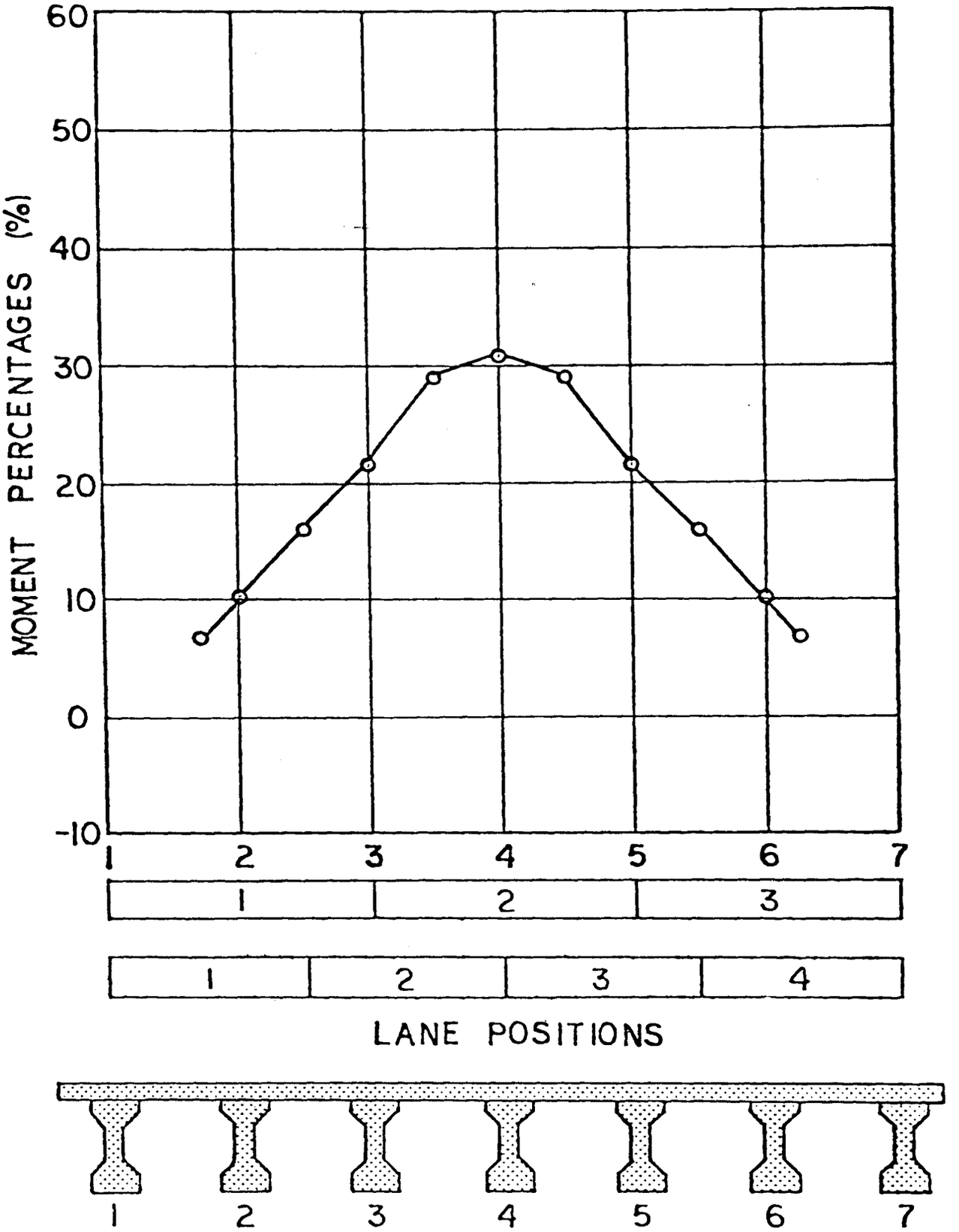

Fig. 27 Influence Line for Moment Percentages
42 Ft. Wide Bridge, 7 Beams, Length 105 Ft. - Beam 4

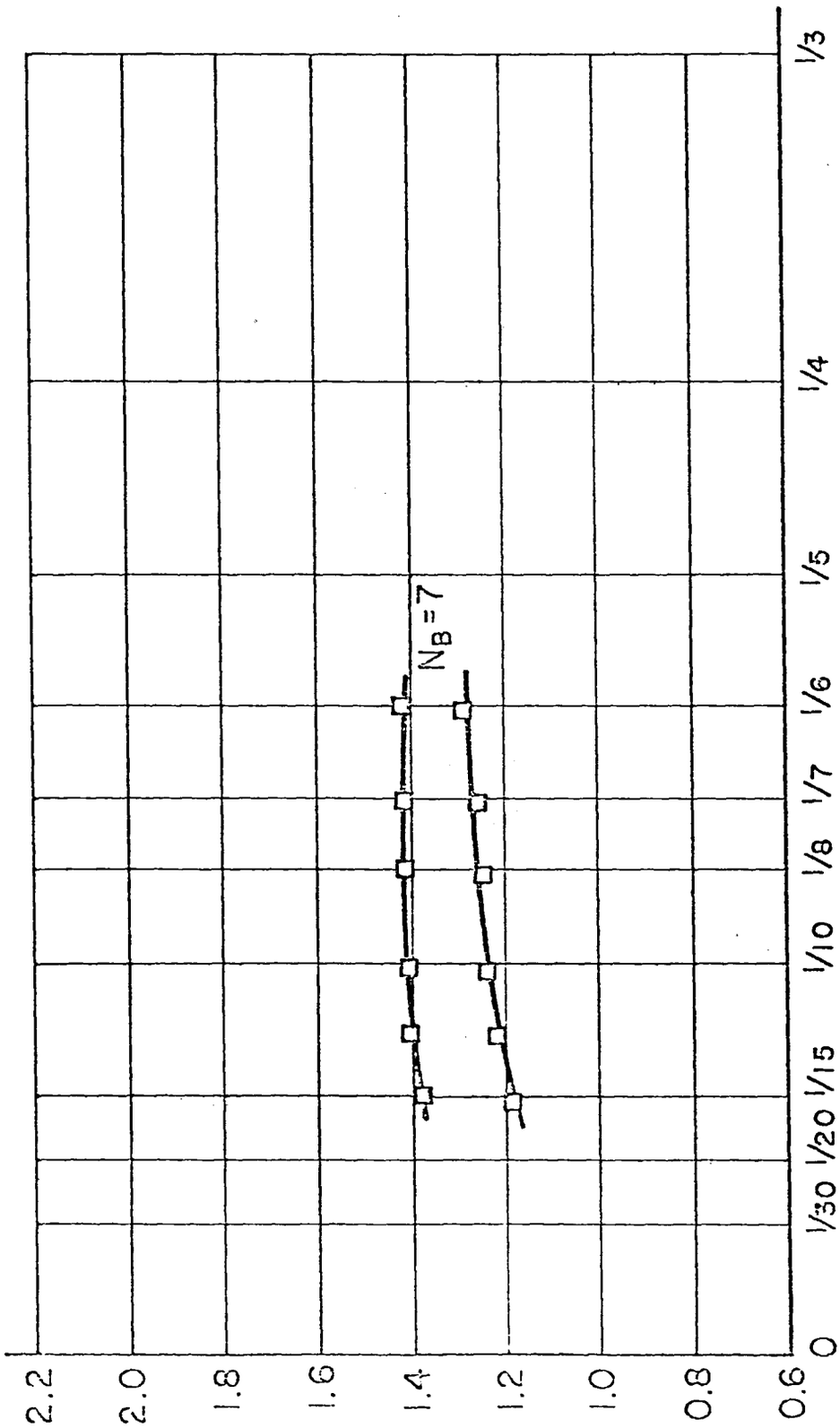

Fig. 28 Distribution Factors for Interior Beam 42ft. Wide, 7 Beam Bridges

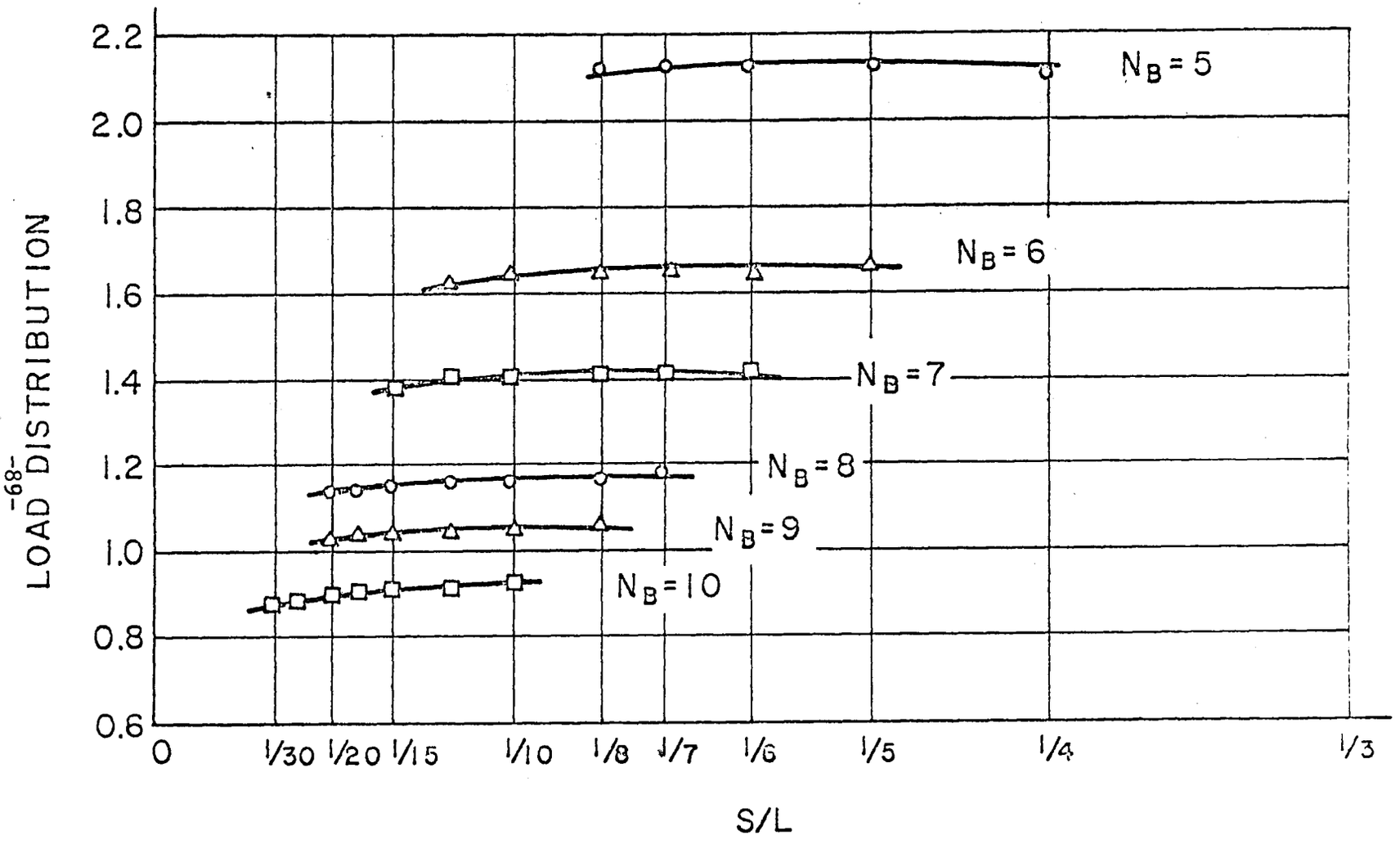

Fig. 29 Distribution Factors for Interior Beam 42 Ft. Wide Bridges ($N_L = 4$)

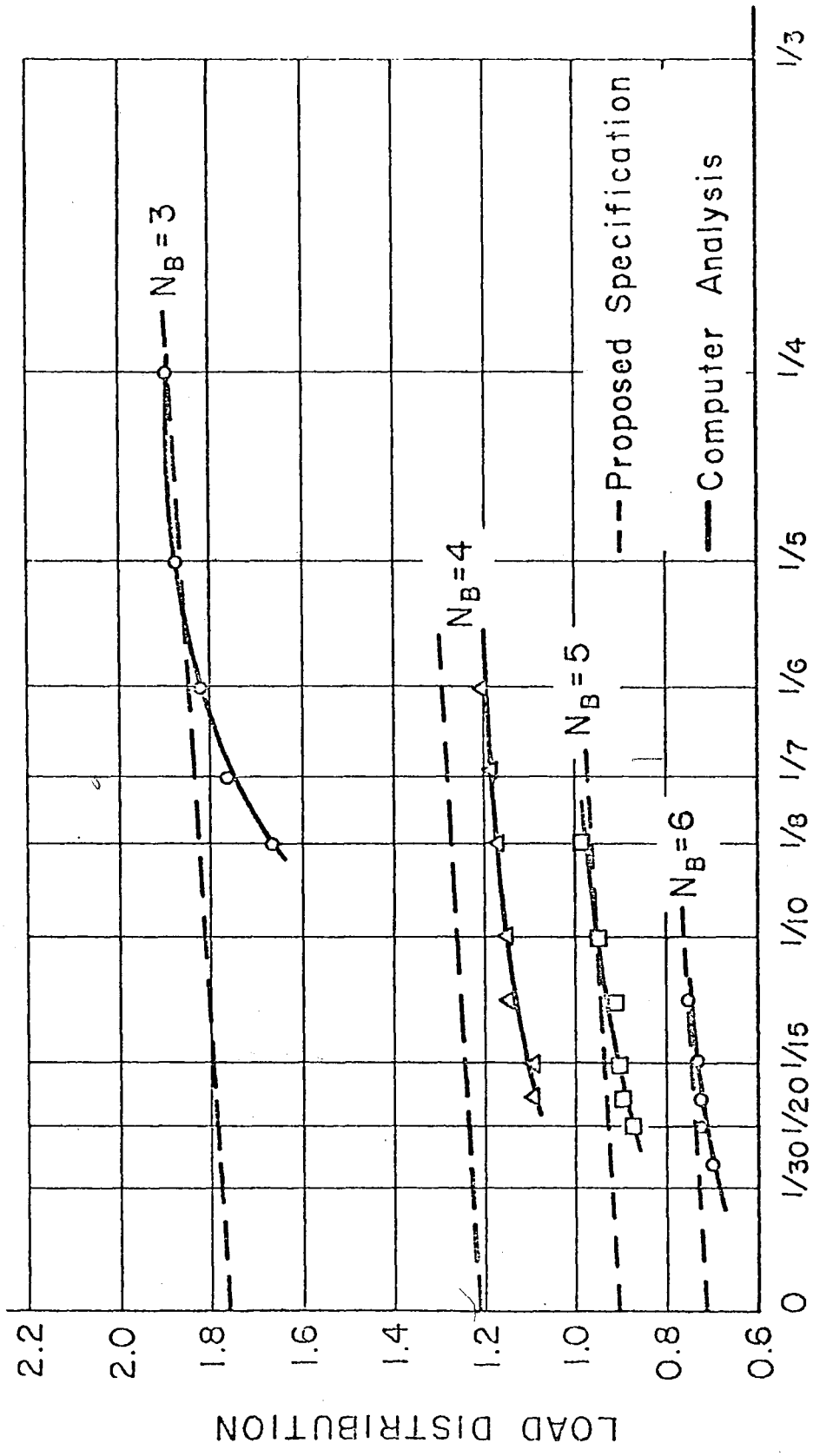

Fig. 30 Distribution Factors for Interior Beam 20 Ft. Wide Bridges ($N_L = 2$)

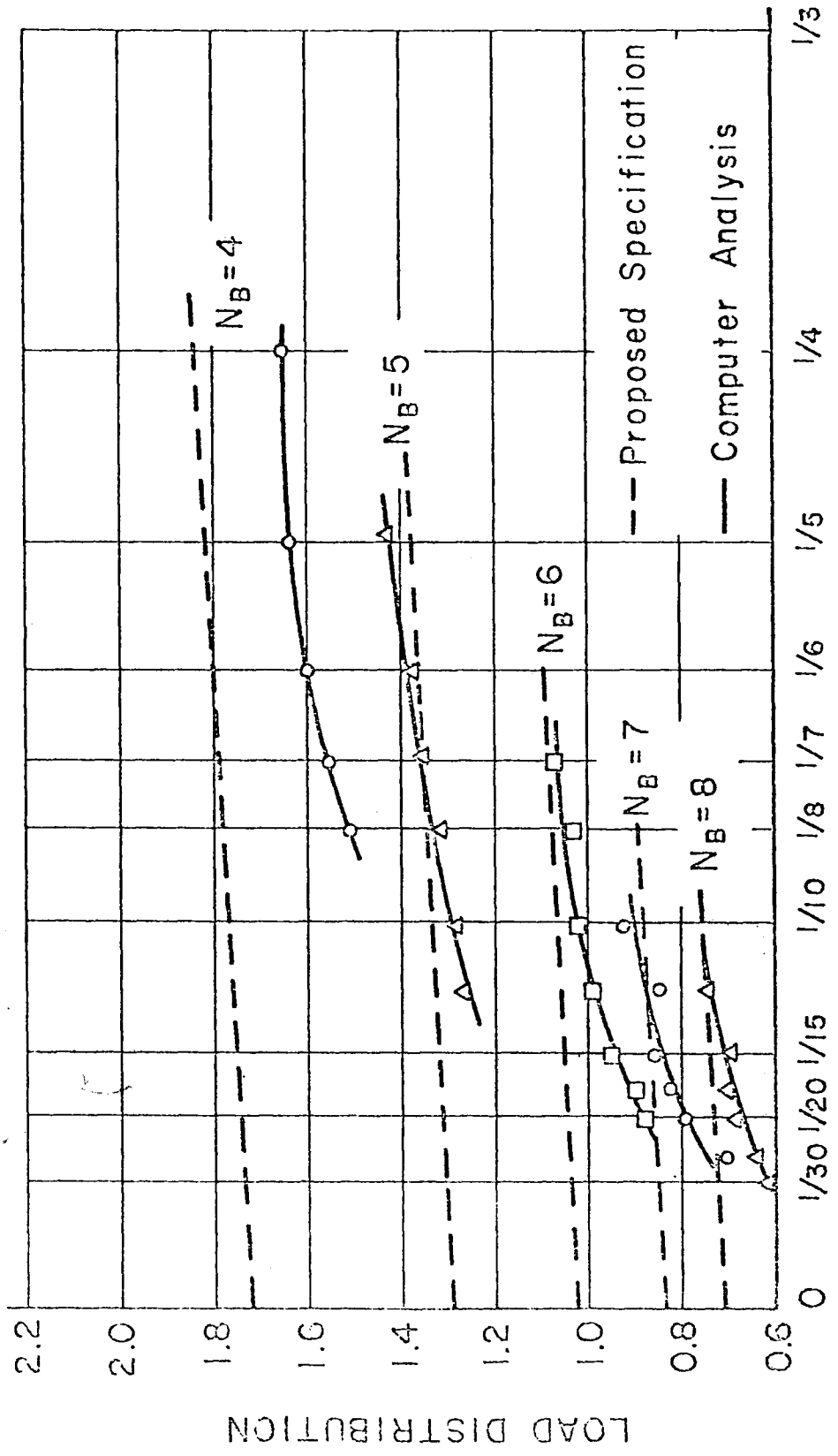

Fig. 31 Distribution Factors for Interior Beam 30 Ft. Wide Bridges ($N_L = 2$)

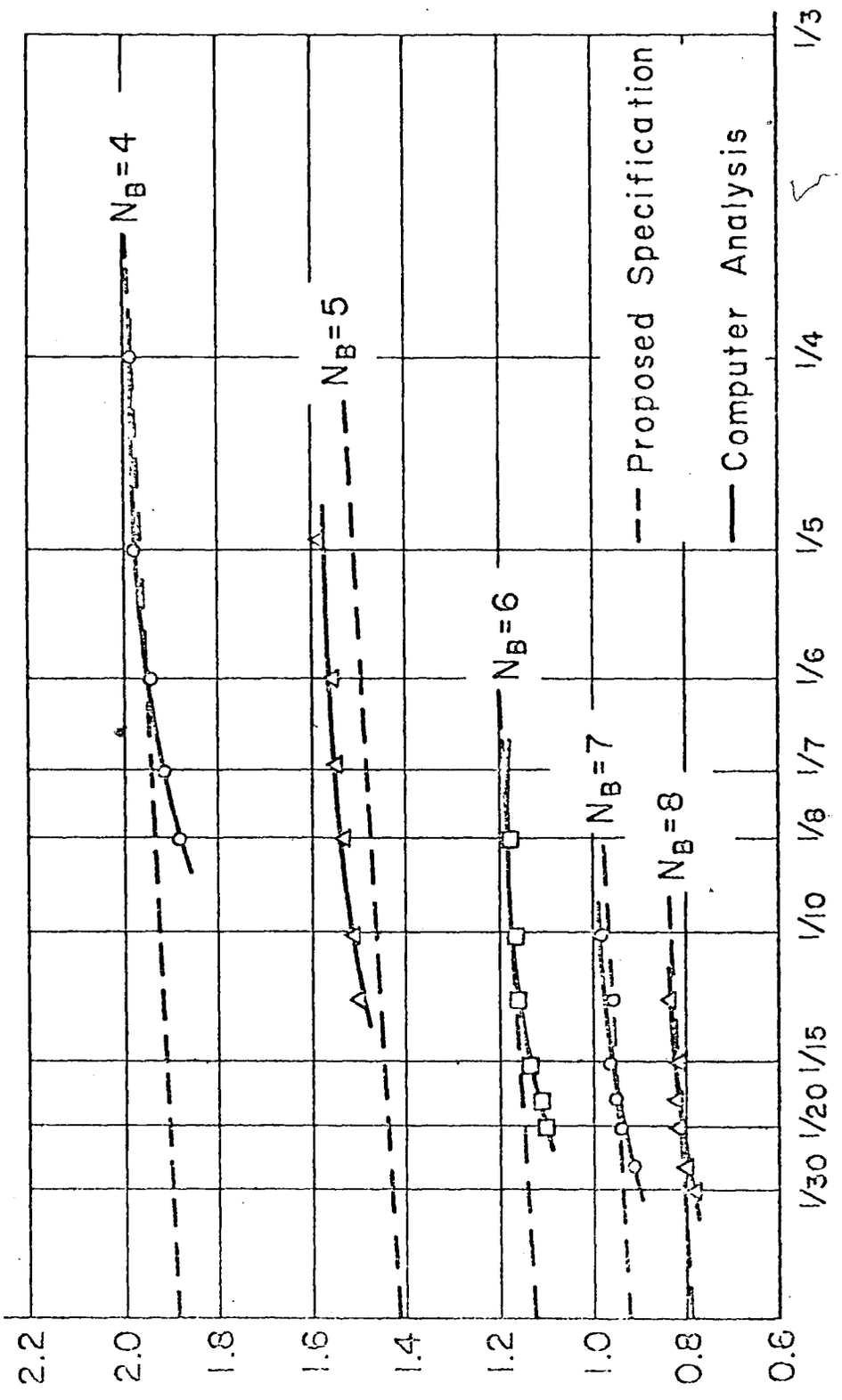

Fig. 32 Distribution Factors for Interior Beam 30 Ft. Wide Bridges (N_L = 3)

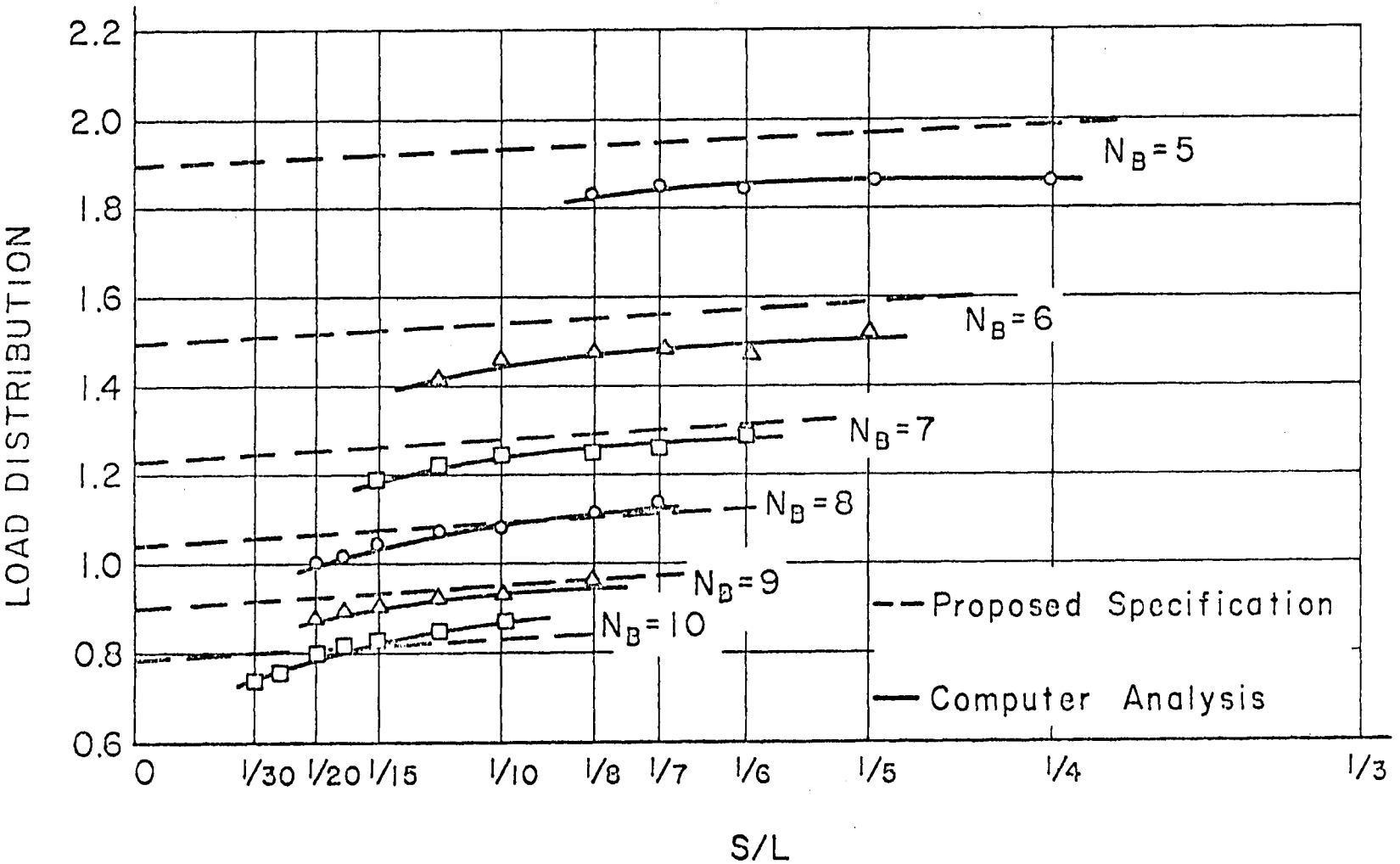

Fig. 33 Distribution Factors for Interior Beam 42 Ft. Wide Bridges (N_L = 3)

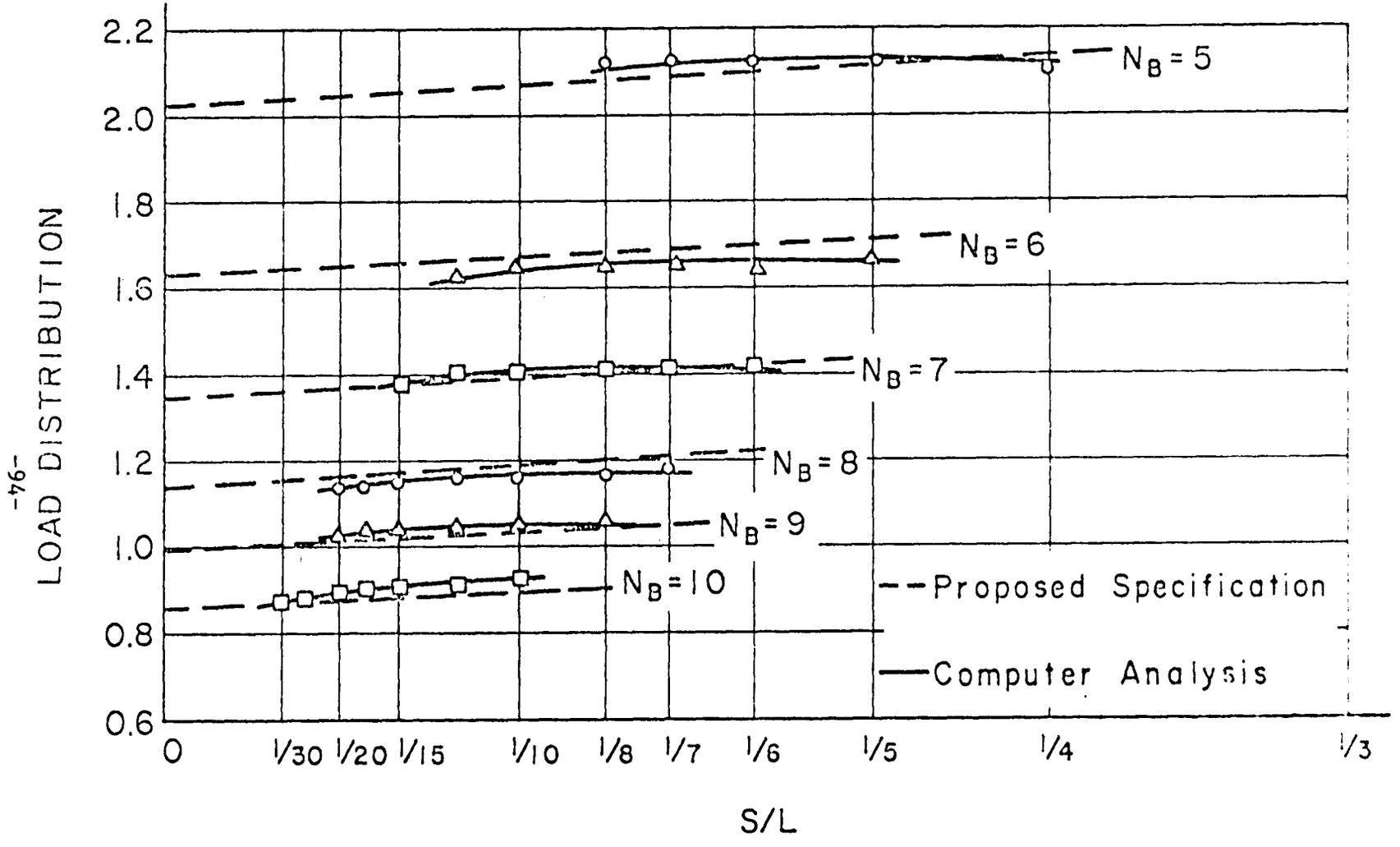

Fig. 34 Distribution Factors for Interior Beam 42 Ft. Wide Bridges (N_L =4)

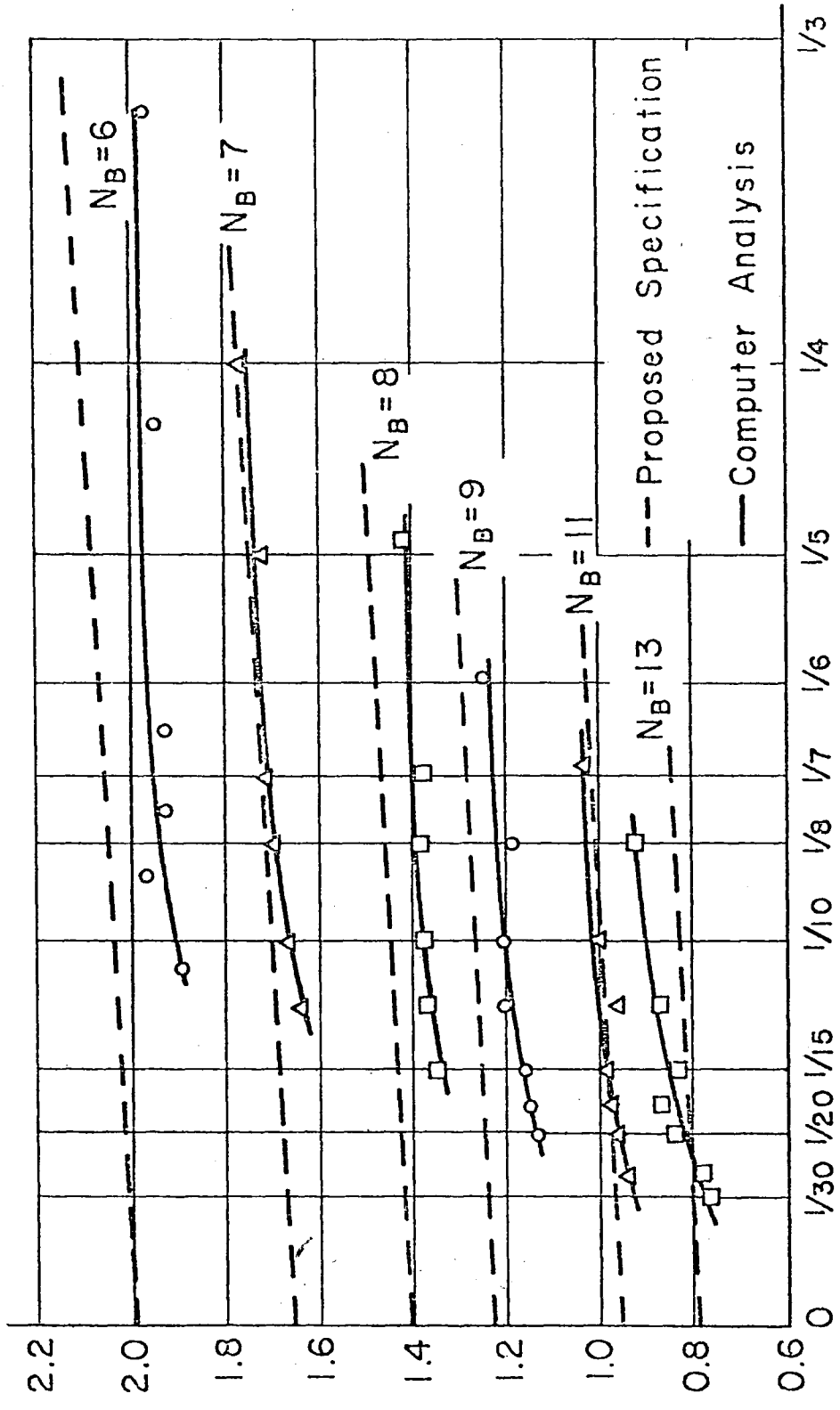

Fig. 35 Distribution Factors for Interior Beam 54 Ft. Wide Bridges (N_L =4)

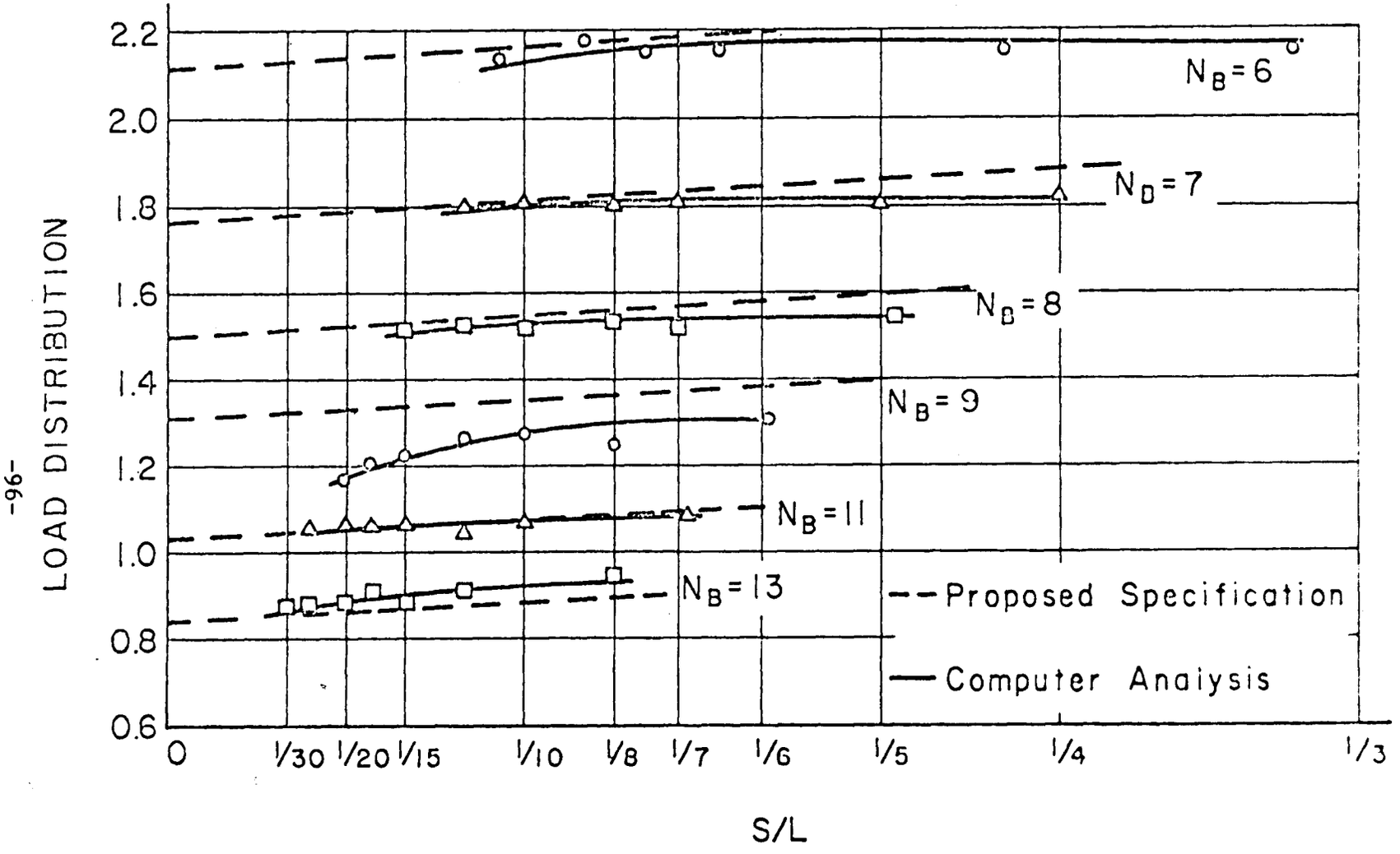

Fig. 36 Distribution Factors for Interior Beam 54 Ft. Wide Bridges (N_L = 5)

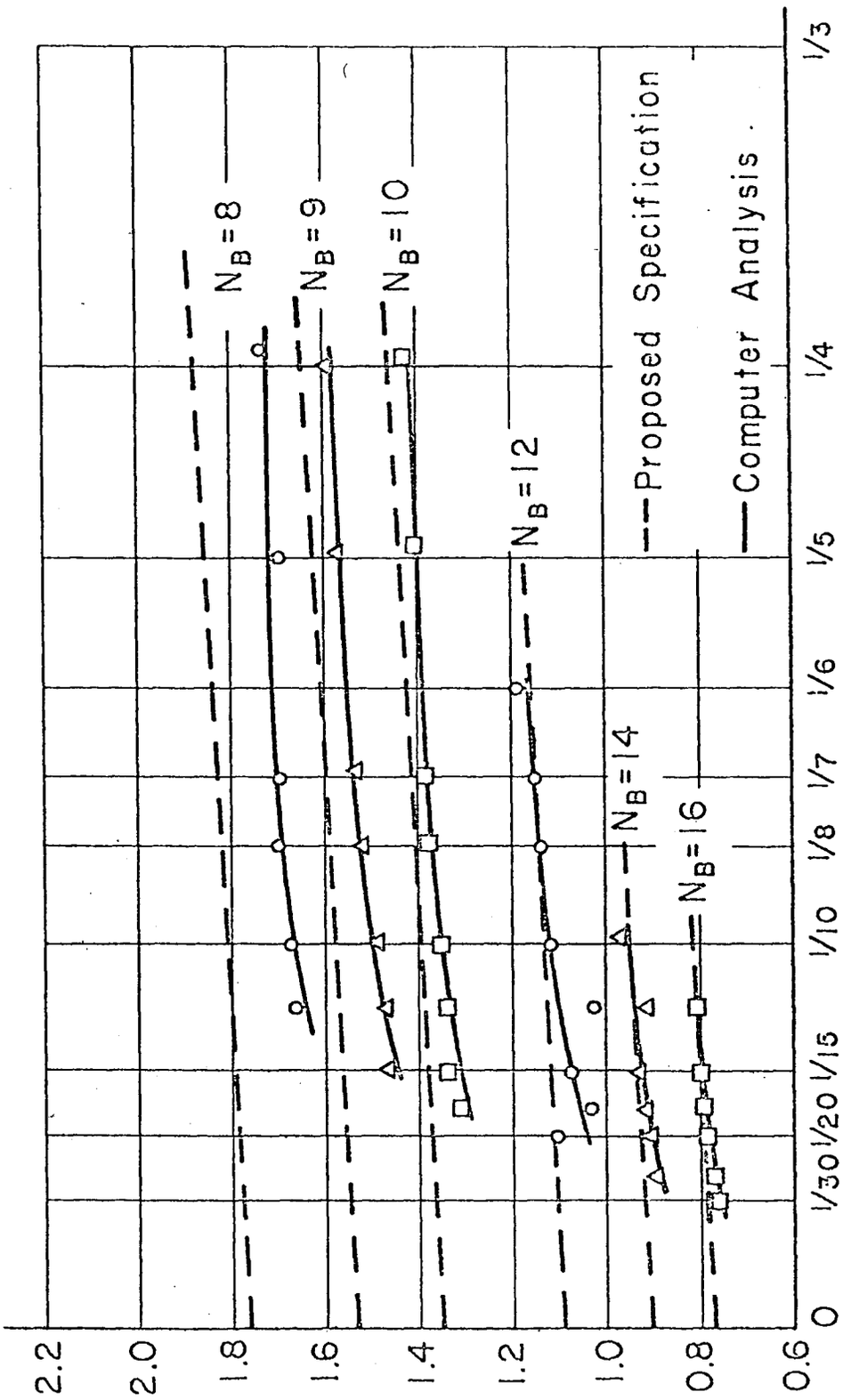

Fig. 37 Distribution Factors for Interior Beam 66 Ft. Wide Bridges (N_L =5)

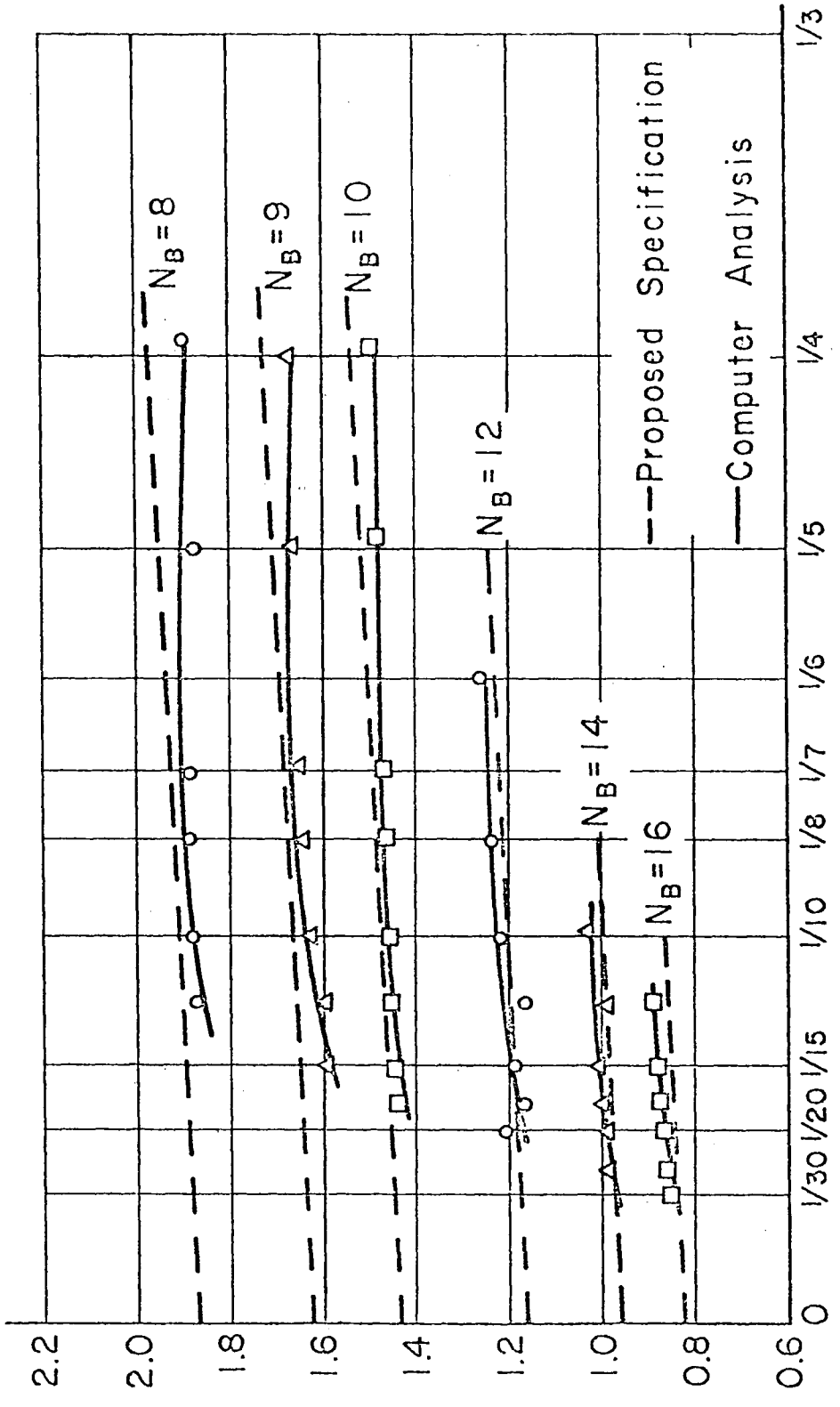

Fig. 38 Distribution Factors for Interior Beam 66 Ft. Wide Bridges (N_L -6)

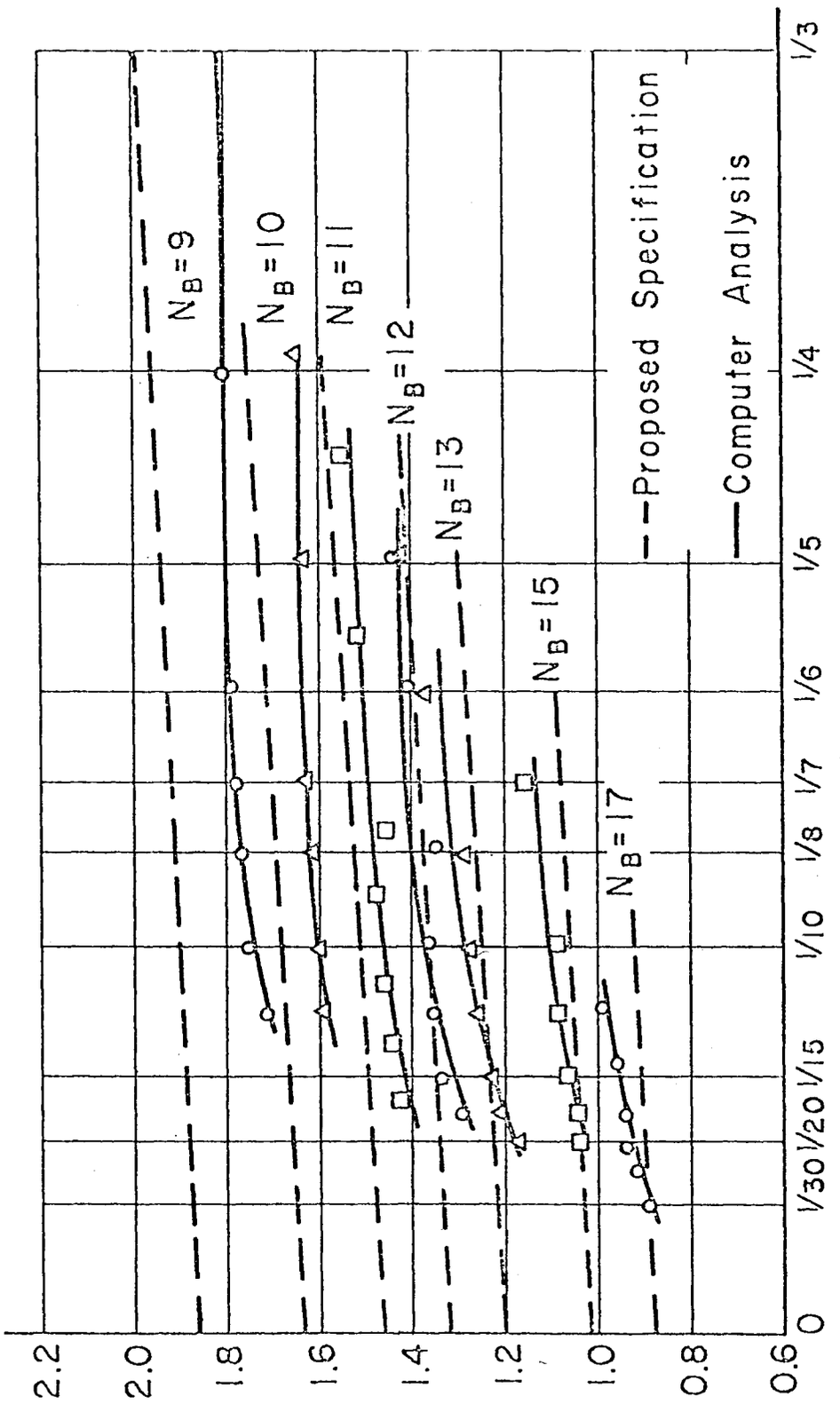

Fig. 39 Distribution Factors for Interior Beam 78 Ft. Wide Bridges (N_L =6)

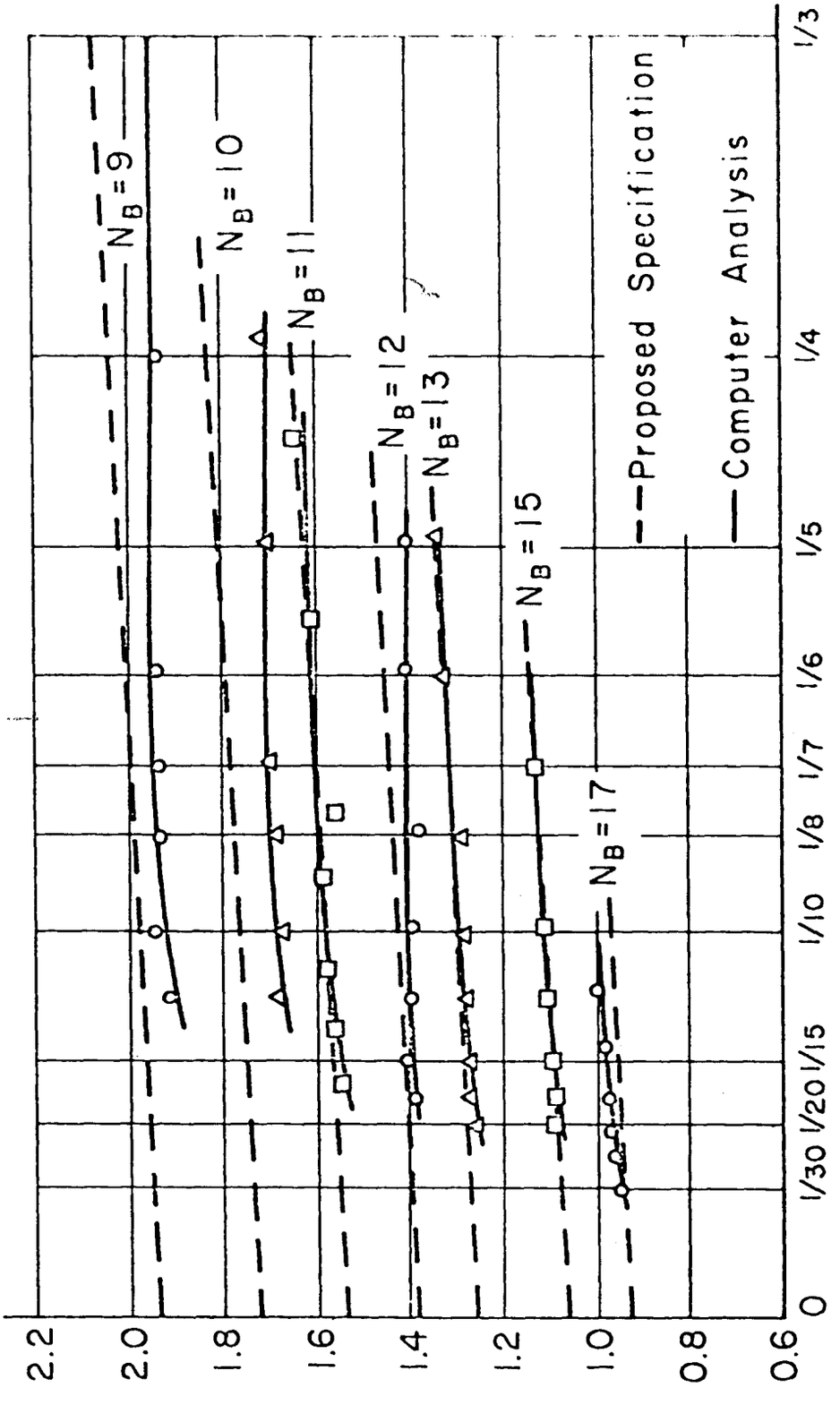

Fig. 40 Distribution Factors for Interior Beam 78 Ft. Wide Bridges (N_L = 7)

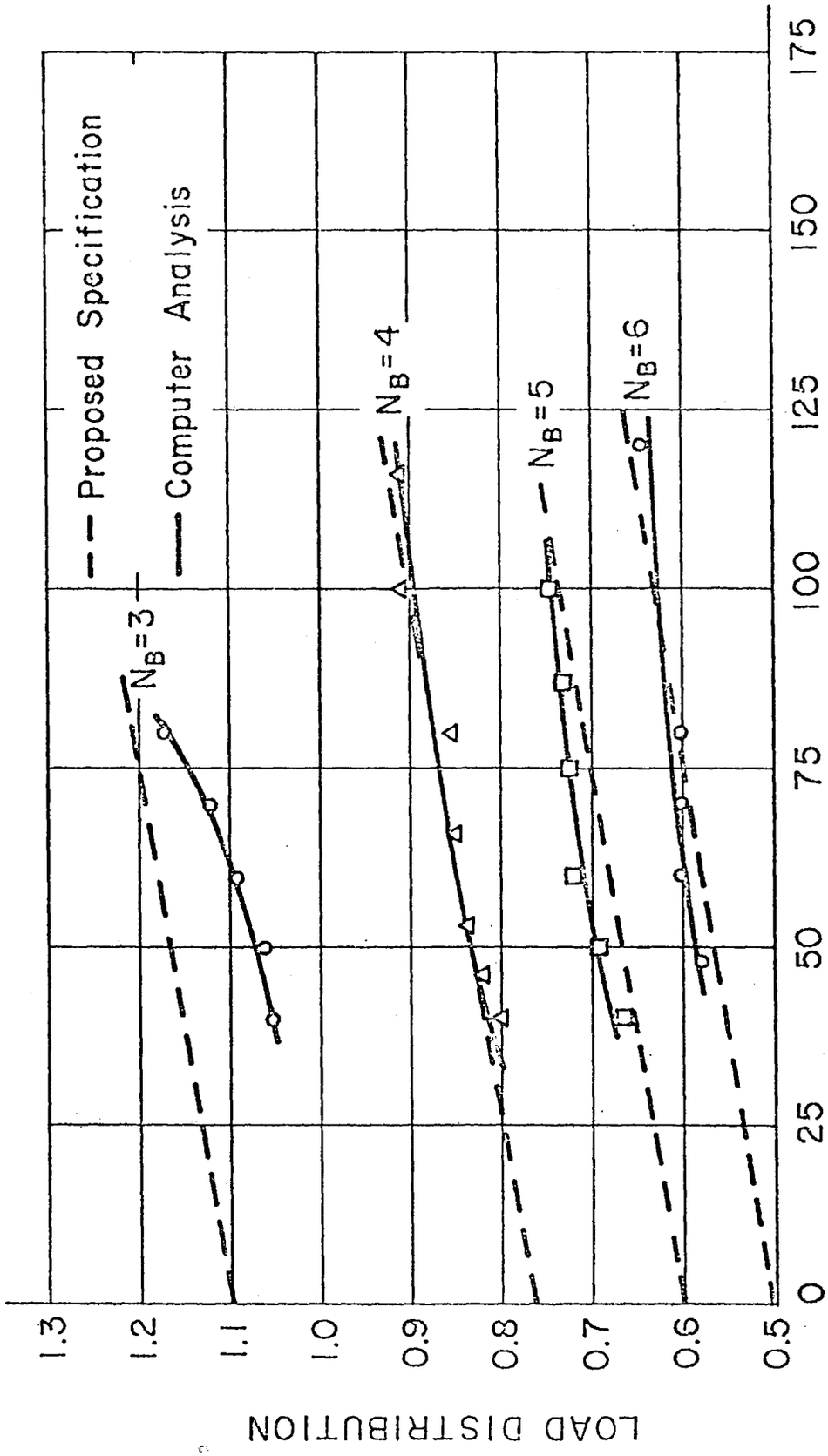

Fig. 41 Distribution Factors for Exterior Beam 20 Ft. Wide Bridges (N_L =2)

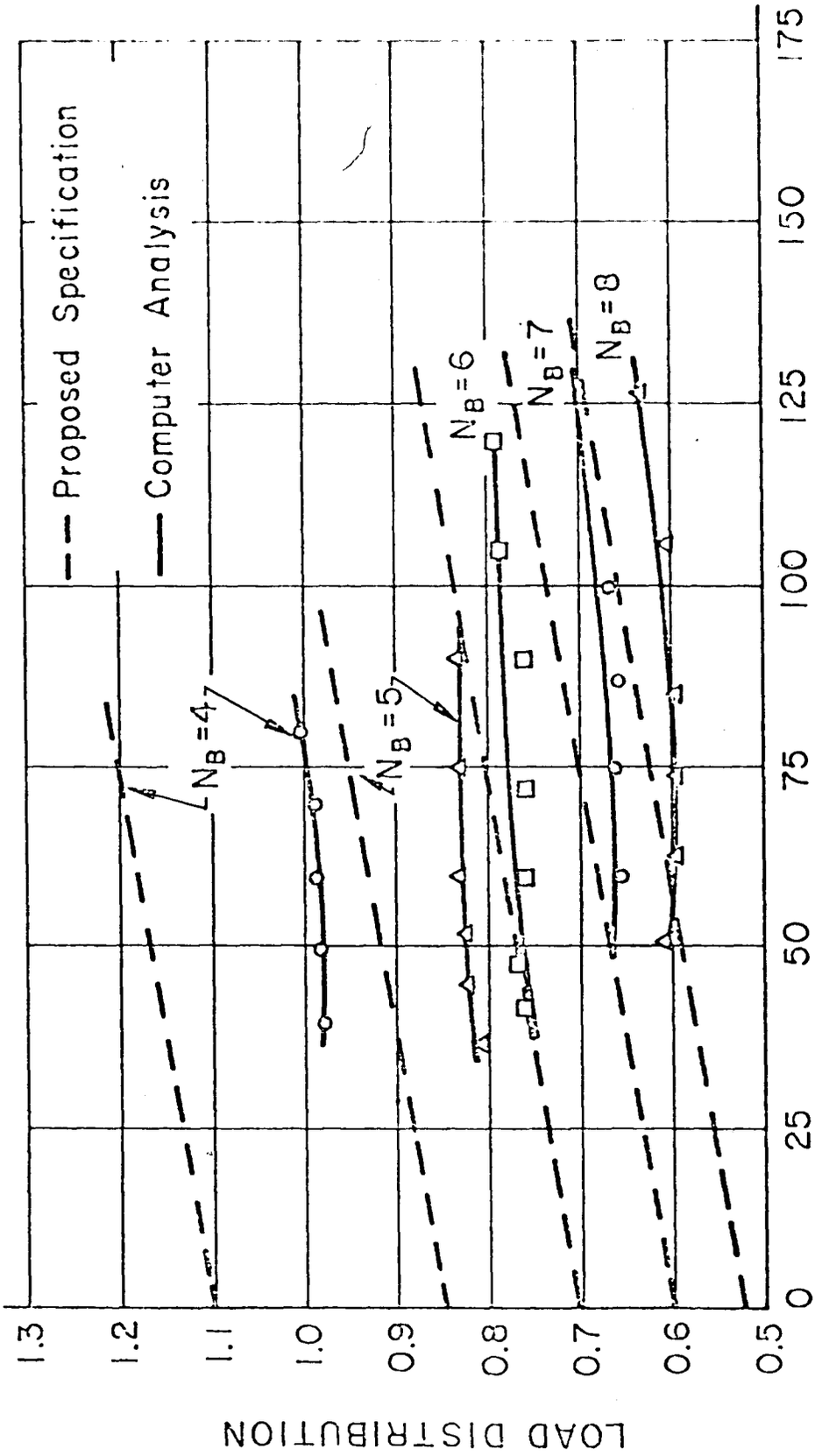

Fig. 42 Distribution Factors for Exterior Beam 30 Ft. Wide Bridges (N_L =2)

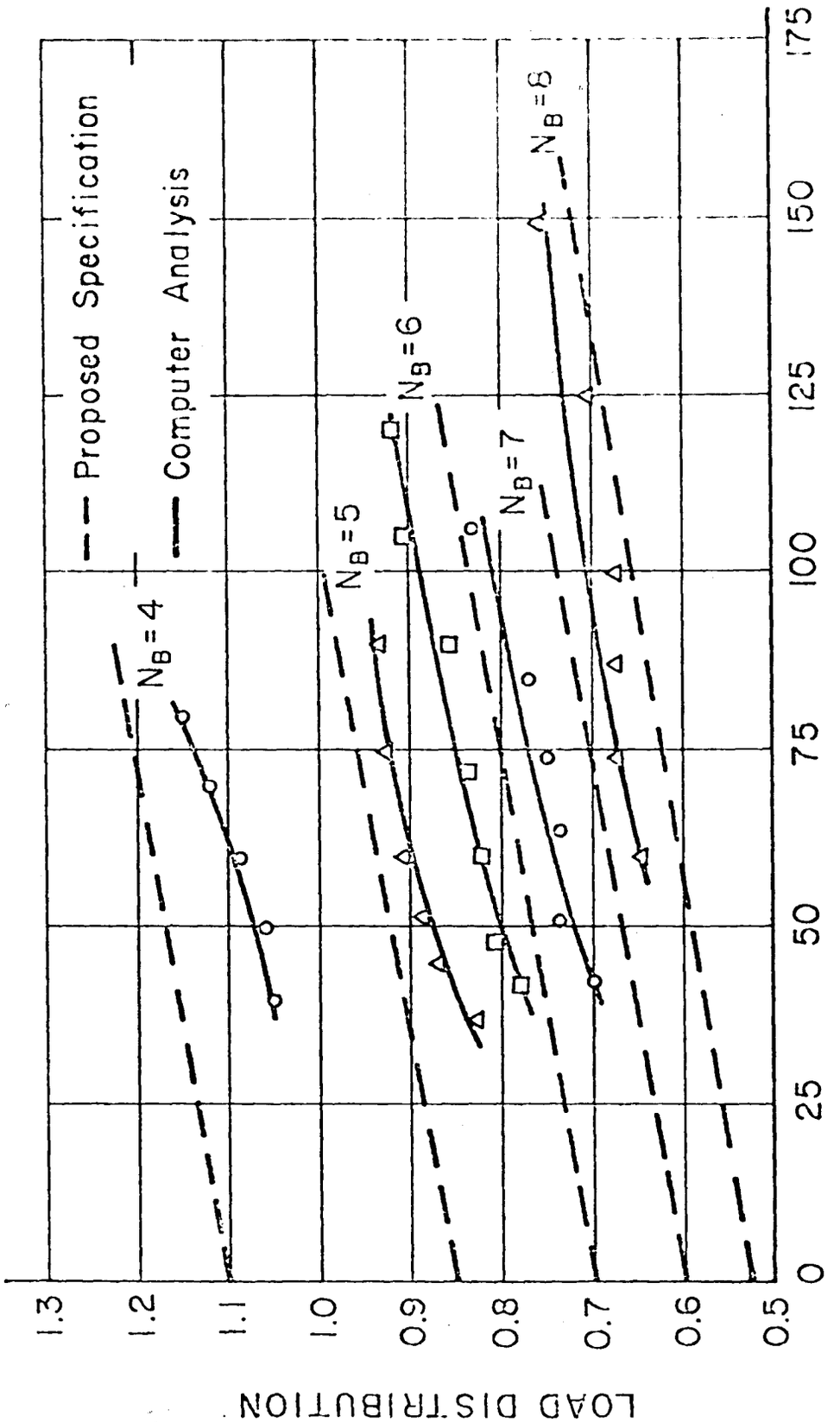

Fig. 43 Distribution Factors for Exterior Beam 30 Ft. Wide Bridge (N_L =3)

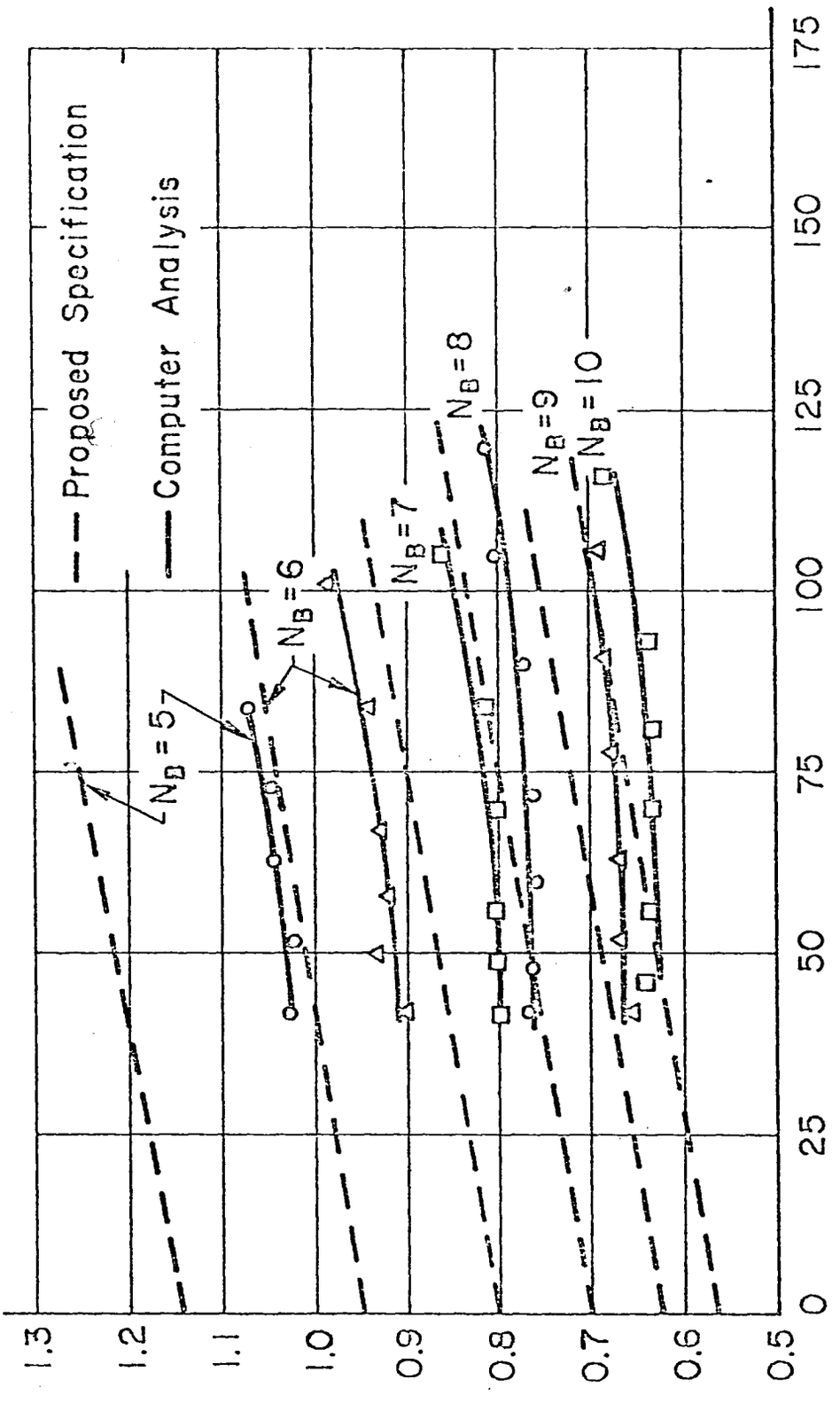

Fig. 44 Distribution Factors for Exterior Beam 42 Ft. Wide Bridges (N_L =3)

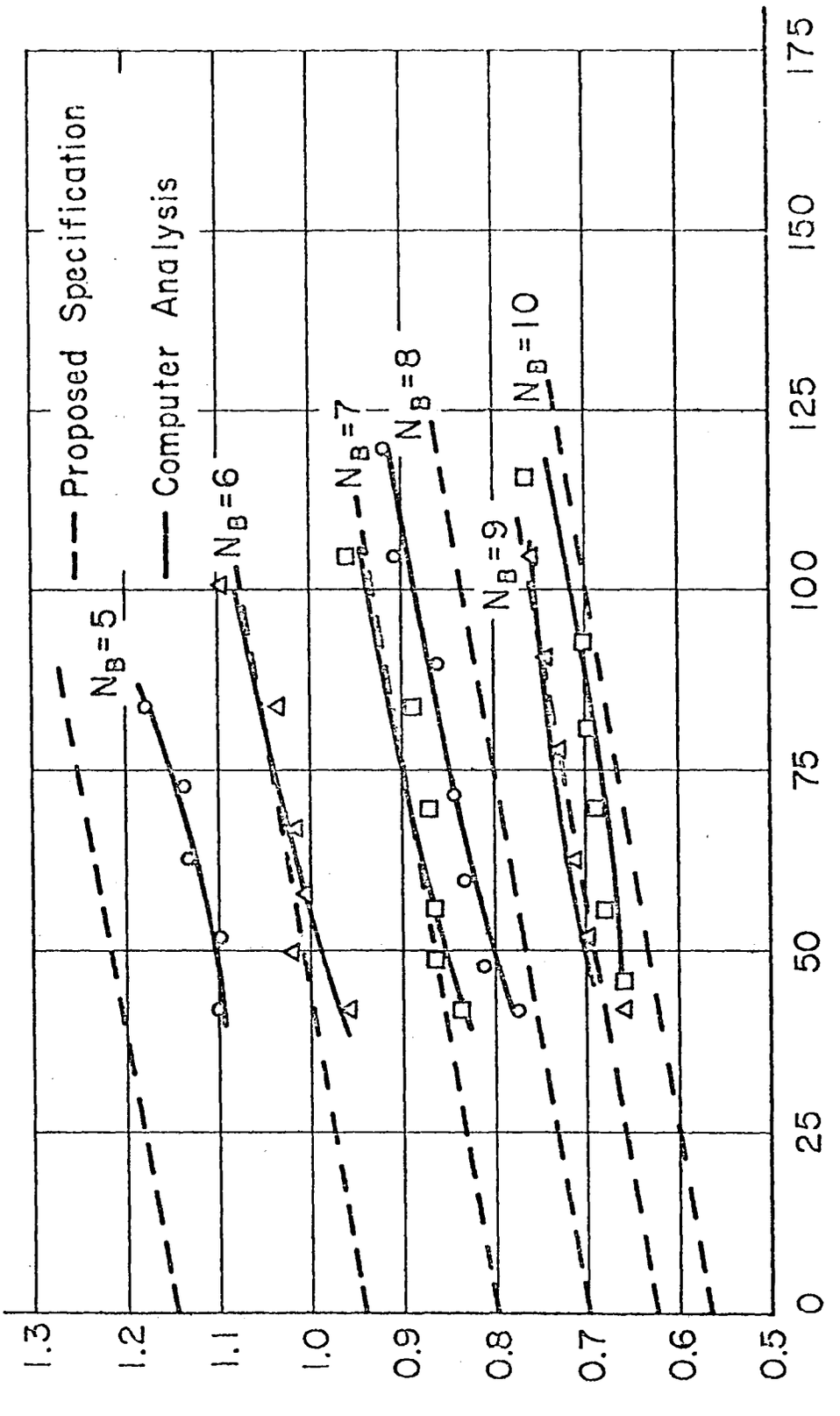

Fig. 45 Distribution Factors for Exterior Beam 42 Ft. Wide Bridges (N_L =4)

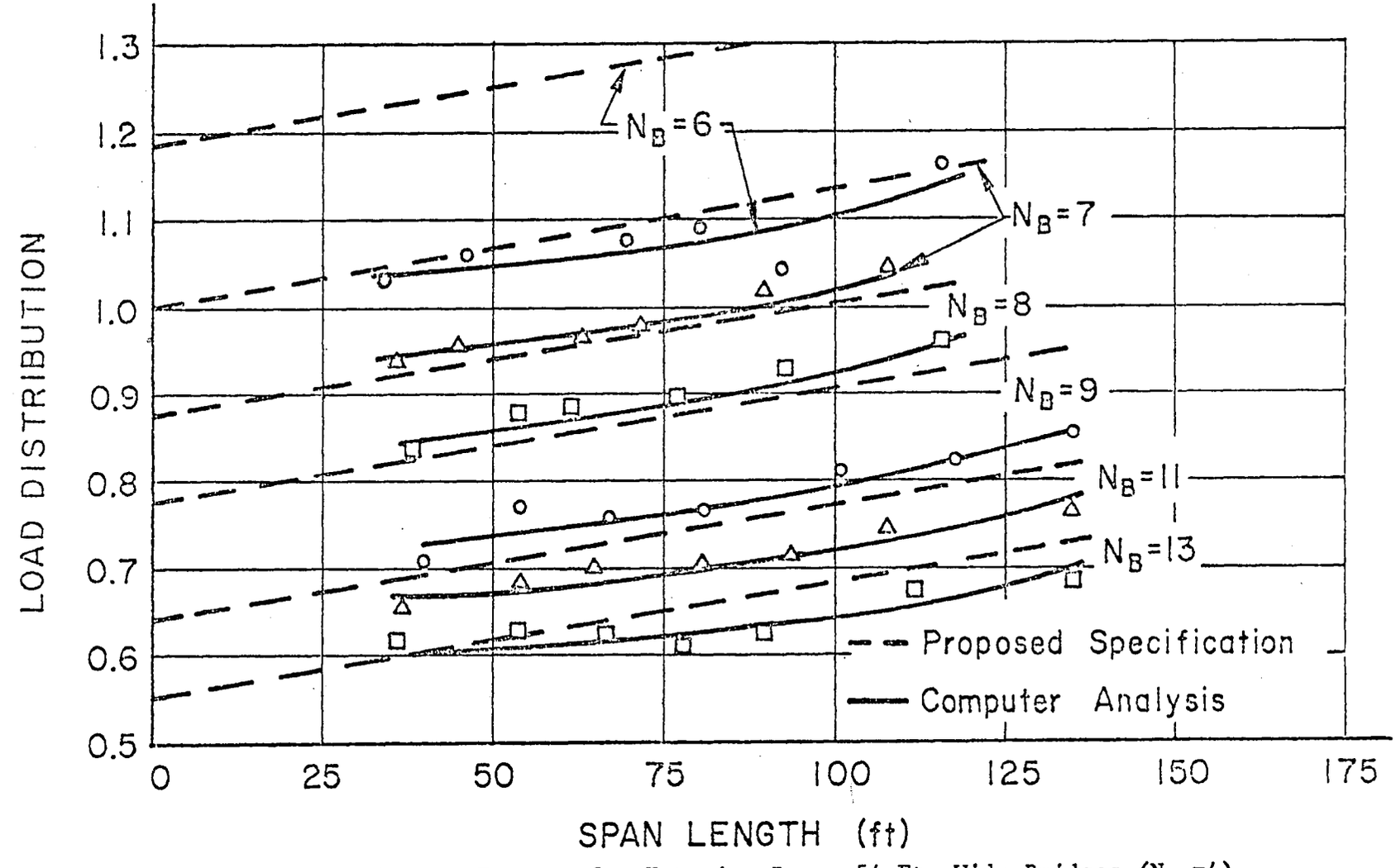

Fig.46 Distribution Factors for Exterior Beam 54 Ft. Wide Bridges (N_L =4)

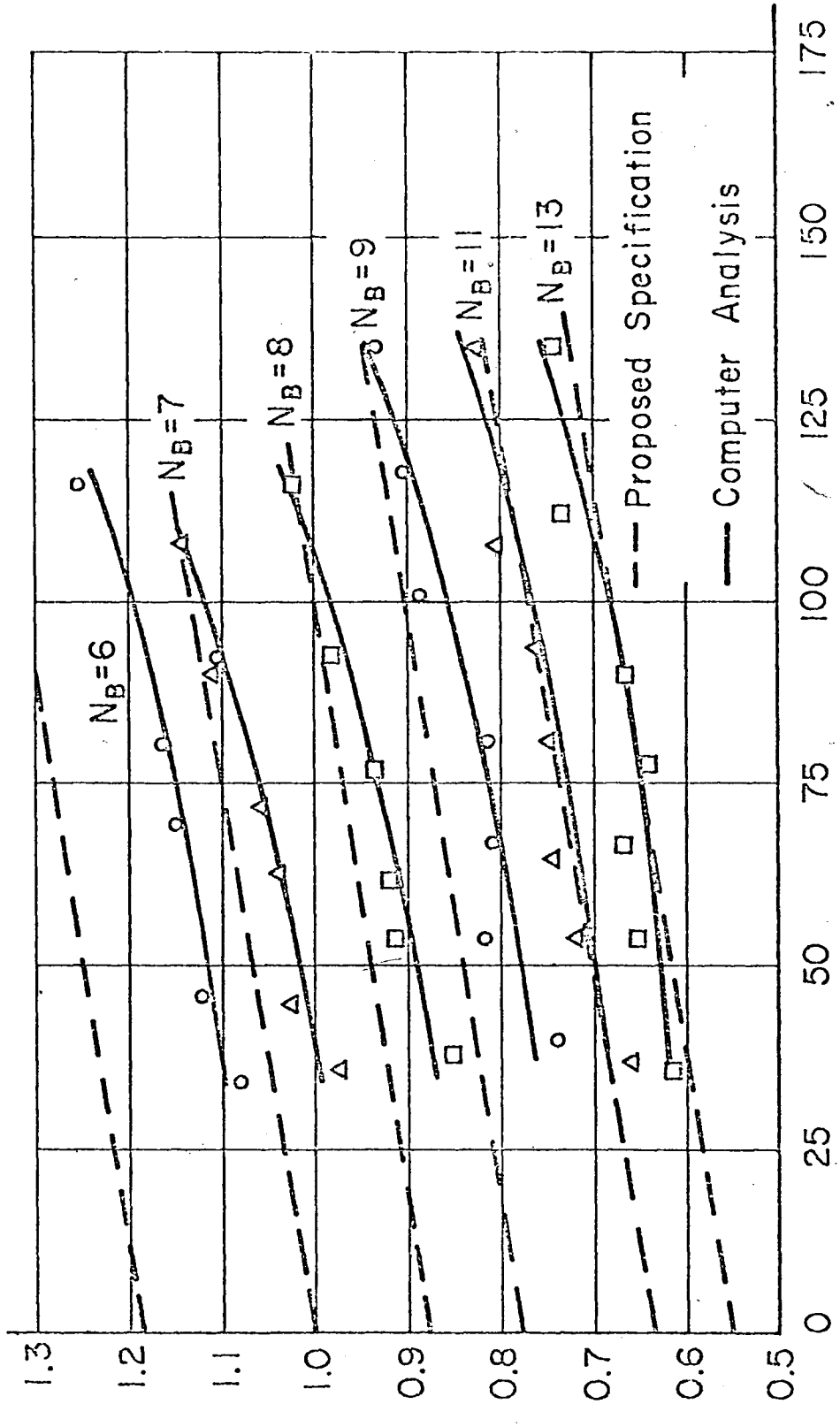

Fig. 47 Distribution Factors for Exterior Beam 54 Ft. Wide Bridges (N_L =5)

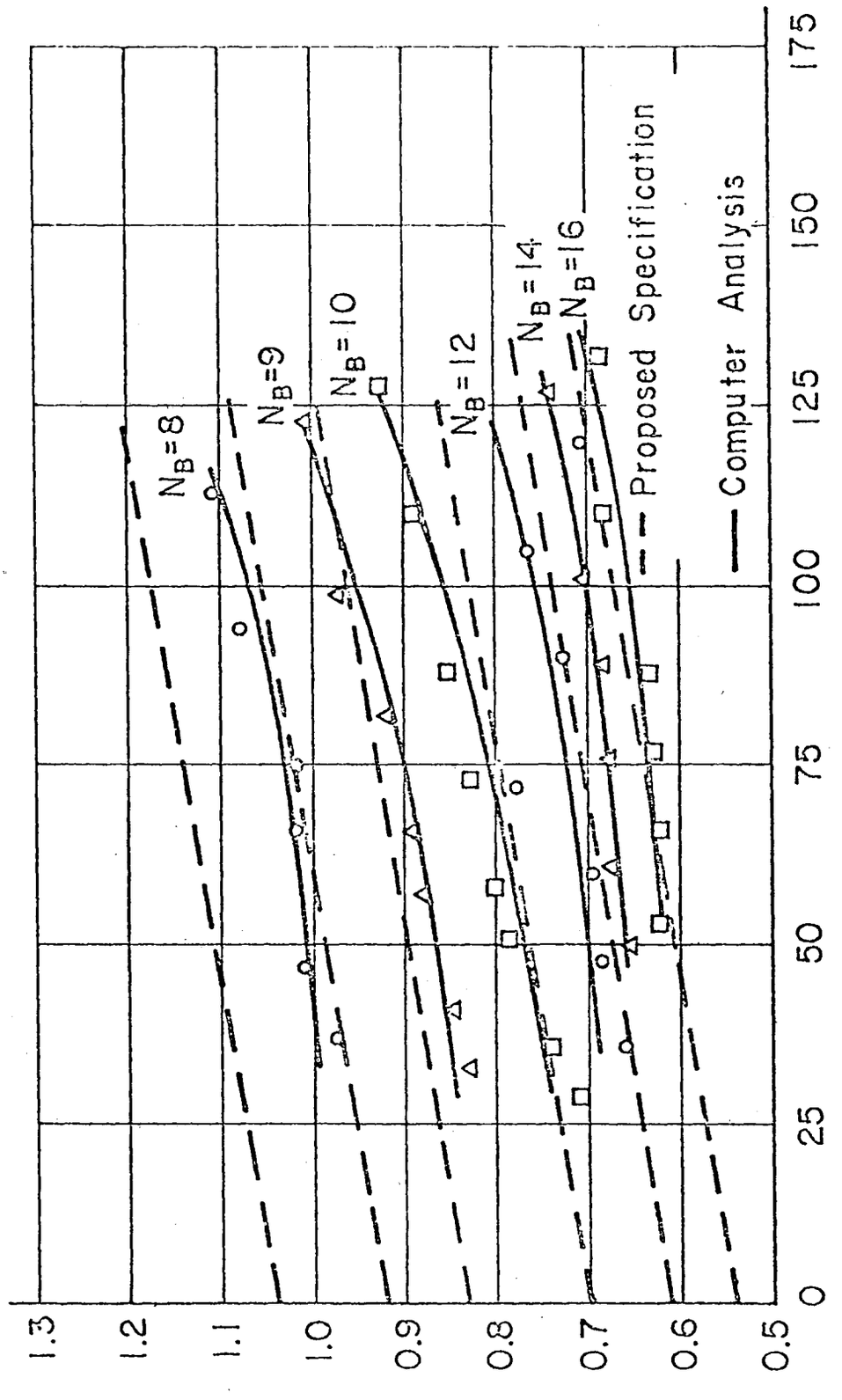

Fig. 48 Distribution Factors for Exterior Beam 66 Ft. Wide Bridges (N_L =5)

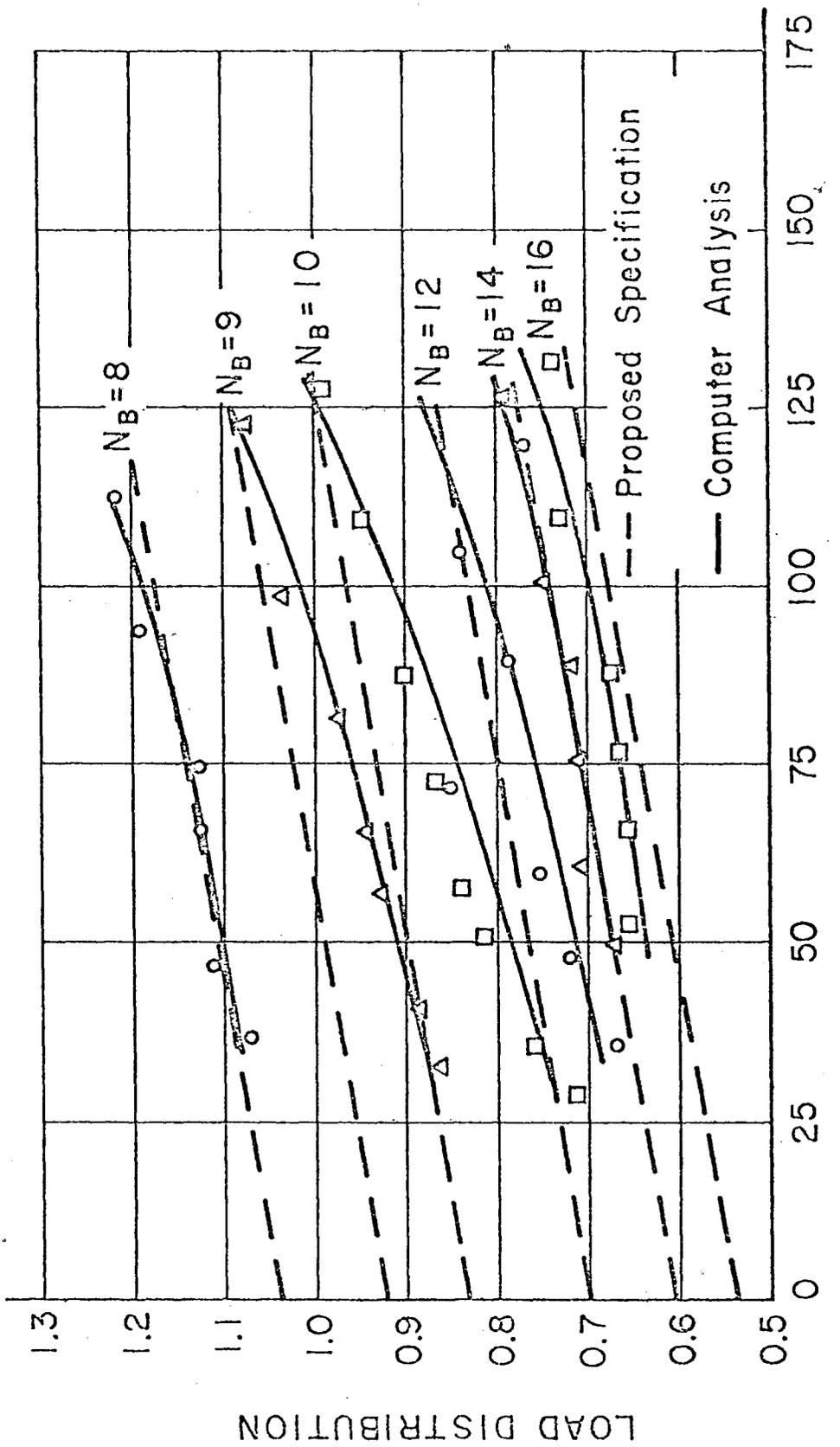

Fig. 49 Distribution Factors for Exterior Beam 66 Ft. Wide Bridges (N_L =6)

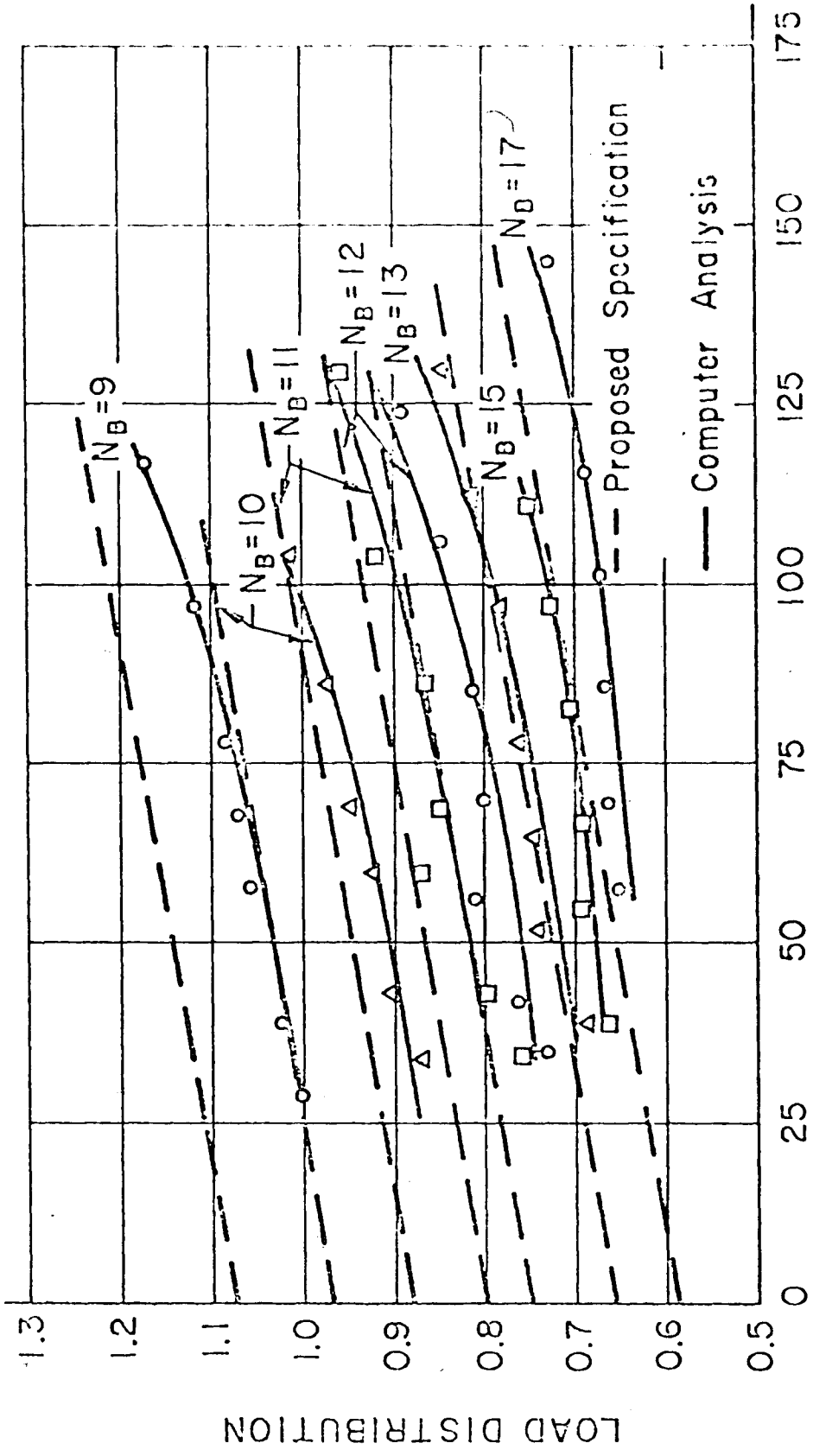

Fig. 50 Distribution Factors for Exterior Beam 78 Ft. Wide Bridges (N_L =6)

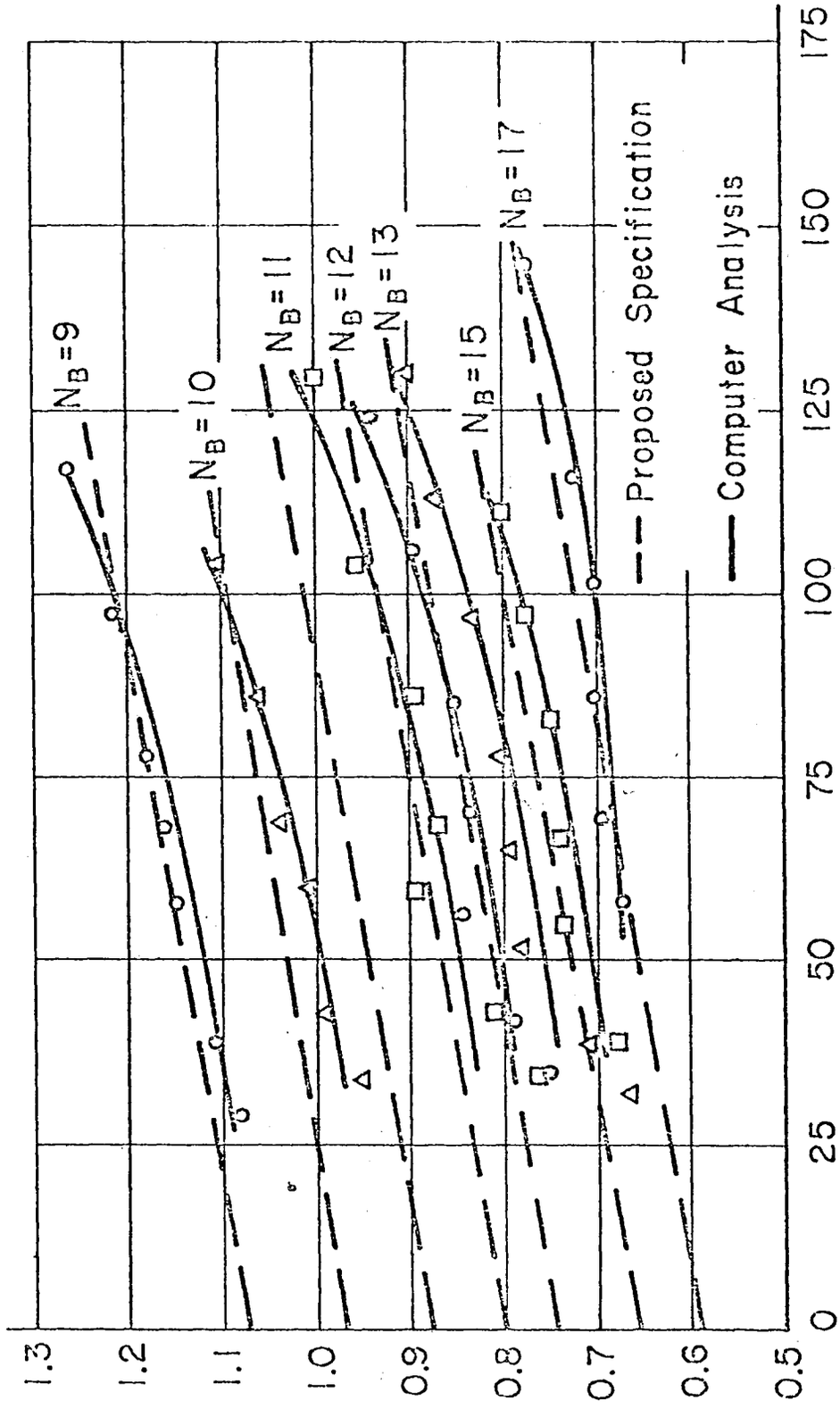

Fig. 51 Distribution Factors for Exterior Beam 78 Ft. Wide Bridges (N_L =7)

10. REFERENCES

1. American Association of State Highway and Transportation Officials
   STANDARD SPECIFICATIONS FOR HIGHWAY BRIDGES, Washington, D. C., 1973.

2. Adini, A. and Clough, R. W.
   ANALYSIS OF PLATE BENDING BY THE FINITE ELEMENT METHOD, Report submitted to the National Science Foundation, Grant No. G7337, University of California, Berkeley, California, 1960.

3. Chen, C. H. and VanHorn, D. A.
   STATIC AND DYNAMIC FLEXURAL BEHAVIOR OF A PRESTRESSED CONCRETE I-BEAM BRIDGE - BARTONSVILLE BRIDGE, Fritz Engineering Laboratory Report No. 349.2, January 1971.

4. Chen, C. H. and VanHorn, D. A.
   SLAB BEHAVIOR OF A PRESTRESSED CONCRETE I-BEAM BRIDGE - LEHIGHTON BRIDGE, Fritz Engineering Laboratory Report No. 349.5, July 1971.

5. DeCastro, E. S. and Kostem, C. N.
   USER'S MANUAL FOR PROGRAM PLATE, Fritz Engineering Laboratory Report No. 400.13, January 1975.

6. Eby, C. C., Kulicki, J. M., Kostem, C. N. and Zellin, M. A.
   THE EVALUATION OF ST. VENANT TORSIONAL CONSTANTS FOR PRESTRESSED CONCRETE I-BEAMS, Fritz Engineering Laboratory, Report No. 400.12, Lehigh University, June 1973.

7. Pennsylvania Department of Transportation, Bridge Division
   STANDARD FOR BRIDGE DESIGN (PRESTRESSED CONCRETE STRUCTURES), BD-201, 1973.

8. Timoshenko, S. P. and Woinowsky, K.
   THEORY OF PLATES AND SHELLS, McGraw-Hill Book Company, Inc., 1959.

9. VanHorn, D. A. and Chen, C. H.
STRUCTURAL BEHAVIOR OF A PRESTRESSED CONCRETE I-BEAM BRIDGE - LEHIGHTON BRIDGE, Fritz Engineering Laboratory, Report No. 349.4, October 1971.

10. Wegmuller, A. W. and VanHorn, D. A.
SLAB BEHAVIOR OF A PRESTRESSED CONCRETE I-BEAM BRIDGE-BARTONSVILLE BRIDGE, Fritz Engineering Laboratory, Report No. 349.3, May 1971

11. Wegmuller, A. W. and Kostem, C. N.
FINITE ELEMENT ANALYSIS OF PLATES AND ECCENTRICALLY STIFFENED PLATES, Fritz Engineering Laboratory Report No. 378A.3, February 1973.

12. Wegmuller, A. W. and Kostem, C. N.
EFFECT OF IMPERFECTIONS ON THE STATIC RESPONSE OF BEAM-SLAB TYPE HIGHWAY BRIDGES, Proceedings of the Specialty Conference on the Finite Element Method in Civil Engineering, Canadian Society of Civil Engineering, McGill University, Montreal, Quebec, Canada, pp. 947-970, June 1972.

13. Zellin, M. A., Kostem, C. N., and VanHorn, D. A.
STRUCTURAL BEHAVIOR OF BEAM-SLAB HIGHWAY BRIDGES A SUMMARY OF COMPLETED RESEARCH AND BIBLIOGRAPHY, Fritz Engineering Laboratory Report 387.1, May 1973.

14. Zienkiewicz, O.
FINITE ELEMENT METHOD IN ENGINEERING SCIENCE, McGraw-Hill Book Company, 1971

11. ACKNOWLEDGMENTS

The work was sponsored by the Pennsylvania Department of Transportation, Federal Highway Administration and the Reinforced Concrete Research Council. Their support is appreciated.

I wish to express a note of deep appreciation and gratitude to Dr. Celal N. Kostem, Dr. David A. VanHorn and Dr. John M. Kulicki for their help and encouragement. Thanks are extended to Messrs. Ernesto S. deCastro and William S. Peterson for their assistance and continuing interest; and to Mr. Stephen Tumminelli who reviewed the manuscript.

Appreciation is also due to the Lehigh University Computing Center staff for their cooperation, especially Robert A. Pfenning, John H. Morrison and Frank E. Washburn.

The manuscript was typed in the Fritz Engineering Laboratory Word Processing Center and the figures were prepared by the Drafting staff.

12. VITA

The author was born July 15, 1951 in Brooklyn, New York.

After graduating from Bishop Loughlin Memorial High School in 1968, the author attended Manhattan College. He received the degree of Bachelor of Science in Civil Engineering in June 1972.

In 1972, he came to Lehigh University and was appointed as a research assistant in the Structural Concrete Division of Fritz Engineering Laboratory. Since that time, he has been associated with the project, "The Development and Refinement of Load Distribution Provisions for Prestressed Concrete Beam-Slab Bridges.